REPUBLIC OF TURKEY
YILDIZ TECHNICAL UNIVERSITY
GRADUATE SCHOOL OF NATURAL AND APPLIED SCIENCES

MEAN FIELD DESCRIPTION OF FINITE NUCLEI UNDER EXTREME CONDITIONS OF ISOSPIN AND TEMPERATURE

ESRA YÜKSEL

Ph.D. THESIS
DEPARTMENT OF PHYSICS
PROGRAM OF PHYSICS

ADVISER
ASSOC.PROF.DR. KUTSAL BOZKURT

İSTANBUL, 2015

REPUBLIC OF TURKEY

YILDIZ TECHNICAL UNIVERSITY

GRADUATE SCHOOL OF NATURAL AND APPLIED SCIENCES

MEAN FIELD DESCRIPTION OF FINITE NUCLEI UNDER EXTREME CONDITIONS OF ISOSPIN AND TEMPERATURE

A thesis submitted by Esra YÜKSEL in partial fulfillment of the requirements for the degree of **DOCTOR OF PHILOSOPHY** is approved by the committee on 22.12.2015 in Department of Physics, Physics Program.

Thesis Adviser
Assoc. Prof. Dr. Kutsal BOZKURT
Yıldız Technical University

Thesis Co-Adviser
Prof. Dr. Elias KHAN
Universite Paris-Sud-11, Institut de Physique Nucléaire

Approved by the Examining Committee
Assoc. Prof. Dr. Kutsal BOZKURT
Yıldız Technical University ____________________

Prof. Dr. Elias KHAN
Universite Paris-Sud-11, Institut de Physique Nucléaire ____________________

Prof. Dr. Gianluca COLÒ
University of Milano-INFN ____________________

Prof. Dr. Hasan TATLIPINAR
Yıldız Technical University ____________________

Prof. Dr. İskender Atilla REYHANCAN
İstanbul Technical University ____________________

Assoc. Prof. Dr. Cem ÖZEN
Kadir Has University ____________________

Assoc. Prof. Dr. Taylan YETKİN
Yıldız Technical University ____________________

This study was supported by The Scientific and Technological Research Council of Turkey (TÜBİTAK) under project number MFAG-114F335 and also by BAP-2014-01-01-DOP02 project.

ACKNOWLEDGMENTS

There are a lot of people to thank who touched my life during my Ph.D. First of all, I would like to thank my adviser, Assoc. Prof. Dr. Kutsal Bozkurt for introducing me to the IPN theory group, his endless support and encouragements during my thesis. I would like to thank to my co-adviser Prof. Dr. Elias Khan, for his guidance, patience and trust in me. Working with him is a great opportunity for me. I am really grateful for his supervision of my work.

During my thesis, I have also worked with great people who expanded my vision with their advanced knowledge and discussions on the nuclear theory. I wish to give my deepest gratitude for Prof. Dr. Nguyen Van Giai for his encouragements, guidance and stimulating discussions. I am also grateful to him for his careful reading of my thesis. Also, I would like to thank IPN theory group for their kindness and hospitality during my visits to Orsay. I would like to thank Prof. Dr. Gianluca Colò for his hospitality in Milano, guidance and useful discussions on the QRPA part of my thesis. Working with him is big change for me. I really appreciate for his collaborations and helpful discussions. I'd like to give special thanks to the Dr. Yifei Niu for her help and enlightening discussions on the finite temperature calculations.

Also, I would like to thank my great friends in Yıldız Technical University, Physics Department; Dr. Pınar Gökdemir, Dr. Deneb Menda, Eylem Attar, Dr. Zeynep Güven Özdemir and Dr. Nimet Yılmaz Canlı, Dr. Asuman Aşıkoğlu Bozkurt, Dr. Ayşegül Çelik Bozdoğan, Dr. Altan Bozdoğan and to all my friends for their valuable support and friendships. A special thank goes to Neslihan Ayarcı for her friendship and endless support at every point of my life. My deepest gratitude and thanks are for my family: Burhan Yüksel, Kadriye Yüksel and Erkan Yüksel. Their confidence and support gave me strength to continue on this road. Finally, I would like to thank and express my gratitude to the Scientific and Technological Research Council of Turkey (TÜBİTAK) for supporting me during my thesis under BIDEB-2211 Graduate Scholarship Programme for Ph.D. students and also with project number MFAG-114F335.

December, 2015

Esra YÜKSEL

TABLE OF CONTENTS

Page

LIST OF SYMBOLS

A	Atom number
N	Neutron number
Z	Proton number
H	Hamiltonian
φ_i	single particle wave function
σ	Spin operator
$\hat{k}$	Momentum operator
$S(E)$	Strength function
α_T	Skyrme tensor parameter
β_T	Skyrme tensor parameter
U_H	Direct term
U_F	Fock term
V_T	Tensor potential
U_q	Central potential
W_q	Spin-orbit potential
$\mathscr{E}$	Energy functional
ρ	Density
κ	abnormal (pairing) density
$\delta\rho$	Transition density
$\hat{P}_\sigma$	Spin exchange operator
J	Spin-orbit density
τ	Kinetic energy density

LIST OF ABBREVIATIONS

EWSR	Energy Weight Sum Rule
FT	Finite temperature
GDR	Giant Dipole Resonance
GMR	Giant Monopole Resonance
GQR	Giant Quadrupole Resonance
HF	Hartree Fock
HFBCS	Hartree Fock Bardeen Cooper Schrieffer
HFB	Hartree Fock Bogoliubov
IS	Isoscalar
IV	Isovector
MFT	Mean Field Theory
NEWSR	Energy Weight Sum Rule
PDR	Pygmy Dipole Resonance
RPA	Random Phase Approximation
QRPA	Quasiparticle Random Phase Approximation

LIST OF FIGURES

Page

LIST OF TABLES

Page

ABSTRACT

MEAN FIELD DESCRIPTION OF FINITE NUCLEI UNDER EXTREME CONDITIONS OF ISOSPIN AND TEMPERATURE

Esra YÜKSEL

Department of Physics

Ph.D. Thesis

Adviser: Assoc. Prof. Dr. Kutsal BOZKURT

Co-Adviser: Prof. Dr. Elias KHAN

Nowadays, investigation of nuclei far from the stability line has become a central topic in the nuclear physics community. With the advances in the experimental facilities, scientists are able to study the different parts of the nuclear landscape with larger proton-neutron asymmetry which is quite important to understand the underlying dynamics of atomic nuclei. In the theoretical framework, the self-consistent mean field models are the appropriate tools in order to probe the static and dynamic properties of atomic nuclei.

In recent years, the formation of the low-energy modes below the Giant Resonance region become a popular topic in nuclear physics, both experimentally and theoretically. Especially, the low-energy part of the dipole resonances attracted scientists due its relation with neutron skin thickness, nuclear symmetry and also with the astrophysical processes like r-process nucleosynthesis. However, the nature and behavior of low-energy modes are not clear yet. In the first part of this thesis, the high-energy and low-energy dipole and monopole modes are investigated within the mean field framework using Skyrme HF+RPA at zero temperature. In particular, we focus on the behavior of the low-energy part of the monopole and dipole spectrum by analyzing the transition densities and collectivity of an excited state. The calculations reveal that the behavior of the low-energy modes are rather different from the high-energy part of the spectrum. They show a complex isoscalar and isovector behavior. In addition, low-energy monopole excitations exhibit a pure single-particle excitation. These pure single-particle excitations allow to analyze the splitting of the corresponding spin-orbit partners.

Recently, exciting results are obtained far from the stability line with the change of the nuclear magic numbers. The magicity of ^{54}Ca nuclei with N=34 magic number has been confirmed with the experimental results which took place at RIKEN. The effect of the tensor force on the evolution of the single-particle energies of nuclei are also investigated within the framework of this thesis. We employ both HFB and HF-BCS methods using Skyrme-type energy density functionals. An increase is obtained in the neutron spin-orbit splittings of p and f states due to the effect of the tensor force which also makes ^{54}Ca a magic nucleus candidate. In addition, QRPA calculations on top of HF+BCS are performed to investigate the first $J = 2^+$ states of the calcium isotopic chain in order to explore the magicity of the ^{52}Ca and ^{54}Ca nuclei. We confirm that the tensor part of the interaction is quite essential in explaining the neutron subshell closure in ^{52}Ca and ^{54}Ca nuclei.

Investigation of the properties and dynamics of nuclei under effect of temperature provide even more detailed information about the structure and properties of nuclei. In the second part of this thesis, the effect of the temperature on the ground state and excited state properties of nuclei are investigated within finite temperature mean field models. Firstly, the temperature dependent the HF-BCS approximation has been used in the calculation of the ground state properties of nuclei. Pairing phase transitions from superfluid to the normal state are studied with respect to the temperature. The temperature dependence of the nuclear radii and neutron skin are also analyzed. An increase of proton and neutron radii is obtained in neutron rich nuclei especially above the critical temperature. Using different Skyrme energy functionals, it is found that the correlation between the effective mass in symmetric nuclear matter and the critical temperature depends on the pairing prescription. The temperature dependence of the nucleon effective mass is also investigated, showing that proton and neutron effective masses display different behavior below and above the critical temperature, due to the small temperature dependence of the density. Secondly, the effect of the temperature on the multipole response of nuclei is investigated within the fully self-consistent finite temperature RPA. It is shown that the low-energy part of the dipole and monopole spectrum is rather sensitive to the temperature. In particular, formation of the new low-energy modes are observed under temperature effects. Lastly, the effect of the temperature on the multipole response of open-shell nuclei is investigated within the FT-QRPA for the first time.

Keywords: Nuclear Structure, Mean-Field Theory, Hartree Fock, Giant Resonances, low-Energy Modes, Random Phase Approximation, Skyrme Interaction, Temperature.

YILDIZ TECHNICAL UNIVERSITY

GRADUATE SCHOOL OF NATURAL AND APPLIED SCIENCES

ÖZET

SONLU ÇEKİRDEKLERİN OLAĞANÜSTÜ İZOSPİN VE SICAKLIK KOŞULLARI ALTINDA ORTALAMA ALAN TEORİSİ İLE TANIMLANMASI

Esra YÜKSEL

Fizik Anabilim Dalı

Doktora Tezi

Tez danışmanı: Assoc. Prof. Dr. Kutsal BOZKURT

Eş danışmanı: Prof. Dr. Elias KHAN

Günümüzde, deneysel alanda meydana gelen gelişmeler ile birlikte nükleer kararlılık vadisi dışında yer alan çekirdeklerin incelenmesi oldukça popüler bir konu haline gelmiştir. Bu çerçevede, proton-nötron asimetrisi yüksek olan egzotik çekirdeklerde yapılan araştırmalar nükleer vadinin farklı bölgelerinde yer alan atomik çekirdeklerin davranışlarını anlamamızı sağlaması bakımından önemlidir. Teorik olarak, öz uyumlu ortamalama alan modelleri çekirdeklerin hem taban durum özelliklerini hem de uyarılmış durumlarını açıklamada oldukça başarılıdır.

Son yıllarda, Dev Rezonans enerji bölgesinin altında oluşan düşük enerjili uyarılmalar hem deneysel hem de teorik olarak oldukça popüler bir çalışma alanıdır. Özellikle düşük enerjili uyarılmaların nötron kabuğu, çekirdeklerin simetri enerjisi ve astrofiziksel olaylar ile ilişkili olduğu bilinmektedir. Ancak düşük enerjili uyarılmaların doğası ve davranışı halen açık değildir. Bu tezin ilk bölümünde, düşük enerjili ve yüksek enerjili dipol ve monopol uyarılmalar Skyrme HF+RPA yöntemi kullanılarak incelendi. Özellikle, düşük enerjili monopol ve dipol uyarılmaların davranışları geçiş yoğunluğu ve kollektivite hesaplamaları yardımı ile incelendi. Düşük enerjili uyarılmaların yüksek enerjili uyarılmalardan farklı olarak hem izoskaler (IS) hem de izovektör (IV) davranışlar gösterdiği anlaşıldı. Bunun yanı sıra, düşük enerjili monopol uyarılmaların tek parçacık uyarılması ile oluştuğu ve düşük enerjili monopol uyarılmaları meydana getiren tek parçacık uyarılmalarının spin-yörünge enerjilerinin analizinde kullanılabileceği gösterildi.

Son günlerde, nükleer kararlılık vadisi dışında yer alan çekirdeklerde yeni sihirli sayıların oluşumunun gösterilmesi oldukça dikkat çekmiştir. RIKEN'de gerçekleştirilen deneyler sonucu ^{54}Ca çekirdeğinin sihirli çekirdek olduğu kanıtlanmıştır. Çalışmamızın bu aşamasında kararlılık vadisi dışındaki çekirdeklerde tensör kuvvetinin tek-parçacık enerjileri üzerindeki etkisi Skyrme HF-BCS ve HFB yöntemleri ile incelendi. Tensör kuvvetinin nötron p ve f kabuklarında enerji düzeyleri arasındaki farkı arttırarak $^{52-54}$Ca çekirdeklerini sihirli çekirdek adayı yaptığı belirlendi. Ayrıca, QRPA kullanılarak $^{52-54}$Ca çekirdeklerini sihirliliği ilk $J = 2^{+}$ enerji kullanılarak da gösterildi. Tensör kuvvetinin $^{52-54}$Ca çekirdeklerinin kabuk yapısının değişiminde oldukça önemli bir rol oynadığı gösterildi.

Çekirdeklerin özelliklerinin sıcaklık etkisi altında incelenmesi, onların yapısı ve davranışı hakkında daha fazla bilgi sahibi olmamızı sağlayacaktır. Bu amaç ile, çekirdelerin taban durum ve uyarılmış durum özellikleri sıcaklığa bağlı ortalama alan teorileri olan FT-HFBCS ve FT-RPA (QRPA) ile incelendi. İlk olarak FT-HFBCS yaklaşımı kullanılarak sıcaklığın çekirdeklerin taban durum özellikleri üzerindeki etkisi incelendi. Kritik sıcaklıklarda çiftlenim özelliklerinin ortadan kalktığı ve nötron kabuk çapının arttığı anlaşıldı. Bunun yanı sıra, simetrik çekirdeklerin etkin kütlesi ve kritik sıcaklık arasındaki bağıntının çiftlenim özelliklerine bağlı olduğu gösterildi. Artan sıcaklıkla beraber yoğunlukta meydana gelen değişim ile proton ve nötron etkin kütlelerinin kritik sıcaklıkların altında ve üstünde farklı davranışlar gösterdiği anlaşıldı. İkinci olarak, sıcaklığın kapalı ve açık kabuk çekirdeklerin çoklu uyarılmaları üzerindeki etkisi FT-RPA (QRPA) kullanılarak incelendi. Düşük enerjili monopol ve dipol uyarılmaların sıcaklıkla beraber değişime uğradığı belirlendi. Ayrıca, yeni düşük enerjili uyarılmaların da sıcaklıktaki artış ile beraber ortaya çıktığı gösterildi.

Anahtar Kelimeler: Nükleer Yapı, Ortalama Alan Teorisi, Hartree Fock, Dev Rezonanslar, Düşük Enerjili Uyarılmalar, Bağımsız Faz Yaklaşımı, Skyrme Etkileşimi, Sıcaklık.

CHAPTER 1

INTRODUCTION

1.1 Literature Review

The history of nuclear physics started with the discovery of the radioactivity of Uranium by A. H. Becquerel in 1896. Then, the electron was found by J. J Thomson in 1897. Afterwards, the atomic nucleus was discovered in the Rutherford experiment in 1911 [1]. The progress continued with the observation of the neutron in early 1932 by Chadwick [2] and gained acceleration with the improvements in theoretical models and experimental facilities. The nucleus is defined as a quantum many-body system made of protons and neutrons and strongly interacting via the nuclear forces. Since then, the researchers strive to probe the structure of nuclei and to understand the behavior of nucleon-nucleon interactions.

In Figure 1.1, the nuclear landscape is presented as a function of the proton (Z) and neutron (N) numbers [3]. In this chart, the black and yellow squares represent stable and unstable nuclei, respectively. Nearly 300 stable isotopes are found in nature. Today, the properties of nuclei near the stability valley are well known with the current theoretical models and experimental results. However, there are still unanswered questions for the nuclei away from the stability valley. Exploration of nuclei with unusual proton-neutron numbers is one of the great challenges both in the experimental and theoretical nuclear physics. In recent years, it has become possible to reach information about exotic nuclei with the advances in experimental nuclear physics. These studies are quite important for improving our knowledge of the nucleon-nucleon interaction and the nuclear mean field as well as the to understand the formation and structure of nuclei away from the stabil-

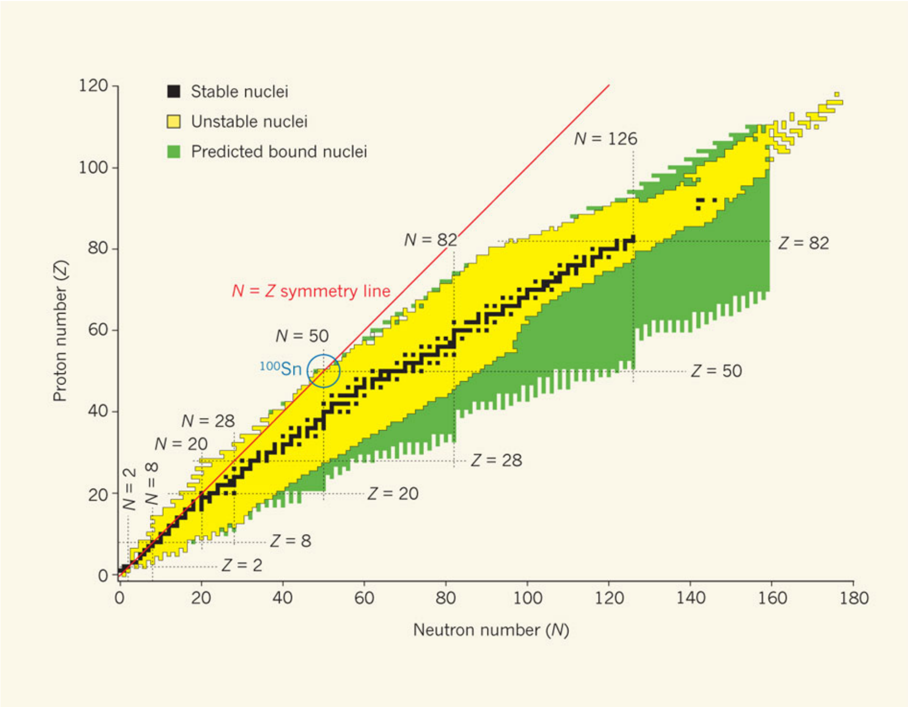

Figure 1.1 The valley of nuclear stability as a function of proton (Z) and neutron (N) numbers in nuclei. Black and yellow squares represent stable and unstable nuclei, respectively. Dotted lines show magic nuclei [3].

ity line. Among the nuclear models, the Liquid Drop Model (LDM) is known as the first primitive model of nuclei where the nucleus is considered as a liquid drop. The total binding energy of a nucleus can be calculated with a semi-empirical mass formula in which the quantum effects are also included. The LDM is able to explain the mechanism of the fission process. However, it is not adequate in the description of the shell structure and excited states of nuclei. Over the years, different theoretical models have been developed in order to probe the properties of nuclei. These models can be grouped into three parts: the ab initio method, the shell model and the self-consistent mean field model [4]. Today, the self-consistent mean field methods are the best in the description of the ground state and excited state properties of the nuclei over the entire nuclear chart.

In the ab initio method, the bare nucleon-nucleon interaction is used in the calculations. Despite the reliability of the results with the realistic interactions between the nucleons, the ab initio method creates great computational challenges. Due to this fact, ab initio calculations can only be performed for light nuclei.

In the shell model, which lies between the ab initio and the self-consistent mean field models, effective interactions are used for the microscopic description of the structure of the nucleus. The nucleons are assumed to move in a common potential which is created by all nucleons. The shell model can be performed within a limited model space of valence nucleons and it requires heavy computational performance like in the ab initio method. Thus, calculations are still a challenge for heavy nuclei.

The self-consistent mean field method is one of the most used and successful method in the description of the properties of medium and heavy nuclei. As in the shell model, the nucleons are supposed to move independently in a common (mean) potential which is generated by all nucleons of the system. The complex nuclear many-body problem is described by an energy functional of the density (EDF). Since the 1970's, the self-consistent mean field models are used to describe the structure and properties of medium heavy and heavy nuclei with much less computational cost when compared with the ab initio and shell models. Since it is difficult to determine the energy functional in its exact form, it is derived from an effective interaction. In the non-relativistic framework, Skyrme [5] and Gogny [6] interactions are well known phenomenological effective interactions in nuclei. Generally, the Skyrme interaction parameters are adjusted phenomenologically to experimental data of finite nuclei or nuclear matter properties. Over the years, Skyrme energy density functionals have gained considerable success in the description of the properties of the nuclei over the nuclear chart. The Skyrme Hartree-Fock approximation is rather successful in the determination of the ground state properties of nuclei (binding energies, radii and single particle spectrum) [7–9]. However, its success is limited to the closed shell nuclei around the stability line of the nuclear valley. In the description of nuclei through the drip lines, both continuum effects and pairing correlations must be considered. In the case of open shell nuclei, either the Hartree-Fock-BCS (HF+BCS) or the Hartree-Fock-Bogoliubov (HFB) approximations are used in the calculations. When compared with the HF+BCS, the HFB approximation gives better results for the nuclei away from the stability line. The success of the HFB approximation comes from the treatment of the pairing correlations. In the HFB method, the mean field and pairing field affect each other, thus providing a better description for the scattering of nucleon pairs to the continuum [10].

The Random Phase Approximation (RPA) is a suitable tool to calculate the nuclear excitations in closed shell nuclei [11,12]. Recently, the Skyrme RPA has been used in order to investigate the dipole response [13–20] and monopole response [21–25] of nuclei. In the case of open shell nuclei, the RPA should be extended to the Quasiparticle RPA (QRPA) in order to take into account the pairing correlations for the proper description of the nuclear excitations. The other important and challenging issue is the self-consistency of the RPA calculations, namely, usage of the same energy density functional in the ground state and the excited state calculations. Until recently, the RPA calculations were not fully self-consistent due to the neglected spin-orbit and Coulomb terms of the energy functionals in the residual p-h interaction. Recently, the fully self-consistent calculations have also been performed with the Skyrme energy density functionals [26, 27]. The self-consistency of the RPA calculations are quite important for the decoupling of spurious states from the spectrum of physical excitations.

The nuclear excited states are the best tools in order to probe the structure and properties of nuclei [9]. The properties of the Giant Resonances are mainly related with the nuclear observables and studied extensively over the years [9, 28–30]. Nowadays, the investigations of the multipole response of nuclei away from the β stability valley become a very active field with the progress in the experimental facilities. Especially, the formation of the low-energy dipole resonances or Pygmy Dipole Resonances (PDR) in neutron rich nuclei is a popular topic, both experimentally [31–34] and theoretically [9,35,36]. In neutron rich nuclei, with the modification of the nuclear potential, some of the neutron states become weakly bound. Due to these loosely bound neutron orbitals, the dipole mode becomes softer and lies in the low-energy part of the spectrum. Generally, the properties of the PDR is related with the symmetry energy and neutron skin thickness [37–39]. Also, it is known that the strength of the PDR could affect the neutron capture rates in r-process nucleosynthesis [9, 40]. Furthermore, the formation of the low-energy monopole states have been predicted theoretically in exotic nuclei [21–25]. Recently, the first measurements of the isoscalar monopole resonances have also been performed in exotic nuclei and formation of the low-energy monopole states was reported [41, 42]. To sum up, the nature and behavior of the low-energy modes are still unclear and model dependent. Due to their complex behavior and unclear structure, we choose the low-energy modes as the main subject of this thesis.

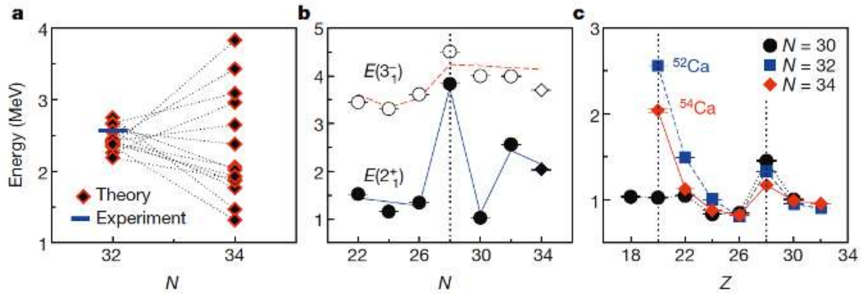

Figure 1.2 Excited-state energies of Ca isotopes and neighboring nuclei. The figure is taken from Ref. [50].

In the last decade, one of the most striking issue is the change of nuclear magic numbers far from the stability line. Today, the well known magic numbers of nuclei are: 2, 8, 20, 28, 50, 82 or 126 [43]. The nuclei which have these proton and neutron numbers are rather stable and called magic nuclei. However, theoretical and experimental results revealed that the magic numbers can change far from the stability line [44–49]. Recently, the experimental signatures about the new magic number N=34 have been obtained in Radioactive Isotope Beam Factory (RIBF) at RIKEN [50]. In Figure 1.2, the experimental results are shown for even-even Calcium nuclei and neighboring nuclei. An increase in the excitation energy of the first 2^+ state of ^{54}Ca nucleus is obtained which is an indication of the magicity. It has been suggested that the tensor part of the effective nuclear interaction can explain the change of magic numbers in exotic nuclei. The tensor force can change the single-particle (s.p.) levels considerably and lead to the formation of the subshell closures [51]. The results are quite important for understanding the nature of the nucleon-nucleon interaction far from the stability line and they indicate the shortcomings of the energy density functionals for the exotic nuclei. Thus, the effects of the tensor force on the single-particle energies and the magicity of ^{54}Ca nucleus have also been investigated within the framework of this thesis.

The effect of temperature on the ground state and excited states of nuclei is also important in order to understand the behavior of nuclei under extreme conditions. In order to investigate the static properties of nuclei, the mean field models are also extended to the finite temperature case [52–54]. Both Hartree-Fock-BCS [52, 53] and HFB models [55–59] are used in order to investigate the properties of nuclei at finite temperatures. It is known that the nuclei undergo a sharp phase transition at finite temperatures. As a consequence, the pairing correlations disappear at a critical temperature. In nuclei through the drip lines, the re-entrance of the pairing correlations can also occur. At finite temperatures, the static properties of nuclei change slightly. For instance, the single-particle energies, the proton and neutron radii and the effective mass of nuclei are affected by the temperature. Apart from the ground state properties, the effect of the temperature on the multipole response of nuclei is also an important issue. As it has been mentioned before, the formation of the low-energy modes in the multipole responses of nuclei are an active field of research both experimentally and theoretically. Since these low-energy modes are quite important for understanding the behavior of exotic nuclei, they should be investigated under different conditions. Recently, several experimental works have been devoted in order to investigate the temperature effects on the Giant Resonance widths and energies [60–64]. In addition, different theoretical models have been applied in order to study the effect of temperature on the excited states of nuclei [65–68]. The first study within the self-consistent finite temperature RPA framework was applied to the ^{40}Ca nucleus [69]. It was shown that the quadrupole response of the ^{40}Ca nucleus was quite sensitive to the temperature effects while the dipole response was not affected much by the temperature. The derivation of the Finite temperature QRPA equations has been given in Ref. [70]. Then, the finite temperature continuum-QRPA has been derived for the first time in Ref. [71]. The effect of the temperature has been emphasized for the low-energy part of the quadrupole response of ^{120}Sn. Recently, the effect of the temperature on the low-energy dipole and monopole modes of the nuclei have been investigated within the relativistic finite temperature RPA framework in Ref. [72]. It has been shown that new low-energy excitations appear in the monopole and dipole response of nuclei due to the temperature effects. Investigation of the multipole response of nuclei at finite temperatures remains a challenge both in the experimentally and theoretically. In particular, the investigation of the low-energy part of the excitation spectrum can provide valuable information about the nuclear excited states under extreme conditions.

In this thesis, all calculations are performed with the self-consistent mean field theories. The thesis is organized as follow: In Chapter 2, The Giant Resonances and their properties are given. The low-energy modes are also briefly introduced. In Chapter 3, The Microscopic Models used throughout the thesis are presented at zero temperature. The Skyrme interaction, Hartree -Fock and Random Phase Approximations are briefly sketched. In Chapters 4 and 5, the dipole and monopole responses of nuclei are investigated. In particular, the formation of low-energy modes in exotic nuclei are discussed. The behavior and nature of the low-energy modes and their relations with the properties of nuclei are presented. In Chapter 6, the effects of the tensor interaction on the formation of the new magic numbers away from the stability line are investigated. The HF+BCS and HFB models are employed and compared. Then, the first 2^+ states of the Ca nuclei are discussed in order to determine the magicity of the ^{54}Ca nucleus. In Chapter 7, The finite temperature extension of the HF-BCS is presented. The temperature dependence of the static properties of nuclei is investigated within this framework. In Chapter 8, The Random Phase Approximation at finite temperature is briefly introduced. The effects of the temperature on the multipole response of the selected nuclei are investigated. The temperature effect on the low-energy part of the spectrum is also discussed. The First applications of the FT-QRPA are also investigated. In Chapter 9, Conclusions and Perspectives are given.

1.2 Objectives of the Thesis

In this thesis, we aim at studying the ground state and excited state properties of nuclei using the self-consistent mean field methods.

In the first part, we investigate the nature and behavior of low-energy modes in the monopole and dipole spectra of nuclei at zero temperature. In order to get a clear understanding, we work on closed-shell magic-doubly magic nuclei where pairing correlations are not present. The formation and the possible occurrence of the low-energy modes are investigated for selected nuclei using the HF+RPA and different Skyrme energy density functionals. In addition, the effects of the tensor force on the single-particle energies and on the possible formation of the new nuclear magic number N=34 are also investigated within the HF+BCS and HFB frameworks. The first 2^+ states of even-even Calcium isotopes are explored with QRPA in order to decide of the magicity of the ^{54}Ca nucleus.

In the second part of the thesis, we aim at investigating the properties of finite nuclei within the self-consistent mean field framework at finite temperature. Both the HF+BCS and RPA are extended to finite temperature HF+BCS and finite temperature RPA (QRPA) in order to perform the calculations under temperature effects. We investigated the effects of the temperature on the ground state and excited states of nuclei. In particular, the possible formation of new low-energy modes under temperature effects are discussed.

1.3 The Original Contributions of This Work

The original contributions of this thesis can be summarized as follows:

In Chapter 4, the formation of low-energy modes in the dipole spectra of nuclei is shown. This mode is generally called as pygmy dipole resonance (PDR). In order to understand the nature and behavior of this mode, we made an analysis over nuclear isotope chains. It is found that the main pattern of the PDR transition densities does not mainly depend on neutron excess but it has rather a complicated character, far from the PDR classical picture of neutron skin oscillations around a proton-neutron core. The proton and neutron transition density analysis shows that the PDR is usually not pure isoscalar (IS) or isovector (IV) in the interior part of nuclei or pure IV outside. Instead, it often shows a complex generic isoscalar and isovector feature which makes it different from the pure isovector nature of the GDR. It has been shown that the PDR involves several particle-hole pairs, showing a non-negligible collectivity which is different from the GDR behavior. The results also indicate that isoscalar probes (for instance, α scattering experiments) can be used in order to excite PDR's.

In Chapter 5, the soft isoscalar monopole response is predicted in doubly magic ^{208}Pb, ^{100,132}Sn nuclei using HF+RPA formalism and Skyrme energy density functionals. Pure particle-hole excitations are predicted in the low-energy region. Due to the specific L=0 multipolarity, these soft modes probe the shell structure through $2\hbar\omega$ gap excitations. They can be related to the spin-orbit splitting, thus providing a complementary information to transfer reaction measurements.

In Chapter 6, we employ both HFB and HF+BCS methods to study the ground states of N=34 isotones with the aim of exploring the possible magic nature of ^{54}Ca. We show that the effect of a tensor force component quite enhances the energy difference between the s.p. states, thus leading to a subshell closure in ^{54}Ca. Furthermore, the tensor force leads to an increased energy of the first 2^+ state in the calcium isotopic chain. Both ^{52}Ca and ^{54}Ca show a magic nature. Especially, the first 2^+ state of ^{54}Ca is well reproduced when compared with the experimental results. The results indicate the importance of the tensor force on the shell evolution of $p-f$ shell nuclei.

In Chapter 7, we have investigated the ground state properties of different nuclei within the finite temperature HF+BCS framework with Skyrme interactions. A substantial increase in the proton and neutron radius of neutron rich nuclei is obtained above the critical temperatures. A correlation is obtained between the effective mass of Skyrme energy density functionals and the critical temperature of ^{120}Sn nucleus, relating $m*$, T_c and $\Delta(T=0)$. It has been shown that with the enhancement in the effective mass, the level densities around the Fermi level and pairing gap increase which eventually leads to an increase in the critical temperature. However, this correlation depends on the pairing prescription. The temperature dependence of the effective k-mass of protons and neutrons is also investigated. Due to the changes in the proton and neutron densities, the effective nucleon masses show rather different fine behaviors before and after the critical temperature, which constitutes a new feature.

In Chapter 8, the multipole response of nuclei is investigated within the fully-self consistent FT-RPA framework using Skyrme energy density functionals. It is shown that the high-energy part of the excitation spectrum in not sensitive to the temperature. However, the low-energy part changes considerably due to the thermal population of the single particle levels. Finally, the temperature effect on the dipole response of open shell nuclei is briefly discussed within the FT-QRPA framework for the first time.

CHAPTER 2

GIANT RESONANCES IN ATOMIC NUCLEI

2.1 Introduction

As a quantum many-body system, understanding the behavior and structure of nuclei constitutes the major part of nuclear physics. The multipole response of nuclei to an external field is known to be a relevant tool to analyze the nuclear structure [9, 73]. Giant Resonances (GR) are known as small amplitude and high frequency collective states of nuclei with typical energies between 12-30 MeV. They can be used as a tool to probe the internal structure of nuclei. Giant resonances exhaust a large part of the Energy Weighted Sum Rule (EWSR) and their structure changes smoothly with the nucleon number [73]. Although they have been investigated mainly around the β-stability line of the nuclear valley, the measurement of GR's in exotic nuclei is still a challenge for the experimental activities.

In Figure 2.1, we present a schematic picture of E1 and E2(E0) single-particle transitions between shell model spaces. From a microscopic view point, Giant resonances are defined as a coherent superposition of particle-hole excitations [73]. Since many p-h excitations are feeding the Giant resonances, they are also known as the collective excitations of nuclei. The RPA (QRPA) is an appropriate method in order for studying the excitations of nuclei where particle-hole excitations are created and interact via the residual particle-hole interaction. Excitation energies, strength, transition densities and the collectivity properties are important features in the interpretation of the Giant Resonances.

The properties of the Giant Resonances are well known and described in many textbooks and reviews extensively. In this part, we just briefly discuss the properties of the GR's

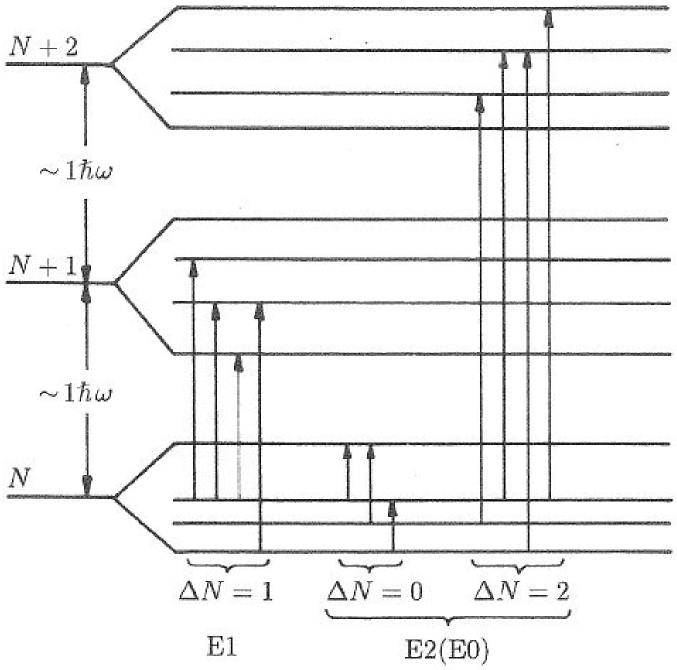

Figure 2.1 Schematic picture of E1 and E2(E0) single-particle transitions between shell model spaces.

which are the subject of this thesis. For a general review, we refer the reader to Ref. [73].

2.1.1 Classification of Giant Resonances

Giant Resonances can be classified according to their L (orbital angular momentum), S (spin) and T (isospin) quantum numbers as can be seen in Figure 2.2. According to their L quantum numbers, they are classified as Monopole (L=0), Dipole (L=1) and Quadrupole (L=2). The spin quantum number (S) determines whether the excitation is Electric or Magnetic. The S=0 mode is called an Electric excitation since spin states are in phase. S=1 is called Magnetic excitation since spin states are out of phase. In addition, the isospin quantum number (T) determines the Isoscalar (IS) or Isovector (IV) nature of the vibration. While T=0 is known as an isoscalar excitation, T=1 corresponds to an isovector one.

Among the nuclear collective modes, the Isovector Giant dipole resonance (IVGDR) is the most studied nuclear mode. The GDR was firstly seen in the experiments of Bothe and Gentner [74] and then confirmed by the photo-absorption experiments of Baldwin

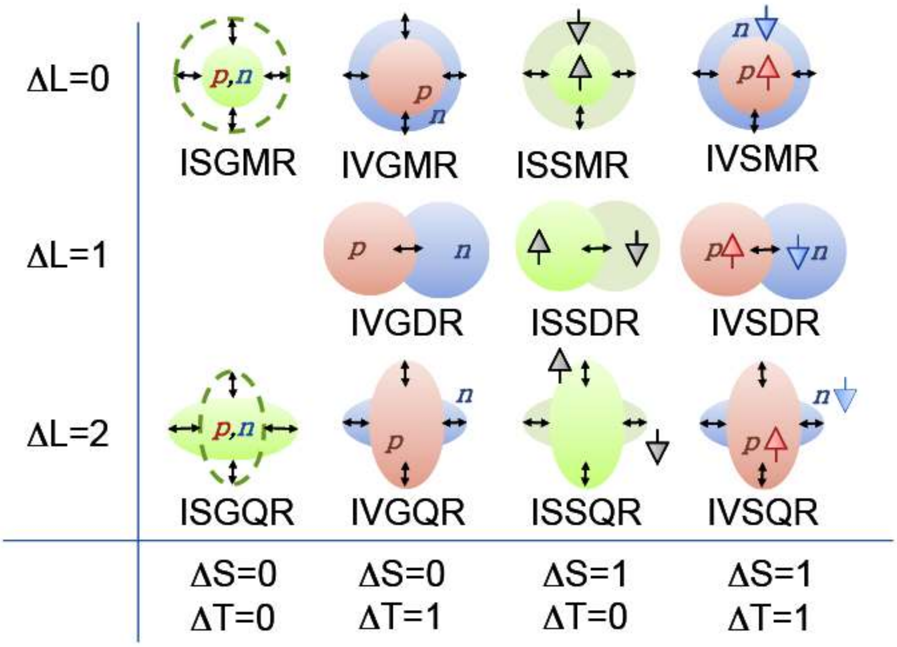

Figure 2.2 Classification of Giant Resonances [73].

and Klaiber [75]. The theoretical predictions and interpretations of this mode can be found in Refs. [28–30]. The Isovector Giant dipole resonances (IVGDR) occur in all nuclei and their excitation energies can be obtained with the $E_x = 80A^{-1/3}$ MeV empirical law for $A > 50$ nuclei. Generally, the widths of the resonances changes between 4-8 MeV, depending on the mass number of the nuclei. While the IVGDR peak can be well described by a Lorentzian shape in heavier nuclei, the strength can be split into several peaks in deformed nuclei. It is known that the low-energy part of the IVGDR is closely related with the neutron skin and symmetry energy of nuclei [9].

The Isoscalar Giant Monopole Resonance (ISGMR) was first discovered in 1977 by means of inelastic α scattering and it is known as the compressional or breathing mode of nuclei. The ISGMR peak energy can be obtained with the $E_x = 80A^{-1/3}$ MeV empirical law as in the case of the IVGDR. For heavier nuclei, the ISGMR has a concentrated strength and its width varies between 2.5-4.0 MeV. In deformed nuclei, the ISGMR has a fragmented shape and its strength is broader. Also, the strength has a fragmented shape in lighter nuclei. The ISGMR properties are mainly related to the nuclear matter incompressibility K_∞. Since the nuclear matter incompressibility cannot be measured experimentally, the ISGMR excitation energies are used in order to determine it. However, there are still discrepancies between the experimental and theoretical results of the ISGMR. In order to obtain a clear idea about the incompressibility of nuclear matter, we need further experimental results on the ISGMR in isotopic nuclear chains. In the last decade, both experimental [41, 76–78] and theoretical [21–25] works have been devoted to the GMR.

The first experimental signatures of the Isoscalar Giant Quadrupole Resonance (ISGQR) were obtained in inelastic electron and proton scattering experiments in the 1970's [79, 80]. The ISGQR resonance energy can be well produced by the expression $E_x = 64.7A^{-1/3}$ MeV for heavier nuclei. In these nuclei, it exhausts almost all EWSR and has a narrow resonance width. It has been known that for even-even nuclei the first excited state is a 2^+. The first 2^+ state is also an indicator for the magicity and reflects the shell structure of nuclei. Especially, the first 2^+ state energies of magic nuclei vary between the 2.0-4.0 MeV while this energy is lower for open shell nuclei due to the nuclear pairing phenomenon.

2.1.1.1 Low-Energy Excitation Modes

In recent years, investigation of nuclei with an extreme ratio of neutrons to protons has gained considerable attention due to the theoretical and experimental improvements in nuclear physics. Especially in neutron rich nuclei, the presence of a neutron skin (i.e., a thin layer of neutrons) outside the spin-isospin saturated core was foreseen by different theoretical models [81, 82]. Because of the weak binding energy of these excess neutrons, it is expected that the dipole mode will be rather soft and below the Giant Dipole Resonance. This low-lying strength is usually called the Pygmy Dipole Resonance (PDR) and often interpreted as the oscillation of the neutron skin against the core [9, 35]. The PDR is a result of the neutron excess in nuclei and such a mode also gives the knowledge of the isospin-dependent components of effective nuclear interactions, which gains importance in nuclei with a large proton-neutron asymmetry [9].

In addition, the pygmy dipole resonance is associated with the static properties of nuclei, for instance the neutron skin thickness and the nuclear symmetry energy. The PDR also plays a relevant role in astrophysics, in the r-process nucleosynthesis [37–40]. However, the nature and the behavior of the PDR is still under debate: is it a single-particle excitation or a collective motion ? Actually, the PDR displays different behaviors with respect to the selected nucleus and the theoretical model. In non-relativistic models the PDR is usually interpreted as single-particle excitations. In a study with the RQRPA approximation, the PDR is interpreted as the non-resonant independent single-particle excitations of the loosely bound neutrons in light Oxygen and Calcium isotopes. The pattern of the PDR changes with increasing neutron number and becomes a quite collective resonant oscillation of the neutron skin [9, 35, 36]. For instance, the PDR can be described as of isoscalar character (i.e., an in-phase motion of protons and neutrons) inside the nucleus and an out-of-phase motion (isovector character) outside the nucleus [35]. This is the so-called classical picture of the PDR.

First evidences of low-lying modes were seen in light halo nuclei in the reaction ^{208}Pb (^{11}Li,^{9}Li) at 800 MeV/nucleon [31]. With more recent experiments in neutron-rich Oxygen isotopes the occurrence of pygmy dipole resonances have been confirmed below the giant dipole resonance and it has been observed that the dipole response is changing with the neutron number [32, 83–85]. Also, strongly bound and doubly magic nucleus ^{16}O has no low-lying mode. E1 strength distributions in the doubly magic ^{40}Ca nucleus and the neutron rich ^{48}Ca nucleus have been studied in high resolution photon scattering experiments by Hartmann et al. [33]. The experimental results show that the summed low-lying strength in the neutron-rich ^{48}Ca nucleus is larger than in the ^{40}Ca (N=Z) nucleus and it depends on the neutron excess of nuclei. The first experiment to investigate the pygmy dipole resonance in the ^{68}Ni nucleus was recently performed with virtual photon scattering technique and low-lying strength at 11 MeV was found with 5% of EWSR [86]. In addition, the heavy Sn isotopic chain is a good case for investigating the nature of low-lying modes. Neutron-rich tin isotopes were studied at GSI with electromagnetic probes. [34] and by nuclear resonance fluorescence (NRF) techniques [87]. The results indicate the presence of some low-lying strength below the GDR, at about 10 MeV. Theoretical investigations of low-lying modes both in Sn isotopes and different isotopic chains are also confirming these experimental results. The main conclusion of these studies is that the dipole strength fragmentation increases and the centroid energy decreases with increasing neutron excess [9, 13, 35, 88].

Proton and neutron transition densities are relevant quantities for studying the behavior of excited states. Analyzing the transition density gives information about the character of excited states of nuclei and their radial dependence, therefore one needs to study the behavior of low-lying dipole modes in much more details. The results of previous works indicate that proton and neutron transition densities are oscillating out of phase in the case of the GDR, displaying an isovector (IV) behavior [9, 35]. Most microscopic models predict that in the low-lying mode, protons and neutrons oscillate in phase in the nuclear interior that is displaying isoscalar (IS) motion, with neutron dominated isovector (IV) motion on the surface [9, 89]. However, this behavior of protons and neutrons is not systematic for low-lying modes of excitation. While theoretical and experimental studies always predict the behavior of Giant Dipole Resonances as isovector, the nature of Pygmy Dipole Resonances under excitation is not clear. Recently, in a theoretical work about the pygmy dipole structures using RHB+RQRPA method, the isospin properties and transition densities of ^{140}Ce nucleus were investigated and it has been shown that the pygmy mode has a complex pattern. More recently, experiments with $(\alpha, \alpha', \gamma)$ and (γ, γ') reactions on neutron-rich ^{138}Ba, ^{140}Ce and ^{124}Sn nuclei gave important results about the structure of the PDR, showing that it is splitted into two parts and display different underlying structures [89–91]. It should be noted that the analysis of the transition densities has been decisive in order to obtain these results.

Apart from the low-lying dipole mode, formation of soft (low-energy) modes can also be seen in the case of monopole excitations of exotic nuclei. It is known that soft modes are a general feature of neutron-rich nuclei [9]. In the case of the soft monopole response, the drip line ^{60}Ca nucleus was analyzed in Ref. [21] with Hartree Fock plus Random Phase Approximation (HF+RPA) and Skyrme interaction. The occurrence of a low energy response was predicted between 4.0 MeV and 12.0 MeV excitation energy, and it is due to the neutron excitations with a minor effect of the residual interaction. Recently, low-energy monopole strength in exotic nickel isotopes was also studied with HF+RPA and relativistic RHB+RQRPA models [23]. Both relativistic and non-relativistic approaches also predicted the occurrence of a low-energy monopole strength between 10 MeV and 15 MeV. It was shown that these soft monopole modes were non-collective and thus could be sensitive to the shell structure and the single-particle spectrum in exotic neutron-rich nuclei: it has been suggested that soft monopole modes could provide information on the $2\hbar\omega$ gap of nuclear shell structure. In this framework, additional work needs to be undertaken on the monopole response of medium and heavy nuclei to investigate the relationship between single-particle spectroscopy and the low-lying monopole strength. One of the aim of the present work is to investigate how these very non-collective states could bring valuable information on the spin-orbit field.

CHAPTER 3

MICROSCOPIC MODEL AT ZERO TEMPERATURE

The atomic nucleus is a quantum many-body system in which nucleons interact with one one another via the strong nuclear force. The investigation of the static and dynamical properties of atomic nuclei constitutes the main themes of both the theoretical and experimental nuclear physics. The self-consistent mean-field models are appropriate tools for the description of the properties of the medium and heavy nuclei which are used in many works since the 1970's [4]. In the mean field models, the nucleons are supposed to move independently in a common potential created by all nucleons. In this approximation, the calculations are not demanding and the results are encouraging for medium and heavy nuclei. Since the self-consistent mean field models are rather successful in the description of atomic nuclei throughout the nuclear valley, we have used non-relativistic self-consistent mean field models in this work.

Within the scope of this thesis, the static properties of nuclei are calculated using the Hartree-Fock (HF) method. In the case of open shell nuclei, Hartree-Fock plus Bardeen-Cooper-Schrieffer (HF+BCS) or Hartree-Fock-Bogoliubov (HFB) approximations are used in order to take into account pairing correlations in nuclei. For the nuclear excited states, the Random Phase Approximation (RPA) or Quasiparticle RPA (QRPA) are applied in closed shell and open shell nuclei, respectively. The success of the HF and RPA comes from the use of the effective nucleon-nucleon interactions in the calculations. In the literature, two effective nucleon-nucleon interactions are generally used: Gogny and Skyrme interactions. The Gogny force is a finite range nucleon-nucleon interaction which has been introduced by Brink and Boeker in the 1967's and parametrized by Dechargé and

Gogny to be used in the self-consistent mean field calculations [6]. The Skyrme interaction is a well known zero-range, density-dependent nucleon-nucleon interaction introduced by Skyrme in 1958's [5]. The parameters of the Skyrme interaction are obtained by fitting the experimental results of some well known nuclei. The Skyrme interaction is used over the years in many theoretical investigations due to its success in the prediction of the properties of nuclei. We have performed all the calculations self-consistently, namely, the same Skyrme energy density functional is used in the Hartree-Fock and RPA calculations. In this part of the thesis, we will present the Skyrme effective interaction and the microscopic models which are used throughout the thesis.

3.1 The Skyrme Interaction

The Skyrme interaction is a zero-range, density-dependent nucleon-nucleon interaction which was proposed by T. H. R. Skyrme in 1959 [5] . The standard form of the Skyrme interaction is given by:

$$\begin{aligned} V_{Sky}(\mathbf{r}_{12}) = {} & t_0(1+x_0\hat{P}_\sigma)\delta(\mathbf{r}_{12}) + \frac{1}{2}t_1(1+x_1\hat{P}_\sigma)[\hat{\mathbf{k}}'^2\delta(\mathbf{r}_{12}) + \delta(\mathbf{r}_{12})\hat{\mathbf{k}}^2] \\ & + t_2(1+x_2\hat{P}_\sigma)\hat{\mathbf{k}'}\cdot\delta(\mathbf{r}_{12})\hat{\mathbf{k}} \\ & + \frac{1}{6}t_3(1+x_3\hat{P}_\sigma)\rho^\alpha(\mathbf{R})\delta(\mathbf{r}_{12}) \\ & + iW_0(\hat{\sigma}_1+\hat{\sigma}_2)\cdot[\hat{\mathbf{k}'}\times\delta(\mathbf{r}_{12})\hat{\mathbf{k}}] \end{aligned} \tag{3.1}$$

In these equations, $\mathbf{r}_{12} = \mathbf{r}_1 - \mathbf{r}_2$ with $\mathbf{R} = (\mathbf{r}_1 + \mathbf{r}_2)/2$. The operator $\hat{\mathbf{k}} = -\frac{i}{2}(\vec{\nabla}_1 - \vec{\nabla}_2)$ is the relative momentum acting to the right and $\hat{\mathbf{k}'}$ is its complex conjugate acting to the left. σ is the Pauli spin operator and $\hat{P}_\sigma = \frac{1}{2}(1+\hat{\sigma}_1\cdot\hat{\sigma}_2)$ is the spin-exchange operator. The constants $t_0, t_1, t_2, t_3, x_0, x_1, x_2, x_3, \alpha, W_0$ are Skyrme parameters which can be obtained by fitting either the experimental properties of some nuclei like binding energies and r.m.s. radii or bulk properties (incompressibility and symmetry energy) of nuclear matter. Since the Skyrme interactions are rather successful in the description of the properties of nuclei, all the calculations are performed with them in this thesis. The Skyrme interactions are selected for each calculation according to their fitting method and the success in describing these.

3.1.1 Skyrme Energy Density Functional

The total energy density functional of a nucleus is a local functional and given by [4]

$$
\begin{aligned}
E[\rho,\kappa,\kappa^*] &= T + E_{Skyrme}[\rho] + E_{Coul.}[\rho_p] + E_{pair}[\rho,\kappa,\kappa^*] \\
&= \int d^3\mathbf{r}[T(\mathbf{r}) + \mathscr{E}_{Skyrme}(\mathbf{r}) + \mathscr{E}_{Coul.}(\mathbf{r}) + \mathscr{E}_{pair}(\mathbf{r})].
\end{aligned} \tag{3.2}
$$

where the kinetic energy term is defined as

$$
T(\mathbf{r}) = \frac{\hbar^2}{2m_p}\tau_p + \frac{\hbar^2}{2m_n}\tau_n \tag{3.3}
$$

and the Skyrme energy term can be written as,

$$
\mathscr{E}_{Skyrme}(\mathbf{r}) = \mathscr{E}_0 + \mathscr{E}_3 + \mathscr{E}_{eff.} + \mathscr{E}_{fin.} + \mathscr{E}_{so} + \mathscr{E}_{sg}. \tag{3.4}
$$

there, $\mathscr{E}_0$ is the zero range term, $\mathscr{E}_3$ is the density dependent term, $\mathscr{E}_{fin}$ is the finite range term, $\mathscr{E}_{eff.}$ is the effective mass term, $\mathscr{E}_{so}$ is the spin-orbit term and $\mathscr{E}_{sg}$ is the tensor coupling term due to the spin and gradient. They are defined as:

$$
\mathscr{E}_0 = \frac{1}{4}t_0\left[(2+x_0)\rho^2 - (2x_0+1)(\rho_p^2+\rho_n^2)\right], \tag{3.5}
$$

$$
\mathscr{E}_3 = \frac{1}{24}t_3\rho^\sigma\left[(2+x_3)\rho^2 - (2x_3+1)(\rho_p^2+\rho_n^2)\right], \tag{3.6}
$$

$$
\begin{aligned}
\mathscr{E}_{eff} &= \frac{1}{8}\left[t_1(2+x_1) + t_2(2+x_2)\right]\tau\rho \\
&+ \frac{1}{8}\left[t_2(2x_2+1) - t_1(2x_1+1)\right](\tau_p\rho_p + \tau_n\rho_n),
\end{aligned} \tag{3.7}
$$

$$
\begin{aligned}
\mathscr{E}_{fin} &= \frac{1}{32}\left[3t_1(2+x_1) - t_2(2+x_2)\right](\nabla\rho)^2 \\
&- \frac{1}{32}\left[3t_1(2x_1+1) + t_2(2x_2+1)\right]\left[(\nabla\rho_p)^2 + (\nabla\rho_n)^2\right],
\end{aligned} \tag{3.8}
$$

$$
\mathscr{E}_{so} = \frac{1}{2}W_0\left[\mathbf{J}.\nabla\rho + \mathbf{J}_p.\nabla\rho_p + \mathbf{J}_n.\nabla\rho_n\right], \tag{3.9}
$$

$$
\mathscr{E}_{sg} = -\frac{1}{16}(t_1x_1 + t_2x_2)\mathbf{J}^2 + \frac{1}{16}(t_1 - t_2)\left[\mathbf{J}_p^2 + \mathbf{J}_n^2\right] \tag{3.10}
$$

where we write $\rho(r) = \rho$ to simplify the equations. In these expressions $\rho = \rho_p + \rho_n$ and $\mathbf{J} = \mathbf{J}_p + \mathbf{J}_n$. In addition, ρ, J and τ are particle, spin-orbit and kinetic energy densities, respectively. They are defined as

$$\rho_q(\mathbf{r}) = \sum_{i,\sigma} |\varphi_i(r,\sigma,q)|^2, \tag{3.11}$$

$$\tau_q(\mathbf{r}) = \sum_{i,\sigma} |\nabla\varphi_i(r,\sigma,q)|^2, \tag{3.12}$$

$$\mathbf{J}_q(\mathbf{r}) = -i \sum_{i,\sigma,\sigma'} \varphi_i^*(r,\sigma,q)[\nabla\varphi_i(r,\sigma',q) \times \langle\sigma|\sigma|\sigma'\rangle], \tag{3.13}$$

where $\varphi_i(r,\sigma,q)$ is the single-particle wave function and i, σ, and q are orbital, spin and isospin quantum numbers, respectively. The Coulomb term of the energy functional is:

$$\mathscr{E}_{Coul.}(\mathbf{r}) = \frac{e^2}{2}\int\int d^3r' d^3r \frac{\rho_p(\mathbf{r})\rho_p(\mathbf{r}')}{|\mathbf{r}-\mathbf{r}'|} - \frac{3e^2}{4}\left(\frac{3}{\pi}\right)^{1/3}\int d^3r \rho_p^{4/3}(\mathbf{r}). \tag{3.14}$$

Due to the finite range of the Coulomb interaction, an approximate exchange term is added to the functional which is known as the Slater approximation for Coulomb exchange [92]. Lastly, for open shell nuclei, the pairing functional can be written as

$$\mathscr{E}_{pair}[\rho,\kappa,\kappa*] = \int d^3r V(\rho(\mathbf{r})) \sum_{q=p,n} \left|\tilde{\rho}_q(\mathbf{r})\right|^2 \tag{3.15}$$

where $V(\rho(\mathbf{r}))$ is the density-dependent pairing interaction.

3.1.2 Tensor Part of the Skyrme Interaction

Although a tensor interaction was included in the original form of Skyrme interaction, it has been ignored in most of the calculations in the past [51]. The effect of the tensor force on the shell structure of nuclei has gained attention with more recent the experimental [93–95] and theoretical results [51,96] and there is a growing interest in this topic in the last decades [51,97–100]. The tensor component of the effective N-N interaction contributes to the spin-orbit part of the effective interaction and thus, it can affect considerably the single-particle (s.p.) energies [51,97]. For the tensor force, the triplet-even and triple-odd zero-range tensor terms are defined as [5]

$$\begin{aligned} \upsilon_T = & \frac{T}{2}\left[(\sigma_1.\mathbf{k}')(\sigma_2.\mathbf{k}') - \frac{1}{3}(\sigma_1.\sigma_2)\mathbf{k}'^2\right]\delta(\mathbf{r}_1-\mathbf{r}_2) \\ & + \frac{T}{2}\delta(\mathbf{r}_1-\mathbf{r}_2)\left[(\sigma_1.\mathbf{k})(\sigma_2.\mathbf{k}) - \frac{1}{3}(\sigma_1.\sigma_2)\mathbf{k}^2\right] \\ & + U\left[(\sigma_1.\mathbf{k}')\delta(\mathbf{r}_1-\mathbf{r}_2)(\sigma_2.\mathbf{k})\right] \\ & - \frac{1}{3}U(\sigma_1.\sigma_2)\times[\mathbf{k}'.\delta(\mathbf{r}_1-\mathbf{r}_2)\mathbf{k}], \end{aligned} \tag{3.16}$$

in this expression, $\mathbf{k} = (\nabla_1 - \nabla_2)/2i$ and $\mathbf{k}' = -(\nabla_1 - \nabla_2)/2i$ are momentum operators which act on the right and left, respectively. T and U are coupling constants and represent the strength of the triplet-even and triplet-odd tensor interactions. The contribution of the tensor part and central exchange term to the energy density is

$$\Delta E = \frac{1}{2}\alpha(J_n^2 + J_p^2) + \beta J_n J_p. \tag{3.17}$$

Here, J is defined as the spin-orbit density:

$$J_q(r) = \frac{1}{4\pi r^3}\sum_i \upsilon_i^2(2j_i+1)\times\left[j_i(j_i+1) - l_i(l_i+1) - \frac{3}{4}\right]R_i^2, \tag{3.18}$$

where $q = 0(1)$ represents neutrons (protons) and $i = n, l, j$ runs over all states having the given q. In the HF+BCS framework, the occupation probability of each orbital is given by υ_i^2 and R_i^2 is the radial part of the wave function. The Spin-orbit potential with the central exchange and tensor terms is,

$$U_{S.O.}^{(q)} = \frac{W_0}{2r}\left(2\frac{d\rho_q}{dr} + \frac{d\rho_{q'}}{dr}\right) + \left(\alpha\frac{J_q}{r} + \beta\frac{J_{q'}}{r}\right) \tag{3.19}$$

where, the first term on the right hand side comes from the Skyrme spin- orbit interaction and the second term includes both the central exchange and the tensor contributions. In equation 3.19, α and β are defined as $\alpha = \alpha_C + \alpha_T$, $\beta = \beta_C + \beta_T$. The central exchange terms are defined as,

$$\alpha_C = \frac{1}{8}(t_1 - t_2) - \frac{1}{8}(t_1x_1 + t_2x_2), \tag{3.20}$$

$$\beta_C = -\frac{1}{8}(t_1x_1 + t_2x_2), \tag{3.21}$$

and the tensor interaction terms are given by

$$\alpha_T = \frac{5}{12}U, \tag{3.22}$$

$$\beta_T = \frac{5}{24}(T+U). \tag{3.23}$$

In the Hartree-Fock (HF) type of description, the tensor force is either added directly to the known Skyrme interactions (e.g., SLy5+T [51]) or all Skyrme terms including the tensor component are refitted on the empirical ground state properties (e.g., the TIJ family of Skyrme forces, see Ref. [96]). Detailed explanations and more information about the tensor force can be found in Refs. [51,97].

In this thesis, the effects of the tensor force on the single-particle energies of nuclei are investigated. Since the tensor force has an important effect on the single-particle levels, it can lead to the formation of new nuclear magic numbers which is a popular topic in recent years. In our calculations, we use SLy5+T and T44 to illustrate the tensor force effects. The tensor interaction parameters are α_T =-170 MeV.fm^5, β_T =100 MeV.fm^5 for SLy5+T and α_T =8.96 MeV.fm^5, β_T =113.02 MeV.fm^5 for T44.

3.1.3 Pairing Correlations

Skyrme-type forces need to be complemented by an additional effective pairing interaction, which has to be specified in Skyrme HFB or HF+BCS calculations. In this thesis, zero-range/contact pairing interaction is used in the calculations of open shell nuclei. This interaction depends on the nuclear density and defined as [101]:

$$V_{pair}(\mathbf{r}_1,\mathbf{r}_2) = V_0\left[1-\eta\left(\frac{\rho(\mathbf{r})}{\rho_0}\right)\right]\delta(\mathbf{r}_1-\mathbf{r}_2). \tag{3.24}$$

Here, $\rho_0 = 0.16\ fm^{-3}$ is the nuclear saturation density and V_0 is an interaction strength which can be determined either by adjusting the ground state properties of the selected nuclei or using $12/\sqrt{A}$ empirical rule. One can choose η=1, 0 or 0.5 for the surface, volume and mixed pairing interactions, respectively.

3.2 Static Mean Field

3.2.1 Variational Derivation of Hartree-Fock Equations

In this section, the Hartree-Fock (HF) equations are derived from a variational principle. In the HF approximation, the wave function is a Slater determinant,

$$|\varphi\rangle = \left(\prod_{i=1}^{A} c_i^\dagger\right)|0\rangle\,, \tag{3.25}$$

where $c_i^\dagger$ and c_i are particle creation and annihilation operators, respectively. The Hamiltonian of the system can be written in the second quantization as

$$H = \sum_{ij} T c_i^\dagger c_j + \frac{1}{4}\sum_{ijkl}\sum_{ijkl} \langle ij|\bar{v}|kl\rangle_A\, c_i^\dagger c_j^\dagger c_l c_k. \tag{3.26}$$

Here, T is the kinetic energy and $\langle ij|\bar{v}|kl\rangle_A$ is the antisymmetrized two-body interaction, respectively. The antisymmetrized two-body interaction is given by

$$\langle ij|\bar{v}|kl\rangle_A = \langle ij|v|kl - lk\rangle\,, \tag{3.27}$$

and the single-particle density matrix is defined as

$$\rho_{ij} = \langle i|\rho|j\rangle = \langle\varphi|c_j^\dagger c_i|\varphi\rangle \tag{3.28}$$

which satisfies $\rho^2 = \rho$.

The expectation value of the Hamiltonian of the system can be written in terms of ρ,

$$\begin{aligned} E[\rho] = \langle\varphi|H|\varphi\rangle &= \sum_{ij}\langle i|T|j\rangle\,\rho_{ji} + \frac{1}{4}\sum_{ijkl}\langle ij|\bar{v}|kl\rangle_A\,\rho_{ki}\rho_{lj} \\ &= \sum_{ij}\langle i|T|j\rangle\,\rho_{ji} + \frac{1}{4}\sum_{ijkl}\langle ij|\bar{v}|kl\rangle_A\,(\rho_{ki}\rho_{lj} - \rho_{kj}\rho_{li}) \\ &= \sum_{ij}\langle i|T|j\rangle\,\rho_{ji} + \frac{1}{2}\sum_{ijkl}\langle ij|\bar{v}|kl\rangle\,\rho_{ji}\rho_{lk}. \end{aligned} \tag{3.29}$$

The energy functional is minimized with respect to the variations of the single-particle density matrix,

$$\delta[E[\rho] - Tr\Lambda(\rho^2 - \rho)] = 0, \tag{3.30}$$

where, Λ is a matrix of Lagrange multipliers. The HF Hamiltonian is defined as

$$h_{ij} = \frac{\partial E[\rho]}{\partial \rho_{ji}} = \langle i|T|j\rangle + \sum_{kl} \langle ik|v|jl\rangle \rho_{lk} \tag{3.31}$$

and the HF equations are obtained from Eq. (3.30):

$$[h, \rho] = 0. \tag{3.32}$$

$$h|\varphi_\nu\rangle = \varepsilon_\nu |\varphi_\nu\rangle . \tag{3.33}$$

The total energy of the system can be written as

$$E^{HF} = \sum_{i=1}^{A} t_{ii} + \frac{1}{2}\sum_{ij=1}^{A} \bar{v}_{ijij} = \sum_{i=1}^{A} \varepsilon_i - \frac{1}{2}\sum_{ij=1}^{A} \bar{v}_{ijij}. \tag{3.34}$$

Finally, the HF equations in coordinate space are given by

$$-\frac{\hbar^2}{2m}\nabla^2\varphi_i(\mathbf{r}) + v_H(\mathbf{r})\varphi_i(\mathbf{r}) - \int d^3\mathbf{r}' v_F(\mathbf{r}',\mathbf{r})\varphi_i(\mathbf{r}') = \varepsilon_i\varphi_i(\mathbf{r}). \tag{3.35}$$

Here, $v_H(\mathbf{r})$ and $v_F(\mathbf{r}',\mathbf{r})$ are defined as

$$v_H(\mathbf{r}) = \sum_{\varepsilon_j<\varepsilon_j} \int d^3\mathbf{r}' \varphi_j^\dagger(\mathbf{r}')v(\mathbf{r}',\mathbf{r})\varphi_j(\mathbf{r}') \tag{3.36}$$

$$v_F(\mathbf{r}',\mathbf{r}) = \sum_{\varepsilon_j<\varepsilon_j} \varphi_j^\dagger(\mathbf{r}')v(\mathbf{r}',\mathbf{r})\varphi_j(\mathbf{r}). \tag{3.37}$$

and they represent the Hartree (direct) and Fock (exchange) terms, respectively.

3.2.2 Skyrme-Hartree-Fock Equations

The Skyrme-Hartree-Fock equations can be obtained from the variation of the total energy with respect to the single particle wave functions φ_i:

$$\delta\left[E - \sum_i \varepsilon_i \int d^3r\, |\varphi_i(r)|^2\right] = 0 \tag{3.38}$$

using Skyrme energy density functionals

$$\delta E = \sum_q \int d^3r \left[\frac{\hbar^2}{2m_q^*(\mathbf{r})}\delta\tau_q(\mathbf{r}) + U_q\delta\rho_q(\mathbf{r}) + \mathbf{W}_q(\mathbf{r}).\delta\mathbf{J}_q(\mathbf{r})\right] \tag{3.39}$$

and the coefficients of the variations are defined as

$$\frac{\hbar^2}{2m_q^*} = \frac{\delta E}{\delta \tau_q} = \frac{\hbar^2}{2m_q} + \frac{1}{8}[t_1(2+x_1)+t_2(2+x_2)]\rho + \frac{1}{8}[t_2(2x_2+1)-t_1(2x_1+1)]\rho_q \quad (3.40)$$

where $m_q^*(\mathbf{r})$ is the effective mass and the central potential (U_q) is

$$\begin{aligned}
U_q = \frac{\delta E}{\delta \rho_q} &= \frac{1}{2}t_0[(2+x_0)\rho - (2x_0+1)\rho_q^2] \\
&+ \frac{1}{24}t_3\alpha\rho^{\alpha-1}[(2+x_3)\rho^2 - (2x_3+1)(\rho_p^2+\rho_n^2)] \\
&+ \frac{1}{12}t_3\rho^{\alpha}[(2+x_3)\rho - (2x_3+1)\rho_q] \\
&+ \frac{1}{8}[t_1(2+x_1)+t_2(2+x_2)]\tau \\
&+ \frac{1}{8}[t_2(2x_2+1)-t_1(2x_1+1)]\tau_q \\
&- \frac{1}{16}[3t_1(2+x_1)-t_2(2+x_2)]\nabla^2\rho + \frac{1}{16}[3t_1(2x_1+1)+t_2(2x_2+1)]\nabla^2\rho_q \\
&- \frac{1}{2}W_0[\nabla.\mathbf{J}+\nabla.\mathbf{J}_q] + \delta_{1q}V_c
\end{aligned} \quad (3.41)$$

whereas the spin-orbit potential is given as

$$W_q = \frac{\delta E}{\delta \mathbf{J}_q} = \frac{1}{2}W_0[\nabla\rho + \nabla\rho_q] - \frac{1}{8}(t_1x_1+t_2x_2)\mathbf{J} + \frac{1}{8}(t_1-t_2)\mathbf{J}_q. \quad (3.42)$$

The Skyrme-Hartree-Fock equations can be written in coordinate space as

$$\left[-\nabla.\frac{\hbar^2}{2m_q^*(\mathbf{r})}\nabla + U_q(\mathbf{r}) + \mathbf{W}_q(\mathbf{r}).(-i)(\nabla\times\sigma)\right]\varphi_i(r,\sigma,q) = \varepsilon_i\varphi_i(r,\sigma,q) \quad (3.43)$$

where $\varphi_i(r,\sigma,q)$ is a single-particle wave function and i, σ, and q are the orbital, spin and isospin quantum numbers, respectively.

3.2.3 Hartree Fock BCS Approximation

It has been known that the Skyrme-Hartree- Fock theory is rather successful in describing the static properties of closed shell nuclei. However, we need better approximations in order to calculate the properties of open shell nuclei. Besides the long-range particle-hole part of the interaction, we have to consider short-range particle-particle interaction part, namely, the pairing correlations in open shell nuclei. The development of the basic Hartree-Fock theory with the pairing correlations leads us to the Hartree-Fock- BCS or Hartree-Fock-Bogoulibov approximations. In the HF-BCS approximation, the mean field and pairing interaction are decoupled from each other. In the BCS theory, the wave function of even-even nuclei is written as

$$|BCS\rangle = \prod_{i>0}(u_i + v_i A_i^{\dagger})\,|0\rangle\,, \tag{3.44}$$

where, u_i and v_i are variational parameters and the operator $A_i^{\dagger} = a_i^{\dagger}\tilde{a}_i^{\dagger}$ creates a pair of like nucleons with opposite spin. The u_i^2 and v_i^2 represent the probability that a certain pair state $(i,\tilde{i})$ is unoccupied or occupied. The relation between them is given by

$$|u_i|^2 + |v_i|^2 = 1. \tag{3.45}$$

In the second quantization formalism, the Hamiltonian of a many-body system can be described in terms of the quasiparticle operators by the Bogoliubov transformation of Eq. (3.26) (see Appendix A). In the BCS theory, the ground state satisfies the property $a_i\,|BCS\rangle = 0$. In addition, The trial wave function parameters u and v are determined by the variation of the energy. The particle number (N) is not conserved, instead it is conserved on average

$$\langle BCS|\hat{N}|BCS\rangle = 2\sum_{i>0} v_i^2 = N \tag{3.46}$$

This can be achieved by adding a constraint to the Hamiltonian. Now, the variational Hamiltonian becomes

$$H' = H - \lambda\hat{N} \tag{3.47}$$

where λ is the Lagrange multiplier and defined as: $\lambda = dE/dN$. It is also called chemical potential or Fermi energy. If we apply the variational principle

$$\delta\langle BCS|H'|BCS\rangle = 0 \tag{3.48}$$

the solution yields

$$v_i^2 = \frac{1}{2}\left(1 - \frac{\varepsilon_i}{\sqrt{\varepsilon_i^2 + \Delta_i^2}}\right), u_i^2 = \frac{1}{2}\left(1 + \frac{\varepsilon_i}{\sqrt{\varepsilon_i^2 + \Delta_i^2}}\right) \tag{3.49}$$

and the gap equation is obtained as

$$\Delta_i = -\frac{1}{2}\sum_{i'>0} \bar{v}_{i\bar{i}i'\bar{i}'} \frac{\Delta_{i'}}{\sqrt{\varepsilon_{i'}^2 + \Delta_{i'}^2}}. \tag{3.50}$$

The particle number equation is defined as:

$$N = \sum_i (2j_i + 1) v_i^2. \tag{3.51}$$

Here, j_i represents the total angular momentum quantum number of the single- particle state. In the BCS theory, the total density is defined as:

$$\rho(r) = \frac{1}{4\pi}\sum_i (2j_i + 1) v_i^* v_i |\phi_i(r)|^2, \tag{3.52}$$

and the abnormal density (or pairing tensor) is:

$$\kappa(r) = -\frac{1}{4\pi}\sum_i (2j_i + 1) u_i v_i |\phi_i(r)|^2, \tag{3.53}$$

In the case of closed shell nuclei, the pairing interaction vanishes and the HF+BCS equations reduce to the well-known HF equations.

3.2.4 Hartree Fock Bogoulibov Approximation

Despite the success of the HF+BCS method in the calculation of the ground state properties of open shell nuclei near the stability valley, one needs better approximations for the nuclei far from the stability line. For the nuclei near the drip line, the Fermi level is close to the particle continuum and the coupling between the continuum states and bound states has to be taken into account properly. Since BCS approximation not suitable to describe the scattering of nucleon pairs from bound states to the continuum, it creates the unphysical neutron gas problem [10]. The Hartree-Fock-Bogoulibov (HFB) method is one of the appropriate approximations in order to investigate the properties of the medium and heavy nuclei through the whole nuclear landscape. The HFB differs from the HF+BCS approximation in the treatment of the pairing correlations. In this approximation, the mean field and pairing field affect each other. In this thesis, we also compare the results of HF+BCS and HFB in order to check the validity of the results when it is needed. The quasiparticle vacuum condition is given by $\hat{\beta}\,|\Phi\rangle = 0$. The quasiparticle operators are connected to the particle operators via:

$$\hat{\beta}_i^\dagger = \sum_j \left(U_{ji}\hat{c}_j^\dagger + V_{ji}\hat{c}_j \right), \tag{3.54}$$

$$\hat{\beta}_i = \sum_j \left(U_{ji}^*\hat{c}_j + V_{ji}^*\hat{c}_j^\dagger \right). \tag{3.55}$$

Here, j runs over the whole configuration space. The quasiparticle operators can be written in a more compact way as:

$$\begin{pmatrix} \hat{\beta} \\ \hat{\beta}_i^\dagger \end{pmatrix} = \begin{pmatrix} U & V^* \\ V & U^* \end{pmatrix} \begin{pmatrix} \hat{c} \\ \hat{c}_j^\dagger \end{pmatrix} \tag{3.56}$$

The single-particle density matrix and pairing density matrices are defined as:

$$\rho_{ij} = \left\langle HFB \middle| c_j^\dagger c_i \middle| HFB \right\rangle = V^* V^T = \rho_{ji}^* \tag{3.57}$$

$$\kappa_{ij} = \left\langle HFB \middle| c_j c_i \middle| HFB \right\rangle = V^* U^T = -\kappa_{ji} \tag{3.58}$$

which are similar to the HF+BCS case. The generalized density matrix R is written as:

$$R = \begin{pmatrix} \rho & \kappa \\ -\kappa^* & 1-\rho^* \end{pmatrix} \tag{3.59}$$

where the generalized density matrix satisfies the $R^2 = R$ equality. As in the case of HF and HF+BCS approximations, the minimization of the total energy of the system gives the so-called HFB equations:

$$E = \left\langle \Psi \middle| \hat{H} \middle| \Psi \right\rangle = E\left[\rho, \kappa, \kappa^*\right], \tag{3.60}$$

$$\begin{pmatrix} h-\lambda & \Delta \\ -\Delta^* & -(h-\lambda)^* \end{pmatrix} \begin{pmatrix} U^k \\ V^k \end{pmatrix} = E_k \begin{pmatrix} U^k \\ V^k \end{pmatrix}. \tag{3.61}$$

Here, E_k stands for the quasiparticle energy and λ is the Lagrange multiplier or chemical potential. Also, the expectation value of the Hamiltonian h_{ij} and pairing field Δ_{ij} are defined as:

$$h_{ij} = \frac{\delta E(\rho, \kappa, \kappa*)}{\delta \rho_{ji}} = h^*_{ji} \tag{3.62}$$

$$\Delta_{ij} = \frac{\delta E(\rho, \kappa, \kappa*)}{\delta \kappa^*_{ij}} = -\Delta_{ji}, \tag{3.63}$$

respectively.

3.3 Time Dependent Mean Field

3.3.1 The Random Phase Approximation (RPA)

In order to calculate the excited states of nuclei, one needs to go beyond the standard Hartree-Fock approximation. One of the appropriate approximations in the calculation of the excited states of closed shell nuclei is the Random Phase Approximation (RPA). The RPA theory was developed by Bohm and Pines [102] in order to study the plasma oscillations of the electron gas in the early 1950's. Later, it has been used in the the calculation of the nuclear excited states of closed shell nuclei. The RPA equations can be derived in several ways [11, 12].

In this section, we derive the Random Phase Approximation (RPA) equations using the Equations of Motion method (EOM). In case of no external force, the Hamiltonian of the system is

$$H = \sum_c \varepsilon_c c^\dagger_a c_a - \frac{1}{2}\sum_{ab} \overline{v}_{abab} + \frac{1}{4}\sum_{abcd} : c^\dagger_a c^\dagger_b c_d c_c : . \tag{3.64}$$

The Schrödinger equation is written as

$$H\left|\nu\right\rangle = E_\nu \left|\nu\right\rangle . \tag{3.65}$$

The creation and annihilation operators can be defined as

$$|\nu\rangle = \Gamma_\nu^\dagger |0\rangle, \tag{3.66}$$

$$\Gamma_\nu |0\rangle = 0. \tag{3.67}$$

By using the Schrödinger equation 3.65, we obtain the Equation of Motion

$$\left[H, \Gamma_\nu^\dagger\right] |0\rangle = (E_\nu - E_0)\Gamma_\nu^\dagger |0\rangle. \tag{3.68}$$

Multiplying from the left part of the equations with an arbitrary state of the form $\langle 0| \delta\Gamma$ will give

$$\langle 0| \left[\delta\Gamma, \left[H, \Gamma_\nu^\dagger\right]\right] |0\rangle = (E_\nu - E_0) \langle 0| \left[\delta\Gamma, \Gamma_\nu^\dagger\right] |0\rangle \tag{3.69}$$

Since the true ground state is not simply the p-h vacuum in RPA, we can create a $p-h$ pair and destroy one at the same time . Thus, the creation operator can be written in a straightforward way:

$$\Gamma_\nu^\dagger = \sum_{ab} X_{ab}^\nu c_a^\dagger c_b - Y_{ab}^\nu c_b^\dagger c_a \tag{3.70}$$

and the RPA ground state is assumed to be

$$\Gamma_\nu |RPA\rangle = 0. \tag{3.71}$$

Since we have two kinds of variations $\delta\Gamma|0\rangle$, we also have two sets of equations of motion

$$\langle RPA| \left[c_b^\dagger c_a, \left[H, \Gamma_\nu^\dagger\right]\right] |RPA\rangle = \hbar\omega_\nu \langle RPA| \left[c_b^\dagger c_a, \Gamma_\nu^\dagger\right] |RPA\rangle, \tag{3.72}$$

$$\langle RPA| \left[c_a^\dagger c_b, \left[H, \Gamma_\nu^\dagger\right]\right] |RPA\rangle = \hbar\omega_\nu \langle RPA| \left[c_a^\dagger c_b, \Gamma_\nu^\dagger\right] |RPA\rangle. \tag{3.73}$$

Here, $\hbar\omega_\nu$ is the excitation energy ($\hbar\omega_\nu = E_\nu - E_0$) of the state $|\nu\rangle$. These equations contain only expectation values of the four Fermion operators. If we assume that the correlated ground state does not differ very much from the HF ground state, we can calculate all the expectation values in the HF approximation. This approximation is known as Quasi-Boson Approximation. In this approximation, we assume that

$$\langle RPA| \left[c_b^\dagger c_a, c_c^\dagger c_d\right] |RPA\rangle \cong \langle HF| \left[c_b^\dagger c_a, c_c^\dagger c_d\right] |HF\rangle = \delta_{ac}\delta_{bd}. \tag{3.74}$$

Within the quasi-boson approximation (QBA), the amplitudes X_{ab}^ν and Y_{ab}^ν have a very direct meaning: their absolute square give the probability of finding the states $c_a^\dagger c_b|0\rangle$ and $c_b^\dagger c_a|0\rangle$ in the excited state $|\nu\rangle$, namely, the p-h and h-p matrix elements of the transition density are

$$\rho_{ab}^\nu = \langle 0| c_b^\dagger c_a |\nu\rangle \simeq \langle HF| c_b^\dagger c_a, \Gamma_\nu^\dagger |HF\rangle = X_{ab}^\nu, \tag{3.75}$$

$$\rho_{ba}^\nu = \langle 0| c_a^\dagger c_b |\nu\rangle \simeq \langle HF| c_a^\dagger c_b, \Gamma_\nu^\dagger |HF\rangle = Y_{ab}^\nu. \tag{3.76}$$

In these equations, X and Y are called the forward and backward amplitudes. If we write Eqs. (3.72), (3.73) in a compact form, we obtain the RPA matrix

$$\begin{pmatrix} A & B \\ B^* & A^* \end{pmatrix} \begin{pmatrix} X^\nu \\ Y^\nu \end{pmatrix} = (E_m - E_0) \begin{pmatrix} 1 & 0 \\ 0 & -1 \end{pmatrix} \begin{pmatrix} X^\nu \\ Y^\nu \end{pmatrix}, \tag{3.77}$$

defining the RPA matrices A and B

$$A_{abcd} \equiv \langle HF| \left[c_b^\dagger c_a, \left[H, c_c^\dagger c_d\right]\right] |HF\rangle = (\varepsilon_a - \varepsilon_b)\delta_{ac}\delta_{bd} + \left\langle ab^{-1}; J |V_{res}| cd^{-1}; J\right\rangle \tag{3.78}$$

$$B_{abcd} \equiv -\langle HF| \left[c_b^\dagger c_a, \left[H, c_d^\dagger c_c\right]\right] |HF\rangle = \left\langle ab^{-1}; J |V_{res}| dc^{-1}; J\right\rangle \tag{3.79}$$

where the A matrix is Hermitian and the B matrix is symmetric. The coupled p-h matrix elements of the interaction are written as

$$\begin{aligned}\left\langle ab^{-1}; J |V_{res}| cd^{-1}; J\right\rangle = &\sum_{JM} (-)^{j_d - m_d + j_b - m_b} (j_a m_a j_b - m_b|JM)(j_c m_c j_d - m_d|JM) \\ &\times \langle j_a m_a j_d m_d |V_{res}| j_b m_b j_c m_c\rangle .\end{aligned} \tag{3.80}$$

In the Skyrme RPA, the residual interaction is given by the second derivative of the energy density functional with respect to the density and defined as $V_{res}^{qq'} = \delta^2 E/\delta\rho_q \delta\rho_{q'}$. The solutions of the RPA equations come in pairs, that is, we obtain both positive and negative energy states with their eigenvectors. However, only positive energy solutions are physically meaningful. Eqn. (3.70) can be written in angular momentum coupled scheme as

$$\Gamma_\nu^\dagger = \sum_{ab} X_{ab}^{\nu J} A_{ab}^\dagger(JM) - Y_{ab}^{\nu J} A_{ab}(\widetilde{JM}). \tag{3.81}$$

Here, $A_{ab}^\dagger$ and $A_{ab}(\widetilde{JM})$ are the coupled p-h creation and destruction operators which are defined as

$$A_{ab}^\dagger(JM) = \sum_{m_a m_b} (-)^{j_b - m_b} \langle j_a m_a j_b - m_b | JM \rangle \, c_{j_a m_a}^\dagger c_{j_b m_b}, \tag{3.82}$$

$$A_{ab}(\widetilde{JM}) = \sum_{m_a m_b} (-)^{J+M+j_b-m_b} \langle j_a m_a j_b - m_b | JM \rangle \, c_{j_b m_b}^\dagger c_{j_a m_a}. \tag{3.83}$$

Normalization condition for the RPA equations is

$$\langle \nu | \nu \rangle = \sum_{ab} (|X_{ab}^\nu|^2 - |Y_{ab}^\nu|^2) = 1. \tag{3.84}$$

3.3.2 The Quasiparticle Random Phase Approximation (QRPA)

In the previous part, we have introduced the RPA and its derivation. The RPA is one of the appropriate methods in the calculation of the excitations of closed- shell even-even nuclei. However, it is not suitable for open shell nuclei. If we go beyond the closed-shell nuclei, we should use the Quasiparticle Random Phase Approximation (QRPA) where the pairing correlations are taken into account. The QRPA equations can be derived by means of the Equation-of-motion (EOM) method as in the the RPA. In this approximation, the BCS vacuum is used as operative vacuum during the derivation. However, this vacuum is not the exact vacuum of QRPA operators. Therefore, the QRPA equations are approximate and do not satisfy the variational principle like in RPA theory.

3.3.3 Derivation of the QRPA Equations

The starting point in the EOM method is the definition of a suitable excitation operator. In QRPA, the excitation operator is defined with quasiparticle creation and annihilation operators. The QRPA excitation operator is defined as:

$$\Gamma_\nu^\dagger = \sum_{a\geq b}\left[X_{ab}^{\nu}A_{ab}^\dagger(JM) - Y_{ab}^{\nu}\widetilde{A}_{ab}(JM)\right] \tag{3.85}$$

and its Hermitian conjugate is

$$\Gamma_\nu = \sum_{a\geq b}\left[X_{ab}^{\nu *}A_{ab}(JM) - Y_{ab}^{\nu *}\widetilde{A}_{ab}^\dagger(JM)\right]. \tag{3.86}$$

The two quasiparticle operators are given by

$$A_{ab}^\dagger(JM) = N_{ab}(J)\left[a_a^\dagger a_b^\dagger\right]_{JM}, \tag{3.87}$$

$$\widetilde{A}_{ab}(JM) = (-1)^{J+M}A_{ab}(J-M) = -N_{ab}(J)\left[\widetilde{a}_a\widetilde{a}_b\right]_{JM}. \tag{3.88}$$

We define the coupled operators as:

$$A_{ab}^\dagger(JM) = N_{ab}\sum_{m_am_b}\langle j_am_aj_bm_b|JM\rangle a_a^\dagger a_b^\dagger \tag{3.89}$$

$$A_{ab}(\widetilde{JM}) = N_{ab}(-)^{J+M}\sum_{m_am_b}\langle j_am_aj_bm_b|J-M\rangle a_ba_a \tag{3.90}$$

The simple BCS vacuum is not the vacuum of QRPA, i.e., $\Gamma_\nu|BCS\rangle \neq 0$. Many quasiparticle components are expected to appear in the QRPA vacuum. Because of this fact, the vacuum is called correlated vacuum. If we take the $|BCS\rangle$ as the approximate vacuum, the equation of motion can be written as

$$\langle BCS|\left[\delta\Gamma, H, \Gamma_\nu^\dagger\right]|BCS\rangle = E_\nu\langle BCS|\left[\delta\Gamma, \Gamma_\nu^\dagger\right]|BCS\rangle \tag{3.91}$$

where $\delta\Gamma = A_{ab}(JM)$ and $\delta\Gamma = \widetilde{A}_{ab}^\dagger(JM)$ are the basic variations of the first and second term and H is the complete Hamiltonian in terms of quasiparticle operators. In order to evaluate the right hand side of Eq. (3.91), BCS expectation values of the commutators of the quasiparticle pair operators A and $A^\dagger$ are needed:

$$\langle BCS|\left[A_{ab}(JM), A_{cd}^\dagger(J'M')\right]|BCS\rangle = \delta_{ac}\delta_{bd}\delta_{JJ'}\delta_{MM'} \tag{3.92}$$

$$\langle BCS|\left[\tilde{A}_{ab}(JM), \widetilde{A}_{cd}^\dagger(J'M')\right]|BCS\rangle = \delta_{ac}\delta_{bd}\delta_{JJ'}\delta_{MM'}. \tag{3.93}$$

Here, we have assumed that $a \geq b$ and $c \geq d$. If one follows the RPA equations derivation, we can define the A and B matrices as

$$A_{ab,cd}(J) = \langle BCS| \left[A_{ab}(JM), H, A^{\dagger}_{cd}(J'M')\right] |BCS\rangle, \tag{3.94}$$

$$B_{ab,cd}(J) = -\langle BCS| \left[A_{ab}(JM), H, \widetilde{A}^{\dagger}_{cd}(J'M')\right] |BCS\rangle. \tag{3.95}$$

Then, we obtain

$$\sum_{c\geq d} A_{ab,cd} X^{\nu}_{cd} + \sum_{c\geq d} B_{ab,cd} Y^{\nu}_{cd} = E_{\nu} X^{\nu}_{ab}, \tag{3.96}$$

$$-\sum_{c\geq d} B^{\dagger}_{ab,cd} X^{\nu}_{cd} + \sum_{c\geq d} A^{T}_{ab,cd} Y^{\nu}_{cd} = E_{\nu} Y^{\nu}_{ab}. \tag{3.97}$$

The QRPA equations can be combined into a matrix:

$$\begin{pmatrix} A & B \\ -B^{*} & -A^{*} \end{pmatrix} \begin{pmatrix} X^{\nu} \\ Y^{\nu} \end{pmatrix} = E_{\nu} \begin{pmatrix} X^{\nu} \\ Y^{\nu} \end{pmatrix}. \tag{3.98}$$

The A and B matrices are defined as

$$\begin{aligned} A_{abcd} =& (E_a + E_b)\delta_{ac}\delta_{bd} + (u_a u_b u_c u_d + v_a v_b v_c v_d) \langle ab; J|V|cd; J\rangle \\ & + N_{ab}(J) N_{cd}(J) \big[(u_a v_b u_c v_d + v_a u_b v_c u_d) \left\langle ab^{-1}; J|V_{res}|cd^{-1}; J\right\rangle \\ & - (-)^{j_c+j_d+J} (u_a v_b v_c u_d + v_a u_b u_c v_d) \left\langle ab^{-1}; J|V_{res}|dc^{-1}; J\right\rangle \big] \end{aligned} \tag{3.99}$$

$$\begin{aligned} B_{abcd} =& -(u_a u_b v_c v_d + v_a v_b u_c u_d) \langle ab; J|V|cd; J\rangle \\ & + N_{ab}(J) N_{cd}(J) \big[(u_a v_b v_c u_d + v_a u_b u_c v_d) \left\langle ab^{-1}; J|V_{res}|cd^{-1}; J\right\rangle \\ & - (-)^{j_c+j_d+J} (u_a v_b u_c v_d + v_a u_b v_c u_d) \left\langle ab^{-1}; J|V_{res}|dc^{-1}; J\right\rangle \big] \end{aligned} \tag{3.100}$$

Here, E is a quasiparticle energy, u and v are BCS occupation factors of the single-particle states and $N_{ab,cd}(J)$ is the normalization factor. The p-h and p-p matrix elements of the interaction is defined in angular momentum coupled form as

$$\left\langle ab^{-1};J\left|V_{res}\right|cd^{-1};J\right\rangle = \sum_{JM}(-)^{j_d-m_d+j_b-m_b}\left(j_a m_a j_b - m_b|JM\right)\left(j_c m_c j_d - m_d|JM\right) \times \left\langle j_a m_a j_d m_d\left|V_{res}\right| j_b m_b j_c m_c\right\rangle, \tag{3.101}$$

$$\left\langle ab;J\left|V\right|cd;J\right\rangle = \sum_{JM}\left(j_a m_a j_b m_b|JM\right)\left(j_c m_c j_d m_d|JM\right) \times \left\langle j_a m_a j_b m_b\left|V\right| j_c m_c j_d m_d\right\rangle. \tag{3.102}$$

where the p-h and p-p interactions are obtained from

$$V^{ph}_{adbc} = \frac{\delta^2 E(\rho,\kappa,\kappa*)}{\delta\rho_{ba}\rho_{dc}}, \tag{3.103}$$

$$V^{pp}_{abcd} = \frac{\delta^2 E(\rho,\kappa,\kappa*)}{\delta\kappa*_{ba}\,\kappa_{dc}}. \tag{3.104}$$

The QRPA equations are similar to the RPA equations and the interaction matrices are independent of M. After the diagonalization of the QRPA matrix, we obtain eigenvalues and eigenvectors which correspond to the excitation energies and their wave functions.

3.3.4 Collectivity of the Excited States

Since we deal with the collectivity of the low-energy modes, we introduce the definition of collectivity in this section. The analysis of the response in terms of collectivity may also be useful. We define here the collectivity as the number of particle-hole (ph) pairs significantly contributing to a given excited state $|\nu\rangle$. This contribution for the ph pair is evaluated as

$$P^{\nu}_{ph} = \frac{|X^{\nu}_{ph}|^2 - |Y^{\nu}_{ph}|^2}{\sum_{ph}|X^{\nu}_{ph}|^2 - |Y^{\nu}_{ph}|^2} \tag{3.105}$$

In this thesis, we consider that a ph pair contributes in a non-negligible way to the excited state $|m\rangle$ if $P^{\nu}_{ph} \geq 5$ %. The collectivity C^{ν} of the excited state $|\nu\rangle$ is the number of such ph pairs. It should be noted that ph pairs can interfere constructively or destructively between each other. Therefore an excited state can be collective with a small strength, if destructive interferences are at work, although many ph pairs are involved.

3.3.5 Transition Operators and Transition Densities

In this section, we give a brief overview of the operators of the nuclear excitations and transition densities. Vibrational states can be obtained either by hadronic or electromagnetic excitations in which proton and neutron numbers do not change with the effect of the external field. The one-body operator $F(r)$ of the selected excitation can then induce p-h excitations. Generally, an isoscalar or isovector external field of the nuclear multipole transition operator F can be written as

$$\hat{F}^{IS}_{JM} = \sum_{i=1}^{A} r_i^J Y_{JM}(\hat{r}_i), \tag{3.106}$$

$$\hat{F}^{IV}_{JM} = \sum_{i=1}^{A} r_i^J Y_{JM}(\hat{r}_i)\tau_z(i) \tag{3.107}$$

where the sums run over all nucleons and $\tau_z(i)$ is the z-component of the isospin operator of nucleon i. In the monopole case (L=0), the operator reads

$$\hat{F}^{IS}_{00} = \sum_{i=1}^{A} r_i^2 Y_{00}(\hat{r}_i) \tag{3.108}$$

In addition, for the dipole case (L=1), the isoscalar dipole operator reads

$$\hat{F}^{IS}_{1M} = \sum_{i=1}^{A} r_i^3 Y_{1M}(\hat{r}_i) \tag{3.109}$$

It should be noted that the operator

$$\hat{F}^{IS}_{1M} = \sum_{i=1}^{A} r_i Y_{1M}(\hat{r}_i) \tag{3.110}$$

corresponds to a translational mode,i.e., not an intrinsic excitation of the nucleus. In the isoscalar dipole mode, it is also necessary to remove the spurious states. The spurious states give unphysical contributions to the states due to the center-of-mass motion and they should be removed from real states. The spurious states can occur due to the several reasons: either fully self-consistency is not achieved or numerical inaccuracies in the calculations can cause the formation of spurious states. For the isoscalar dipole mode, the spurious states can be removed with the modification of the operator as

$$\hat{F}^{IS}_{1M} = \sum_{i=1}^{A} (r_i^3 - \eta r_i) Y_{1M}(\hat{r}_i) \tag{3.111}$$

in here, $\eta = 5/3 \langle r^2 \rangle$ [103]. It is also necessary to remove spurious states from isovector dipole states

$$\hat{F}^{IV}_{1M} = \frac{eN}{A} \sum_{i=1}^{Z} r_i Y_{1M} - \frac{eZ}{A} \sum_{i=1}^{N} r_i Y_{1M} \tag{3.112}$$

where the effective charge for protons and neutrons are $\frac{eN}{A}$ and $\frac{eZ}{A}$, respectively. The reduced transition probability for any operator is defined as

$$B(EJ, i \to f) = \frac{1}{2J_i + 1} \left| \langle f \| F_J \| i \rangle \right|^2 . \tag{3.113}$$

and the transition strength is calculated with

$$B(EJ, i \to f) = \left| \sum_{ph} (X^{\nu}_{ph} + Y^{\nu}_{ph}) \times \langle p || Y_J || h \rangle \right|^2 \tag{3.114}$$

at the RPA level. In this thesis, we mainly deal with the transition densities of the low-energy excitations. Important information on the dynamics of a nuclear collective mode can be obtained from the transition density analysis of a given state of excitation. Using RPA forward and backward amplitudes, the transition density is given as

$$\delta\rho_\nu(r) = \frac{1}{\sqrt{2J+1}} \sum_{ph} (X^{\nu}_{ph} + Y^{\nu}_{ph}) \times \langle p || Y_J || h \rangle \frac{R_p(r) R_h(r)}{r^2} \tag{3.115}$$

in here, $R(r)$ is the reduced radial wave function. In QRPA, the transition density reads

$$\delta\rho_\nu(r) = \frac{1}{\sqrt{2J+1}} \sum_{ph} \left[\left(X^{\nu}_{ph} + Y^{\nu}_{ph} \right) (u_p v_h + v_p u_h) \right] \times \langle p || Y_J || h \rangle \frac{R_p(r) R_h(r)}{r^2} \tag{3.116}$$

where u and v are the BCS amplitudes of the single-particle states. In order to calculate isoscalar (IS) or isovector (IV) transition densities, one can just perform

$$\delta\rho^{(IS)}_\nu(r) = \delta\rho^n_\nu(r) + \delta\rho^p_\nu(r), \tag{3.117}$$

$$\delta\rho^{(IV)}_\nu(r) = \delta\rho^n_\nu(r) - \delta\rho^p_\nu(r). \tag{3.118}$$

3.3.6 Sum Rules

Sum rules are important tools in order to test the reliability of the used approximations and calculations. For a given one-body operator, the strength function is given as [9, 11]

$$S(E) = \sum_{\nu} |\langle \nu || F_{\nu} || 0 \rangle|^2 \, \delta(E - E_{\nu}). \tag{3.119}$$

The k^{th} moment is given by

$$m_k = \sum_{\nu} (E_{\nu} - E_0)^k \, |\langle \nu | F_{\nu} | 0 \rangle|^2 . \tag{3.120}$$

In the case of k=1 (k=0) ,we obtain the linear moment S_1 (S_0) which is also known as the linear energy weighted sum rule (The non-energy energy weighted sum rule). The energy-weighted sum rule (EWSR) is a fundamental quantity because it can be evaluated without requiring a detailed RPA calculation, if the mean field and RPA calculations correspond to the same starting Hamiltonian H.

$$m_1 = \sum_{\nu} (E_{\nu} - E_0) \, |\langle \nu | F_{\nu} | 0 \rangle|^2 = \frac{1}{2} \langle 0 | [F, [H, F]] | 0 \rangle . \tag{3.121}$$

This is known as the Thouless Theorem. For the isoscalar operators (spin independent operators) with multipole L, the EWSR is given by

$$m_1 = \frac{\hbar^2}{2m} L(L+2)^2 \frac{A}{4\pi} \langle r^{2L-2} \rangle. \tag{3.122}$$

Here, $\langle r^{2L-2} \rangle$ is the ground-state expectation value and experimentally accessible. In the monopole case, the double commutator sum rule is given by

$$m_1 = \frac{\hbar^2}{m} \frac{A}{2\pi} \langle r^2 \rangle \tag{3.123}$$

and for the isoscalar dipole operator

$$m_1 = \frac{\hbar^2}{m} \frac{A}{2\pi} (33 \langle r^4 \rangle - 25 \langle r^2 \rangle^2) \tag{3.124}$$

However, the isovector dipole operator depends on the isospin and the EWSR reads

$$\frac{1}{2} \langle 0 | [F, [H, F]] | 0 \rangle = \frac{1}{2} \langle 0 | [F, [H, F]] | 0 \rangle \, (1 + \kappa) \tag{3.125}$$

where κ is the enhancement factor and $\kappa \approx 0.2 - 0.3$. Finally, for the dipole excitations the sum rule gives

$$m_1 = \frac{9}{\pi}\frac{\hbar^2}{m}\frac{NZ}{A}\left(1 + \frac{2m}{\hbar^2}\frac{4\pi A}{NZ}\left(t_1\left(1 + \frac{x_1}{2}\right) + t_2\left(1 + \frac{x_2}{2}\right)\right)\int drr^2\rho_p\rho_n\right) \tag{3.126}$$

with the Skyrme interaction.

The non-energy weighted sum rule (m_0) and energy weighted sum rule (m_1) are used in the determination of the centroid energy, $E_0 = \frac{m_1}{m_0}$. In addition, the constrained (E_{-1}) and scaled (E_3) energies are defined as

$$E_{-1} = \sqrt{\frac{m_1}{m_{-1}}}, E_3 = \sqrt{\frac{m_3}{m_1}}. \tag{3.127}$$

which give information about the distribution of the strength function.

CHAPTER 4

ANALYSIS OF PYGMY DIPOLE MODE IN DOUBLE MAGIC NUCLEI

In this section, we present the numerical results for the dipole excitations of nuclei. Since we focus on nuclei around magicity in the nuclear chart, we performed calculations with self-consistent Hartree Fock+Random Phase Approximation in matrix formalism. In view of the variety of interpretations of the PDR, it may be useful to provide a systematic analysis of this mode on the nuclear chart. For now, calculations of the dipole strength with HF+RPA method have been done in Refs. [13–20] with various Skyrme interactions. However, a systematic work focused on transition density properties of low-lying modes on various nuclei of nuclear chart is still lacking. This would allow to investigate in a general way the neutron and proton contributions to the PDR pattern along the nuclear chart and provide useful information through the use of transition densities, as demonstrated in the case of the ^{140}Ce PDR. The collectivity of the PDR is also currently under discussion [9]. On this purpose a systematic analysis of the collectivity of the response should also be undertaken. This chapter is based on the publication 'Analysis of the proton and neutron contributions to the dipole mode in doubly magic nuclei' [104].

4.1 Details of the Calculations for the Dipole Spectrum

In this part, we mainly investigate the Pygmy Dipole Resonance (PDR) in doubly magic nuclei in which pairing effects are expected to be weak such as in the N=40 subshell closure. More advanced models could be used such as the continuum-QRPA [105] but we would like to focus here on spherical non-superfluid systems, to be able to provide a clear interpretation of the PDR, possibly in terms of single particle levels. The continuum effect can play a role on the low energy dipole response, but shall not qualitatively change the results. The Skyrme type SLy4 interaction parameters are used both in HF and RPA calculations. The SGII interaction is also used in order to study the impact of functional's choice on the results. First, we performed the spherical Hartree-Fock calculation with Skyrme interaction and the results were used to perform self-consistent RPA calculations of the isovector dipole response.

The HF-RPA model with Skyrme effective forces is well-known [9]. We only mention that in this work we solve the RPA equations in configuration space, choosing the particle-hole space so as to exhaust the energy-weighted sum rules. The continuous part of the single-particle spectrum is discretized by diagonalizing the HF Hamiltonian on a harmonic oscillator basis with 12 shells. In the present study, the isovector dipole response of magic nuclei is described with the microscopic HF+RPA method. All the terms of the residual interaction are calculated self-consistently, except for the the spin-orbit and the Coulomb terms. In this case the mixing of the spurious term in the soft dipole strength is known to be small, mainly a shift of few hundreds keV for some states [106]. The present calculations are performed in a box of radius R=20 fm. The continuum treatment can also play a role on the strength: in the case of neutron-rich nuclei, the pygmy mode can be located above the one neutron separation energy (Table 4.1). This shall be the case of the other neutron-rich nuclei of this study such as ^{24}O, ^{70}Ca or ^{132}Sn. However, from previous continuum QRPA studies, the discretization of the continuum is expected to shift the states of the PDR not more than by 500 keV [105, 107].

The Skyrme type SLy4 [108] interaction is used both in HF and RPA to accomplish the self-consistency. Calculations are also performed with SGII [103], yielding similar results than in the SLy4 case. A 600 keV smearing factor is used on the RPA response for presentation purposes.

The collectivity of the states are also investigated (see Eq. (3.105)). In order to provide an overview of the PDR feature on the nuclear chart, the transition densities of the PDR in O, Ca, Ni Sn, and Pb nuclei are studied. The common trends which can be extracted from these analysis will be given in the conclusion.

Table 4.1 One neutron separation energies for doubly magic nuclei

Nucleus	S_n (MeV)
^{16}O	13.4
^{24}O	4.1
^{40}Ca	14.8
^{48}Ca	9.6
^{70}Ca	1.2
^{56}Ni	16.3
^{68}Ni	8.9
^{78}Ni	5.9
^{100}Sn	17.1
^{132}Sn	7.9
^{208}Pb	7.9

4.1.1 Oxygen Isotopes

Both theoretical and experimental analysis of oxygen isotopes show that the stable ^{16}O nucleus has no low-lying modes whereas neutron-rich isotopes of oxygen exhibit a low-energy dipole mode below the Giant Dipole Resonance region [19, 35, 109]. In recent theoretical studies with the RRPA method and large scale shell model calculations, fragmented isovector dipole strength was centered at 21.8 MeV and 23.7 MeV for ^{16}O nucleus, respectively [35, 110].

The isovector dipole response and transition densities of the ^{16}O nucleus obtained with the HF+RPA calculation is displayed in Figure 4.1 Giant Dipole Resonance exhibits strong peaks at 18.1 MeV and 19.4 MeV and exhausts 25.9% and 30.5% of the Energy Weighted Sum Rule (EWSR),respectively. The centroid value of the energy is found at 21.4 MeV. Experimentally, the mean energy of the GDR is found as 23.2 MeV [111]. As expected, there is no strong low-lying mode because of the equal contribution of protons and neutrons and the collectivity C is the largest for the GDR. At large energies, above 25 MeV, the response is as collective as the one in the 20-25 MeV range. However, the smaller strength at large energies shows that the ph pairs interfere destructively. The transition density analysis shows that protons and neutrons are oscillating out of phase for GDR at 19.4 MeV which is an usual feature of GDRs.

HF+RPA results for the isovector dipole response of neutron-rich oxygen ^{24}O nucleus

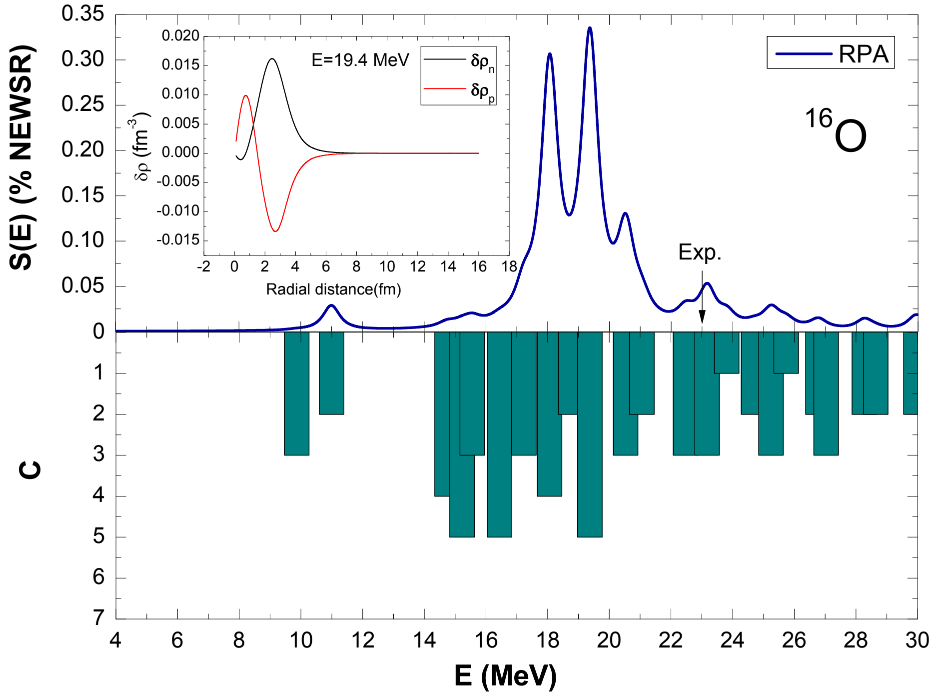

Figure 4.1 Upper panel: Calculations within RPA for the dipole strength distribution in ^{16}O with the Skyrme type SLy4 interaction. In the upper left insertion the proton and neutron transition densities are plotted for the GDR peak at 19.4 MeV excitation energy. The experimental GDR value is taken from Ref. [111] Lower panel: Collectivity C versus energy graph where C is defined using Eq. (3.105). The strength are given in Non Energy Weighted Sum Rule (NEWSR) units.

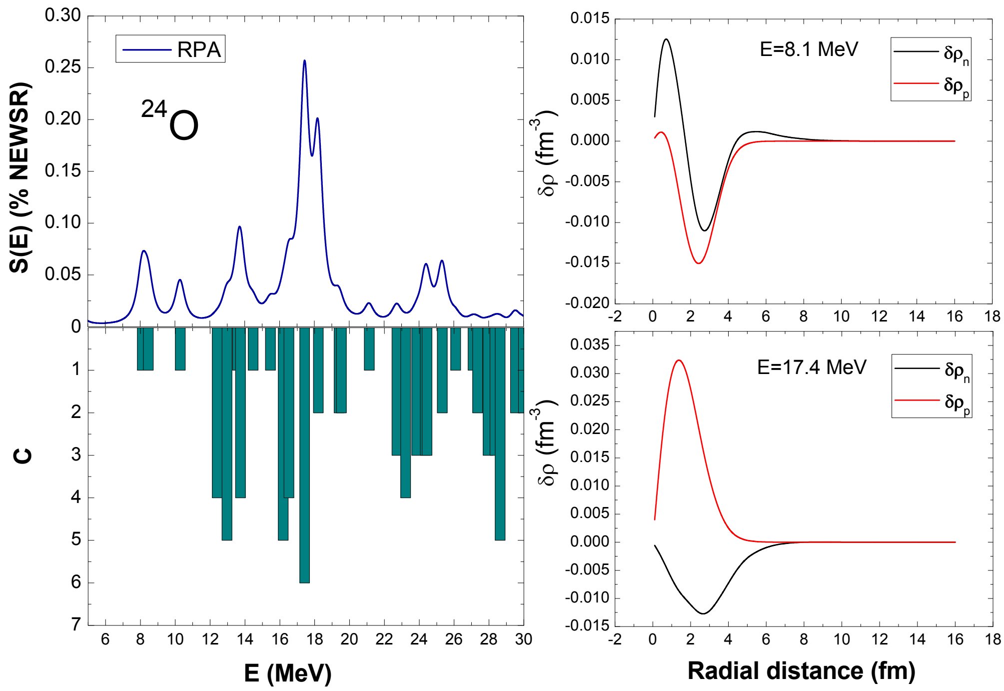

Figure 4.2 Left Panel: same as in Figure 4.1 but for the ^{24}O nucleus. Right Panel: transition densities for GDR and PDR regions.

are displayed in Figure 4.2. Detailed works with RQRPA and QRPA methods together with experiments in neutron-rich oxygen isotopes show that the low-lying strength (PDR) results from single neutron particle-hole excitations. With the increase of neutron number, the dipole strength appears to be more fragmented [32,35,84] than in the ^{16}O case. In our calculations, the GDR region is also much more fragmented as expected from the increase of the neutron Fermi level. In addition, a low-lying strength appears below the GDR region, at about 8 MeV with 2.37% of EWSR. Figure 4.2. shows that these excitations are non-collective as noticed in previous studies [9]. Transition densities of ^{24}O nucleus for GDR and PDR regions are given in the right part of Figure 4.2. In several theoretical analysis, it has been shown that the GDR displays usual IV character whereas PDR motion is IS in the nuclear interior with neutron dominated motion on the surface [9]. The present results yield a different interpretation: while GDR motion is IV as usual, PDR displays a mixed IS+IV character inside the nucleus and shows neutron character outside the nucleus where neutron skin oscillating around the core with no contribution from protons. The transition density results are rather different especially in the interior region of the nucleus, compared to other theoretical works in oxygen isotopes.

4.1.2 Calcium Isotopes

Recently, high resolution photon scattering experiments were performed to study calcium isotopes [112]. The GDR peak was measured at about 19 MeV for both ^{40}Ca and ^{48}Ca nuclei. While no low-lying strength was observed for the ^{40}Ca nucleus, first signatures of low-lying strength for the ^{48}Ca nucleus were observed in Ref. [112]. In the microscopic framework, neither RPA [15, 19] nor RRPA [35] methods predict any PDR for ^{48}Ca. It should be noted that recently the dipole strength in ^{40,48}Ca has been studied with the second-RPA, exhibiting a low-lying strength [106] in ^{48}Ca. Theoretical results from various models are analogous for oxygen and calcium isotopes in terms of fragmentation with the increase of the neutron number. Collective dipole excitations of the calcium isotopes ^{40,48}Ca are shown in Figure 4.3. The GDR is mainly located at 17.9 MeV (16.1% of EWSR) and 18.5 MeV (24.1% of EWSR) for ^{40}Ca and at 17.2 MeV (20.1% of EWSR) and 18.8 MeV (29.2% of EWSR) for ^{48}Ca nucleus. The centroid energies of ^{40}Ca and ^{48}Ca are 18.2 MeV and 18.3 MeV, respectively. The results are in agreement with the experimental results. Transition density analysis shows a pure IV character for GDR region as expected for both nuclei. In addition there is a low-energy mode between 12-13 MeV both for ^{40}Ca and ^{48}Ca, interpreted as the tail of the GDR because of the pure isovector motion of protons and neutrons in the corresponding transition density. This mode is also as collective as the GDR and destructive interferences are at work, explaining the small PDR strength compared to the GDR one.

The dipole response of the ^{70}Ca nucleus is plotted in Figure 4.4. The GDR response is strongly fragmented because of the extreme neutron excess. The centroid value of the energy in the GDR region is found at 17.3 MeV. A low-lying mode appears below the GDR region: the neutron rich ^{70}Ca nucleus has a low-lying strength at about 5.7 MeV with 1.09% of EWSR. In Ref. [113] the PDR motion for neutron-rich calcium isotopes was predicted isoscalar inside the nuclei and neutron on the surface. The transition densities analysis on Figure 4 allows to analyze this low-lying strength. Proton and neutron display both IV and IS motions in the interior of the nucleus and neutron motion on the surface which shows that this mode is not a tail of the GDR. Namely, the spatial behavior is decomposed into 3 parts: IV in the center of the nucleus, IS at average radii, and neutron on the surface. This specific mode of excitation corresponds to a so-called arch mode, because of the shape of the neutron density with respect to the proton one during this vibration. It exhibit a rather small collectivity and can be considered as a pure single-ph mode.

4.1.3 Nickel Isotopes

The results for the isovector dipole resonance and transition densities of ^{56}Ni nucleus with HF+RPA and Skyrme SLy4 interaction are illustrated on Figure 5. In the doubly magic ^{56}Ni nucleus (N=Z) the giant dipole resonance is located at about 19.1 MeV with 27.5% of EWSR and a centroid value is found as 18.5 MeV. Because of the equal contribution of protons and neutrons no low-lying mode is seen in this nuclei and results are in agreement

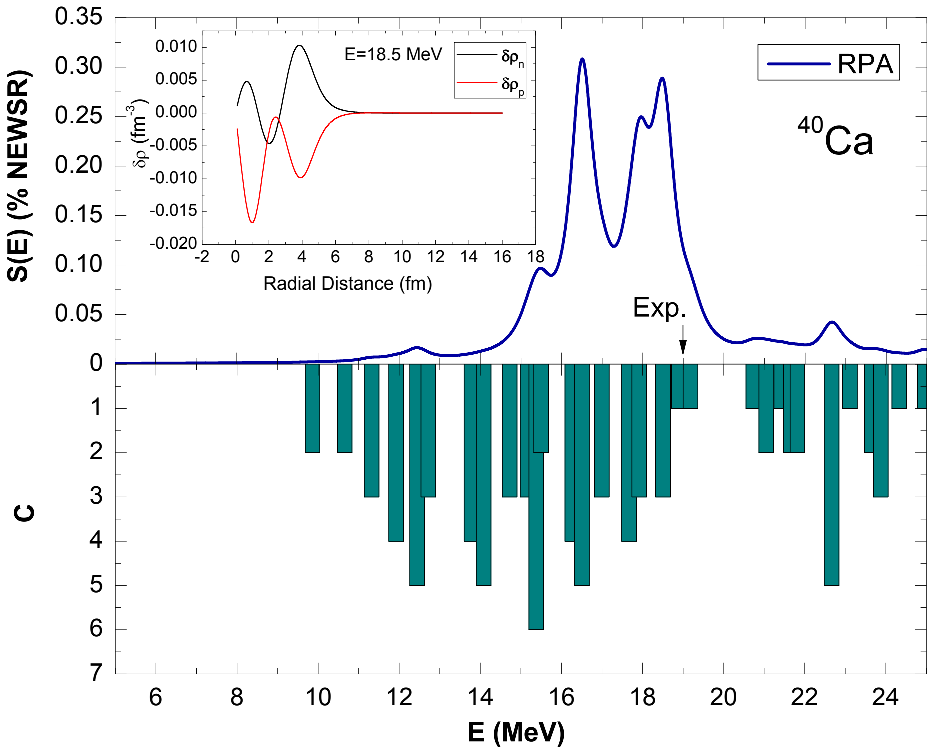

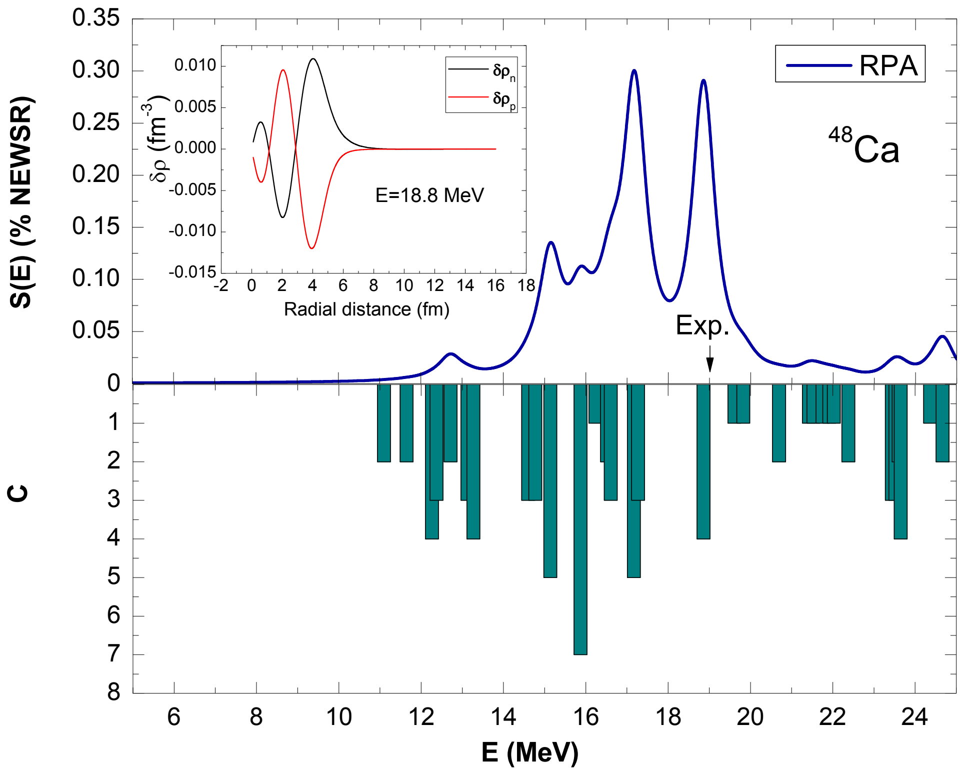

Figure 4.3 Same as in Figure 4.1 but for ^{40}Ca and ^{48}Ca nuclei. Experimental values of GDR are taken from Ref. [112].

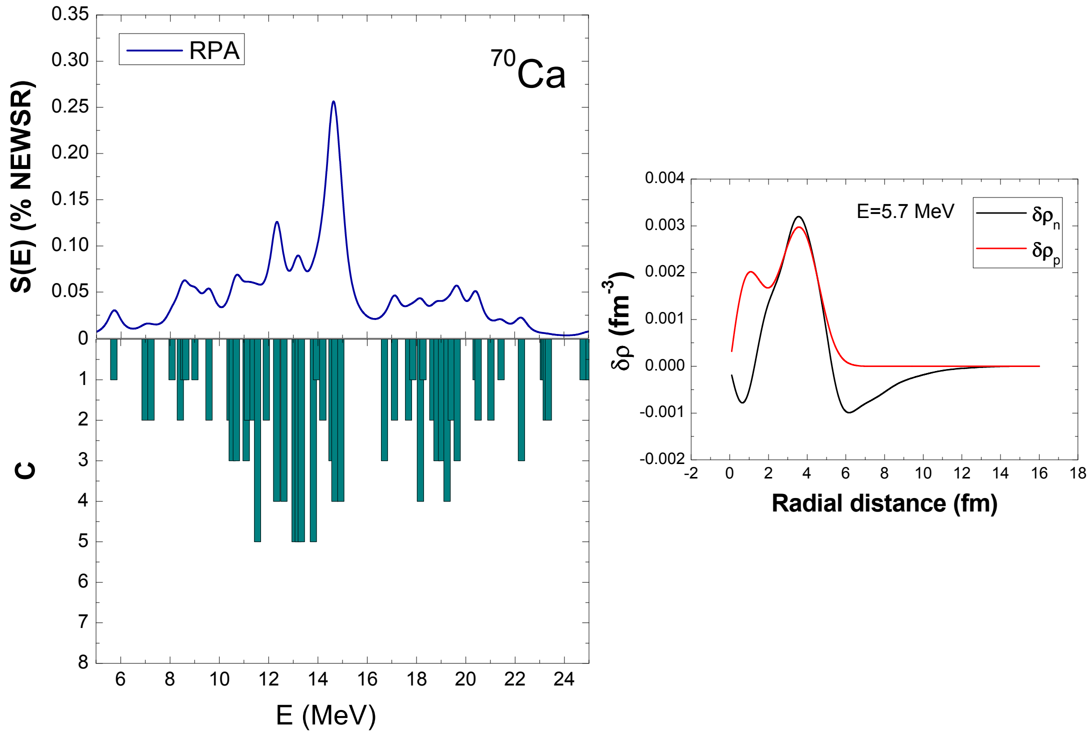

Figure 4.4 Left Panel:The RPA dipole strength distribution in the ^{70}Ca nucleus with the Skyrme type SLy4 interaction and collectivity C versus energy graph where C is defined by using Eq. (3.105). Right Panel: Neutron and proton transition densities for the PDR.

with the RRPA predictions of Ref. [35]. The transition densities analysis of ^{56}Ni shows an IV behavior, which is a general feature of GDR and given in Figure 4.5.

The investigation and interpretation of the PDR in ^{68}Ni have been made with microscopic RPA and RRPA models: ^{68}Ni exhibit a low-lying mode between 10.0-11.0 MeV [14, 35]. These results are also consistent with a recent experiment in which PDR value was found at about 11.0 MeV with the Coulomb excitation of ^{68}Ni nucleus at 600 MeV/nucleon [86]. In Figure 4.6 we plot the isovector dipole responses of ^{68}Ni and ^{78}Ni nuclei. The main GDR peak of ^{68}Ni is located at 17.7 MeV (27.1% of EWSR) and the PDR peak is approximately at 11.0 MeV (1.35% of EWSR). The GDR peak for ^{78}Ni is located at 15.5 MeV (19.56 % of EWSR) and the low-lying strength peak is at 9.8 MeV (0.43% of EWSR). The centroid energy values for ^{68}Ni and ^{78}Ni nuclei are found as 17.3 MeV and 17.2 MeV, respectively which is analogous to other models [35]. With the increase in neutron number, the dipole response of the ^{78}Ni nucleus is fragmented and the low-lying

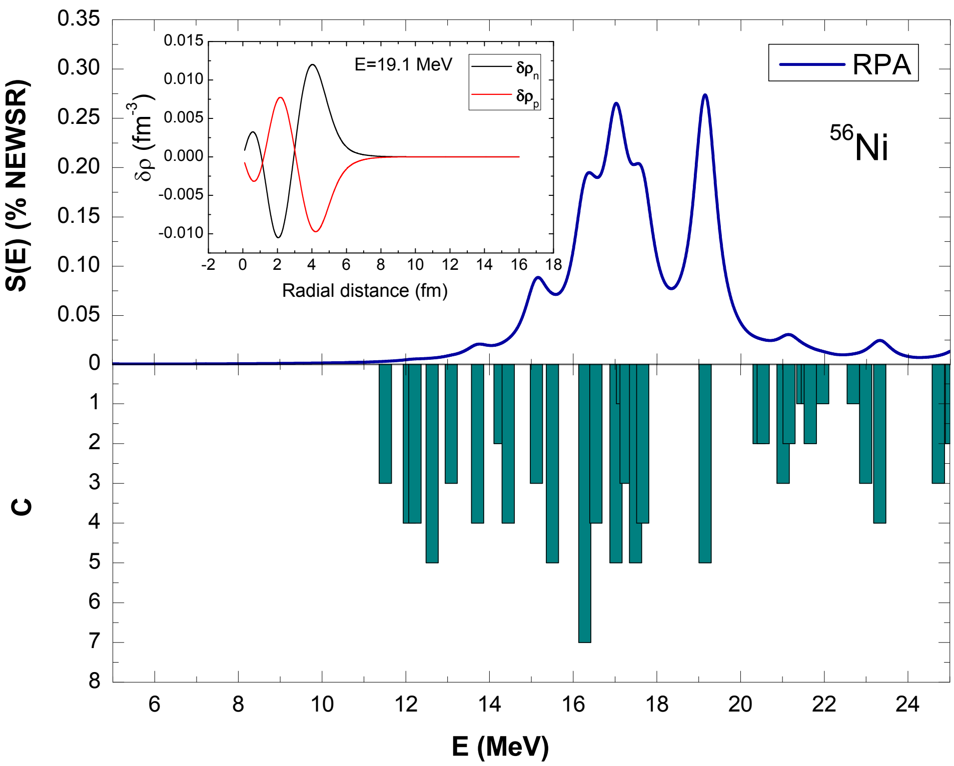

Figure 4.5 Same as in Figure 4.1 but for the doubly-magic ^{56}Ni nucleus. The GDR peak is located at 19.1 MeV.

response shifted to lower energy as in calcium and oxygen isotopes. Theoretical results with RPA [114] and RRPA [35, 38] methods also agree on the centroid of the PDR. In the right panel of Figure 6, the GDR and PDR transition densities are shown for ^{68}Ni and ^{78}Ni nuclei. The PDR is rather collective in both nuclei. The GDR exhibits usual IV behavior for both nuclei. But both ^{68}Ni and ^{78}Ni nuclei show very specific behavior in the low-lying part. The motion of nucleons in the inner part of the ^{68}Ni nucleus displays dominated IV behavior with isoscalar contribution until the surface, and on the surface neutron motion can be seen, which is a rather different interpretation from recent theoretical works [35, 115]. The PDR of ^{78}Ni exhibits an IV pattern inside the nucleus, and a more mixed IS+IV one on the surface. ^{78}Ni nucleus has much more neutrons and larger neutron skin than ^{68}Ni. However, in Figure 6 while ^{68}Ni nucleus has a pronounced neutron contribution on the surface, the neutron-rich ^{78}Ni nucleus has less neutron contribution on the surface. In addition, although there are only eight protons difference between ^{70}Ca and ^{78}Ni nuclei, the PDR pattern gives rather different motions in the transition densities analysis. This

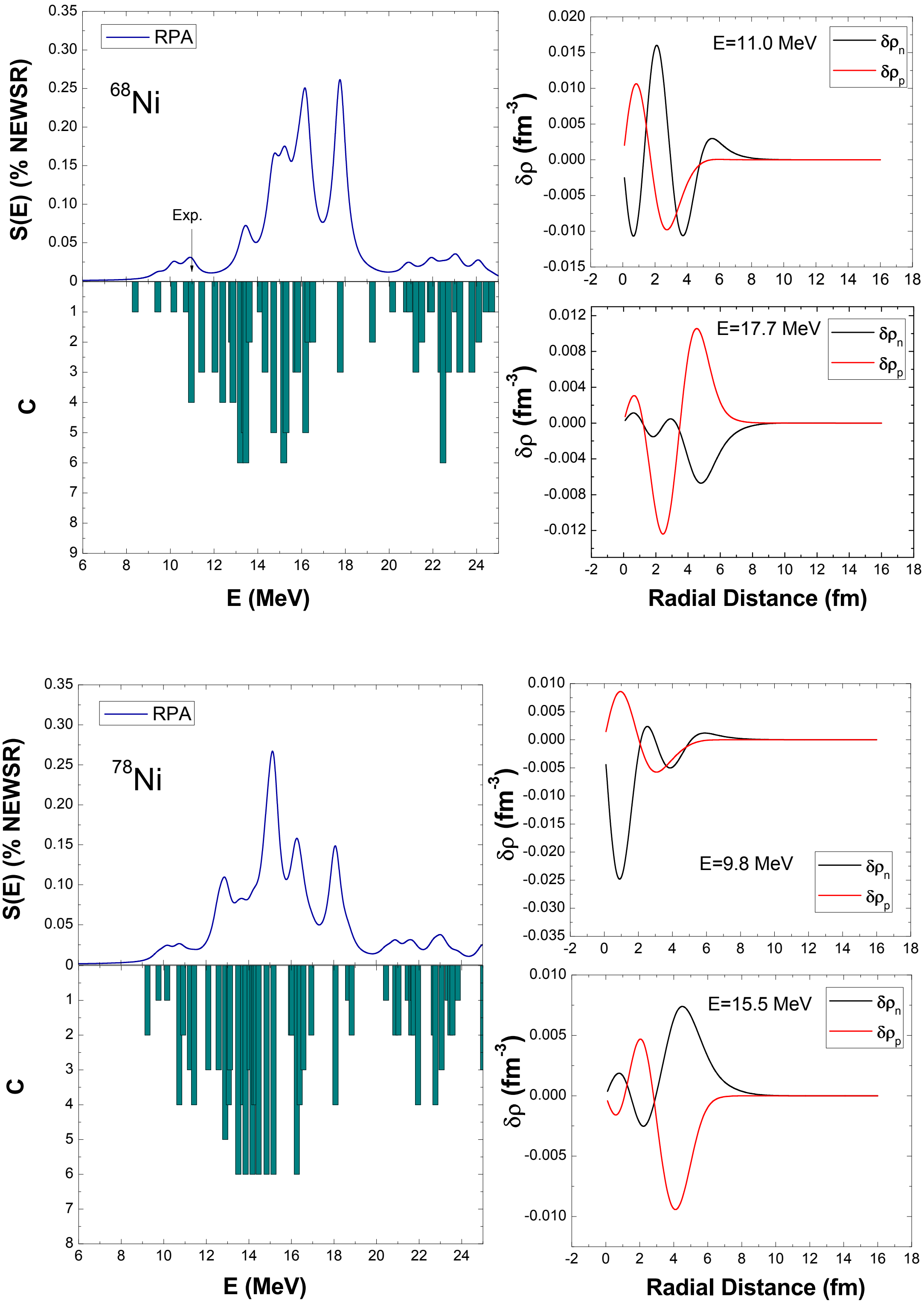

Figure 4.6 Same as in Figure 4.2 but for ^{68}Ni and ^{78}Ni. The experimental PDR value of ^{68}Ni is taken from Ref. [86].

change in motion can be attributed to the filling of the $1f_{7/2}$ level.

4.1.4 Tin Isotopes

Heavy doubly-magic tin nuclei were studied with different theoretical models and experiments. All models predicted that the low-lying strength strongly depends on the neutron excess [19,34,35,114,116–118]. The dipole response of tin neutron-rich nuclei is strongly fragmented with the increase in neutron number and the low-lying strength is shifted to lower energy. The PDR value is predicted below 10 MeV. Tin nuclei have a large isotopic chain which is experimentally accessible. Especially, low-lying modes can be analyzed with the increase of the neutron number.

In recent years, ^{100}Sn and ^{132}Sn nuclei were studied with different theoretical models and experiments. Experimentally the occurrence of a low-lying mode was found at about 9.8 MeV for ^{132}Sn nucleus [34]. Recently, the GDR and PDR of neutron-rich Sn isotopes were investigated with RPA [114] and RRPA [37, 119]. A low-lying strength was found between 8-10 MeV. All microscopic methods give similar results for transition densities of tin nuclei: IV motion in the GDR region and IS motion in the interior part of nuclei with neutron density motion on the surface for PDR region, i.e. the classical PDR picture. Various theoretical models predicted the nature of the PDR for ^{132}Sn as isoscalar dominated motion of protons and neutrons with neutron dominated motion on the surface [9, 35, 113, 120].

In Figure 4.7, the predicted dipole response of ^{100}Sn nucleus (N=Z) is displayed. The ^{100}Sn nucleus has no low-lying mode because of the equal number of protons and neutrons. It has a sharp peak at 15.2 MeV (16.1% of EWSR). However, the centroid value of the energy is 16.9 MeV, in agreement with another theoretical work using the relativistic RPA [35]. Transition densities of the ^{100}Sn state located at 15.2 MeV is given inside Figure 4.7, exhibiting IV character and interpreted as GDR because of the isovector motion of protons and neutrons.

The present RPA results for the neutron-rich ^{132}Sn are given in Figure 4.8. The centroid value of the GDR is found at 16.3 MeV. With the increase of neutron excess, a low-lying

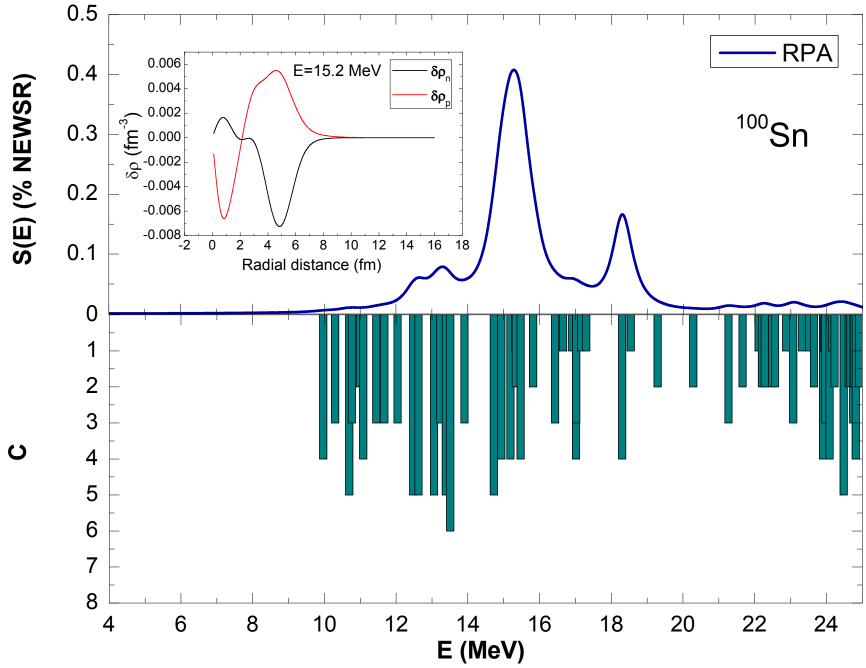

Figure 4.7 Same as in Figure 4.1 but for the doubly-magic ^{100}Sn nuclei with the GDR peak at 15.2 MeV.

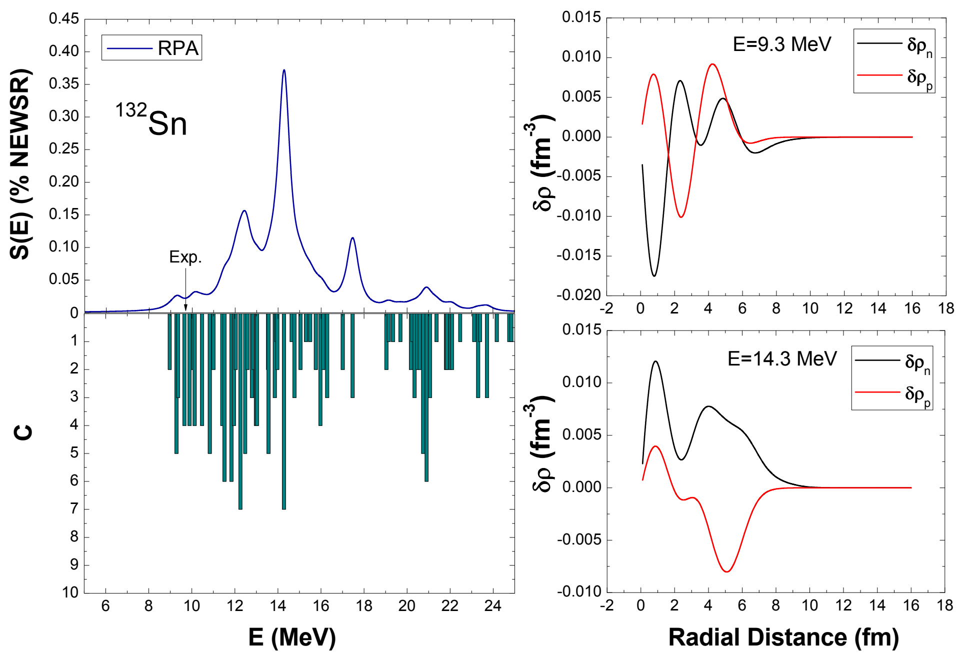

Figure 4.8 Same as in Figure 4.2 but for the doubly-magic ^{132}Sn nuclei with the GDR peak at 14.3 MeV and the PDR peak is at 9.3 MeV. The experimental value is taken from Ref. [34].

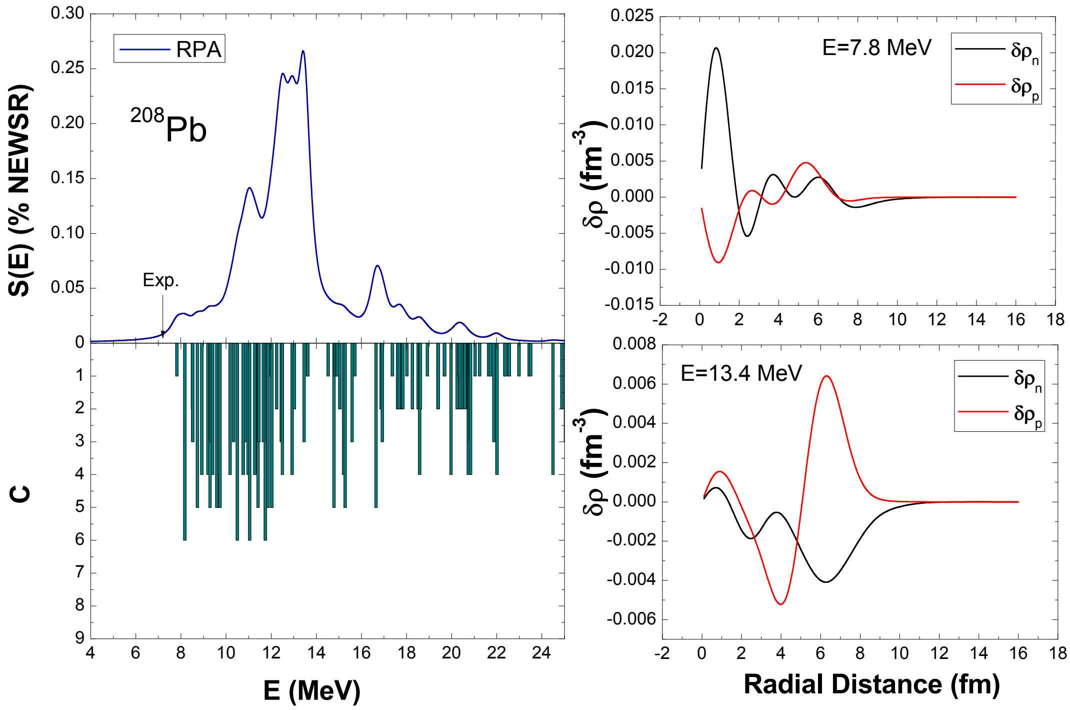

Figure 4.9 Same as in Figure 4.2 but for ^{208}Pb at 7.8 MeV and 13.4 MeV excitation energies. Experimental value of PDR value is taken from Ref. [122].

strength can be seen below the GDR region with a peak at 9.3 MeV. Transition densities are displayed in Figure 4.8 for both the PDR and the GDR located at 9.3 MeV (1.01% of EWSR) and 14.3 MeV (33.4% of EWSR) excitation energies, respectively. While the GDR has out of phase motion of proton and neutron densities, the PDR displays a mixed IS+IV motion. Other low-energy states of the PDR exhibit the same feature, having all a large collectivity. Although ^{132}Sn is a heavy neutron-rich nucleus, the neutron transition density is not strongly dominating over the proton one. The motion of nucleons in low-lying mode of ^{132}Sn nucleus is more analogous to ^{78}Ni: IV inside and isoscalar close to the surface.

4.1.5 Lead-208

Results for neutron-rich doubly magic ^{208}Pb nuclei are displayed in Figure 4.9. GDR is found at 13.4 MeV (20.4% of EWSR) for ^{208}Pb nucleus and in agreement with experimental results [121, 122]. In addition, the low-lying strength starts at 7.8 MeV (0.77% of

EWSR) and exhibits a collectivity similar to the GDR. It is 7.2 MeV experimentally and found between 7.0-11.0 MeV by several theoretical models in refs. [13, 36].

In Figure 4.9, the transition densities of protons and neutrons are also given. The results are rather different from the expected classical nature of PDR. We found a strong neutron dominated IV motion inside the nuclei and mixing of IS+IV motion on the surface as found in ^{78}Ni and ^{132}Sn nuclei.

4.2 Summary

Collective dipole excitations of different magic and doubly magic isotopic chains are studied within the framework of HF+RPA approximation over the nuclear chart using the SLy4 Skyrme interaction. The neutron excess has an important impact on the collective excitations of nuclei: with the increase in neutron number, high-lying modes are fragmented and a low-lying mode is formed, as already known from previous studies.

However, it is found that the main pattern of the PDR transition densities do not mainly depend on neutron excess and has rather complicated character, far from the PDR classical picture of neutron skin oscillations around a proton-neutron core. The proton and neutron transition densities analysis shows that the PDR is usually not pure IS or IV in the interior part of nuclei or pure IV outside. Instead it often shows a complex generic isoscalar and isovector feature which makes it different from the pure isovector nature of the GDR. With the neutron excess, the only common feature for the PDR among magic nuclei is its IV nature in the very interior of the nucleus, which is at variance with the classical PDR picture of a neutron skin oscillating around a proton-neutron core. In the case of ^{70}Ca, this leads to the so-called arch mode. Except in the case of the light ^{24}O nucleus, the PDR involves several particle-hole pairs, showing a non-negligible collectivity where destructive interferences between the particle-holes pairs can be at work.

In addition, changing the interaction to SGII gives similar results in transition density analysis. Pairing effects on transition densities of different isotopic chains will be investigated in a forthcoming work.

CHAPTER 5

THE SOFT GIANT MONOPOLE RESONANCE IN DOUBLY MAGIC NUCLEI

In this part of the thesis, we performed isoscalar monopole response calculations on closed-shell tin (Z=50) isotopic chain. Possible occurrence of low-lying strengths in the monopole response are investigated. In particular, we investigate the isoscalar monopole response, its collectivity and the relationship between the low-energy excitations and the evaluation of the spin-orbit splitting of closed shell nuclei. This chapter is based on the publication 'The Soft Giant Monopole Resonance as a probe of Spin-Orbit splitting' [123].

5.1 Details of the Calculations for the Monopole Spectrum

Considering closed shell ^{208}Pb nucleus and Tin isotopes, we performed calculations in the framework of the self-consistent Hartree-Fock + Random Phase Approximation in matrix formalism. This allows to describe the soft monopole mode in doubly magic nuclei such as ^{208}Pb and ^{100,132}Sn: pairing effects are known to blur the single-particle picture [105] and we prefer, as a first step, to analyze the situation in a pairing-free system.

The Skyrme SLy4 and SGII interactions are both used in HF and RPA calculations. All the terms of the residual interaction are calculated self-consistently, except for the spin-orbit and the Coulomb terms. The RPA calculations are done on top of the HF one, the same interaction being used in the HF and RPA models.

The HF+RPA model with Skyrme effective forces is well-known [9]. We only mention that the RPA equations are solved in configuration space, choosing the particle-hole space so as to exhaust the energy-weighted sum rules. The continuous part of the single-particle spectrum is discretized by diagonalizing the HF Hamiltonian on a harmonic oscillator basis with 12 shells. We checked the stability of the present results by increasing the number of shells. The present calculations are performed in a box of radius R=20 fm, and we also checked the stability of the results by increasing the box radius to R=30 fm. The GMR centroid is predicted using the m_1/m_0 sum rules ratio. A 600 keV smearing factor is used on the RPA response for presentation purposes.

5.1.1 Monopole Spectrum of Tin Nuclei

Figure 5.1 displays the strength function of the isoscalar Giant Monopole Resonance and its collectivity for the ^{100}Sn nucleus. The GMR centroid energy is predicted at about 18.8 MeV. Neutron and proton transition densities display an isoscalar (in phase motion of protons and neutrons) behavior for the GMR, as expected. In the low-energy part, while they show isovector (out of phase motion of protons and neutrons) motion in the interior of nuclei, mixed isoscalar and isovector motion can be seen through the surface of nucleus, and the proton transition density dominates. The low-energy part of the response calculated with SLy4 exhibits pure proton single particle excitations: ($1g_{9/2}$, $2g_{9/2}$) and ($2p_{3/2}$, $3p_{3/2}$) for 14.4 MeV and 16.1 MeV, respectively. This pure particle-hole configuration of the soft monopole strength explains the mixed isoscalar/isovector behavior of the excitation, which reflects the proton single-particle wavefunction at work. However, it should be noted that a different pattern is obtained in the case of SGII: there is almost no soft mode. This shows that in this N=Z nucleus, soft monopole modes are questionable. In the high-energy part of the response, the collectivity increases as a general behavior of giant resonances. Beyond the GMR the monopole response gives no strength in the 22-28 MeV part because particle-hole configurations interfere destructively.

The GMR centroid is located at 17.5 MeV for the neutron-rich ^{132}Sn nucleus as displayed on Fig. 5.2. The configuration analysis shows that the low-energy strengths corresponds to almost pure single neutron excitation: ($2d_{3/2}$, $3d_{3/2}$), ($3s_{1/2}$, $4s_{1/2}$), ($1h_{11/2}$, $2h_{11/2}$), ($2d_{5/2}$, $3d_{5/2}$) for the states located at 11.7 MeV, 12.1 MeV, 13.2 MeV and 14.3 MeV,

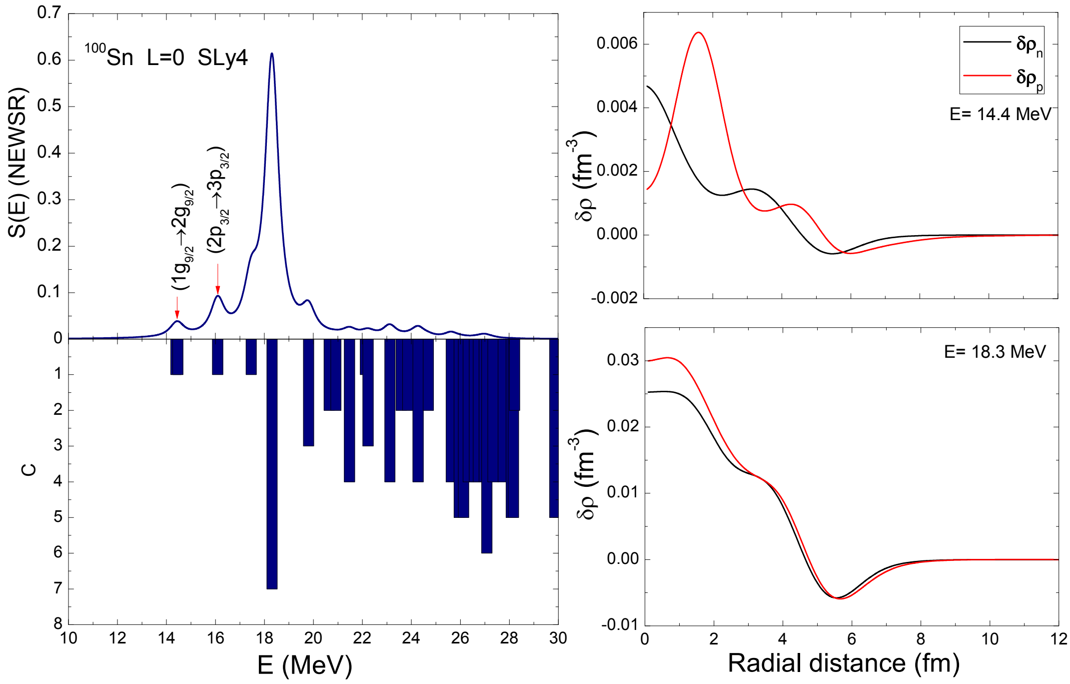

Figure 5.1 Left Panel: Calculations within RPA for the isoscalar monopole strength distribution in ^{100}Sn with Skyrme type SLy4 interaction. The collectivity C (Eq. (3.105), see text) is also displayed. Right panel: Transition densities for a soft monopole mode and the main contribution to the GMR.

respectively. In the low-energy part, the transition densities are neutron dominated. Very similar overall results are again found in the case of SGII, showing the reliable predictivity of the present results. Therefore, as noted in Ref. [23], the pure single particle-hole configuration is a recurrent pattern predicted for the soft monopole mode in neutron-excess nuclei.

Figure 5.3 shows the isoscalar GMR results with its collectivity for the ^{208}Pb nucleus. The GMR centroid energy is at about 14.6 MeV. As in the configuration analysis of ^{132}Sn nucleus, the low-energy strengths also corresponds to almost pure single neutron excitations: ($3p_{1/2}$, $4p_{1/2}$), ($3p_{3/2}$, $4p_{3/2}$) and ($2f_{5/2}$, $3f_{5/2}$) for the states located at 9.775 MeV, 10.87 MeV and 11.16 MeV, respectively. In the low-energy part, the transition densities are again neutron dominated. In the high energy part, the transition densities are not purely isoscalar. We also check our calculations with SGII interaction and same results are obtained.

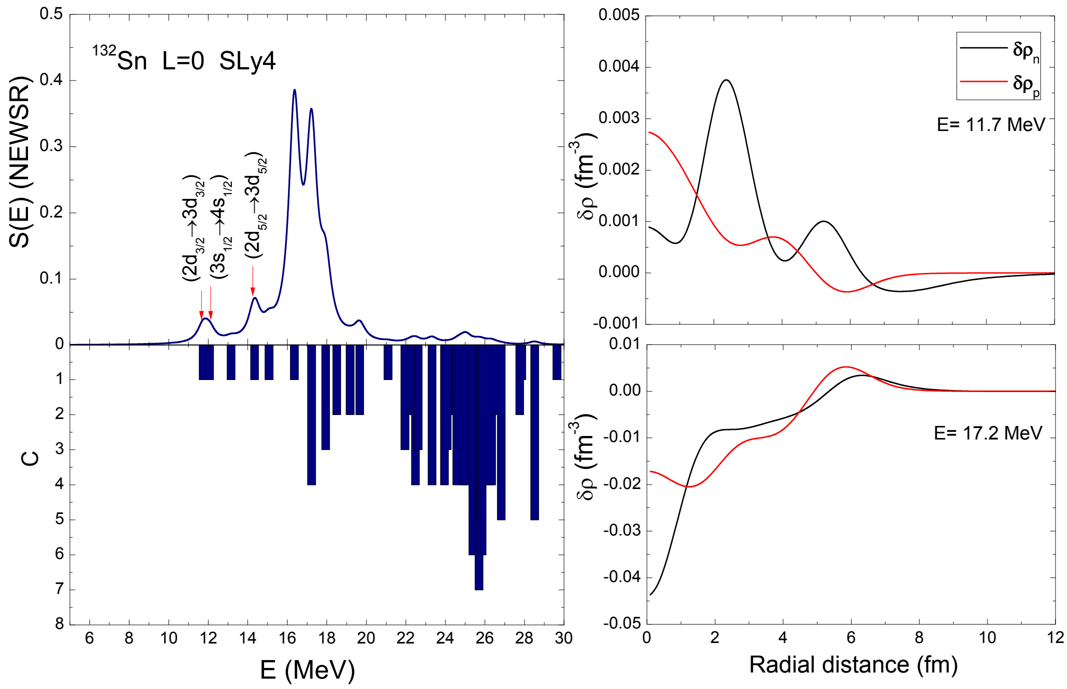

Figure 5.2 Same as in Fig.1 but for ^{132}Sn

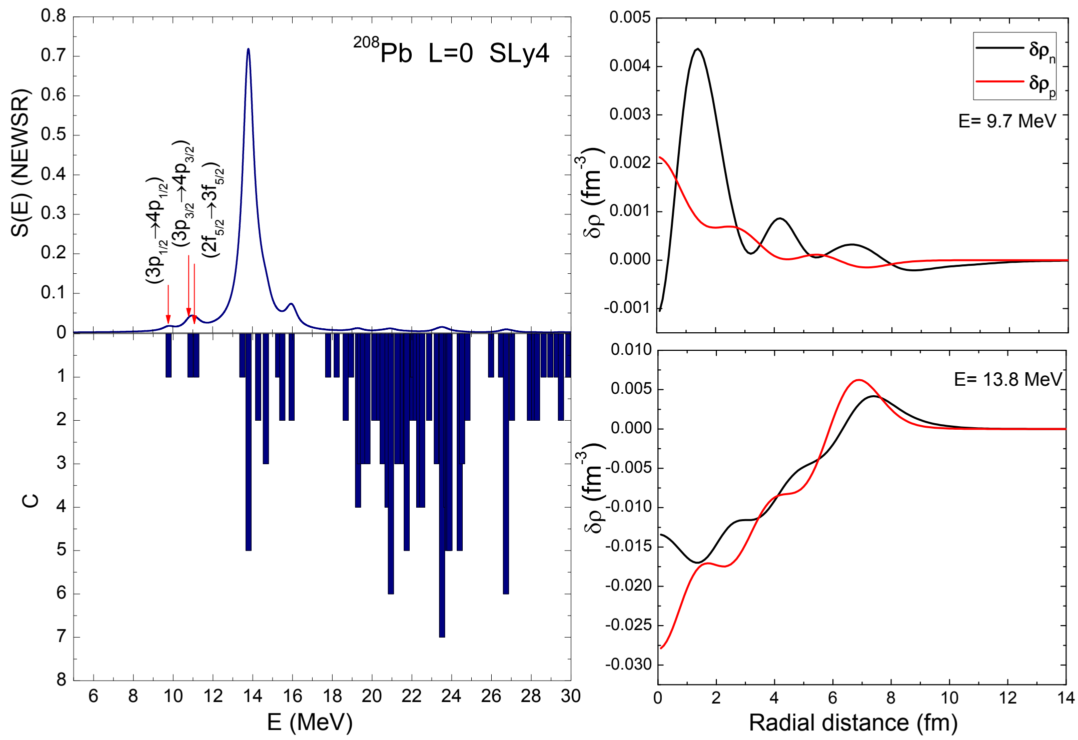

Figure 5.3 Same as in Fig.1 but for ^{208}Pb

Since the low-energy monopole strength arises from pure single-particle $2\hbar\omega$ excitations between the $4\hbar\omega$ and $6\hbar\omega$ energy levels for ^{132}Sn, the corresponding single neutron levels predicted with the HF calculations are displayed in Figure 5.4. The soft monopole modes are built from single particle-hole excitations between these two major shells, which can be identified with hole states close to the Fermi level. For instance, a part of the soft monopole mode is built with a particle from the $2d_{5/2}$ Fermi level feeding the $3d_{5/2}$ state. A similar figure is displayed for ^{208}Pb.

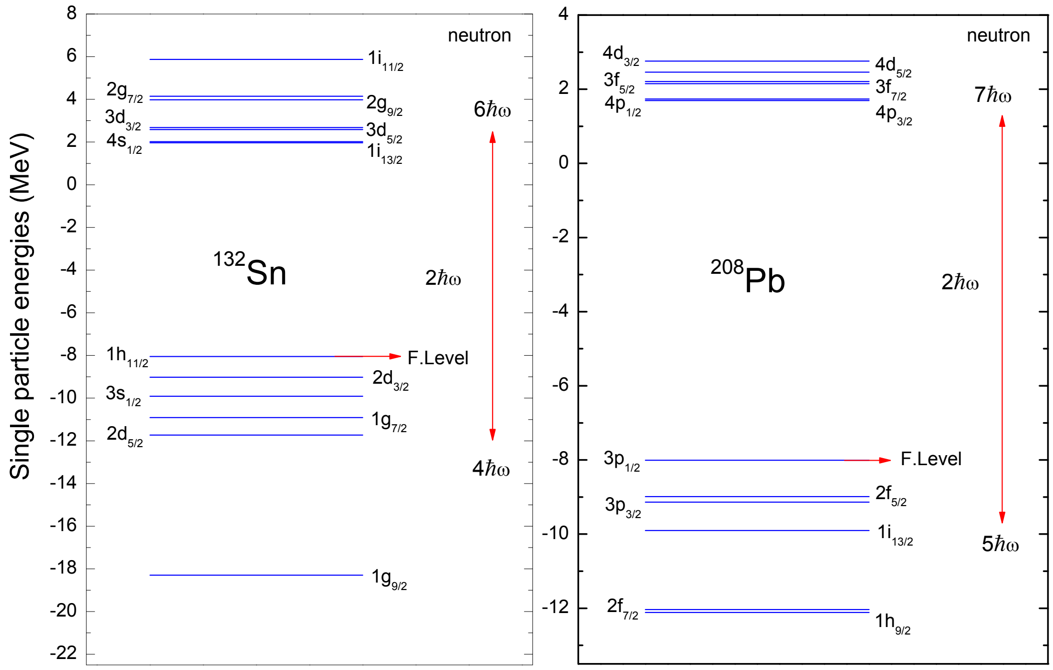

Figure 5.4 Left: Single neutron states for the ^{132}Sn nucleus in the $4\hbar\omega$ and $6\hbar\omega$ shells. The $5\hbar\omega$ is not shown. The Fermi Level is also displayed. Right: Same Figure but for ^{208}Pb.

It should be noted that similar results are obtained in open-shell ^{106,116,120}Sn nuclei within the RPA approximation, but in this case pairing effects are neglected. Relativistic QRPA calculations on Nickel isotopes have also shown that the single-particle feature of the soft monopole modes is universal [23].

5.1.2 Evaluation of the Spin-Orbit Splitting

Since almost all the low-energy monopole modes in the neutron-rich ^{208}Pb and Z=50 Tin isotopes are built from pure single neutron $2\hbar\omega$ excitations, the typical centroids of the soft modes (between 10 and 14 MeV as described above) shall provide an evaluation of the $2\hbar\omega$ gap value: for A = 132, $2\hbar\omega \simeq 13$ MeV leads to $\hbar\omega \simeq 30$ A$^{-1/3}$ MeV, at variance with the commonly admitted 40 A$^{-1/3}$ MeV value obtained with the harmonic oscillator. We obtain same conclusion for ^{208}Pb. This effect can be due to the discretized continuum approximation performed here, and should not be taken as a strong conclusion. However, the present method seems complementary to deduce the $\hbar\omega$ behavior compared to using the GMR, because there is no shift of the soft modes centroids due to the residual interaction, as showed in Ref. [23], contrarily to the GMR case where the residual interaction has an important effect on the centroid location.

The pure particle-hole excitations of the soft monopole modes can also be used to investigate the spin-orbit splitting and bring relevant spectroscopic information. Usually the spin-orbit splitting is analyzed using transfer reaction. Numerous data have already been obtained with (d,p) reactions on the position of the neutron single particle states (see e.g. [124]). However, these measurements rely on intra-shell analysis, involving possible core excitation, together with a DWBA prediction to assign spin and parity. We propose here to take advantage of the pure single particle excitation feature of the soft monopole mode to access to the spin-orbit effects, which could bring complementary informations with respect to the transfer reactions. The measurement through the soft monopole mode shall provide a direct measurement of the spin-orbit splitting.

It should be noted that the proper continuum treatment is important in the determination of the configurations of the single-particle excitations in the low-energy part of the spectrum. Using the exact continuum treatment, the interpretation for the low energy monopole is changed hindering the LS measurement. However in both cases (exact and discrete continuum), an increase of the GMR at low energy is predicted and it would therefore be relevant to measure it experimentally.

5.1.2.1 Lead-208

To make a first test of the method we consider the stable doubly magic ^{208}Pb nucleus. Single particle levels of ^{208}Pb nucleus is well known from experimental results. Experimentally, the energy differences between $3p_{1/2}-3p_{3/2}$ spin-orbit partners were found as 0.9 MeV [125] for ^{208}Pb. SLy4 interaction gives the energy differences between $3p_{1/2}-3p_{3/2}$ and $4p_{1/2}-4p_{3/2}$ spin-orbit partners as 1.13 MeV and 0.04 MeV, respectively. For ^{208}Pb nucleus, all low-energy monopole modes are built from single neutron $2\hbar\omega$ excitations between $5\hbar\omega$ and $7\hbar\omega$ energy levels. In order to evaluate the spin-orbit splitting, it should be noted that the soft monopole states allow to provide the 3p spin-orbit splitting $\Delta\varepsilon_{3p}$, taking advantage of the 4p states degeneracy ($\varepsilon_{4p1/2} \simeq \varepsilon_{4p3/2}$):

$$\Delta\varepsilon_{3p} \equiv \varepsilon_{3p1/2} - \varepsilon_{3p3/2} \simeq \varepsilon_{3p1/2} - \varepsilon_{4p1/2} - \varepsilon_{3p3/2} + \varepsilon_{4p3/2} = \Delta\varepsilon_{1/2} - \Delta\varepsilon_{3/2} \tag{5.1}$$

where $\Delta\varepsilon_{3/2,1/2}$ are the $2\hbar\omega$ energy difference between the 3p and 4p states for j=3/2 and 1/2, respectively. $\Delta\varepsilon_{3/2,1/2}$ therefore corresponds to the centroids of the soft monopoles states, which are located in ^{208}Pb at 10.87 and 9.78 MeV, respectively. Hence, Eq. (5.1) provides $\Delta\varepsilon_{3p} \simeq$10.87-9.78=1.09 MeV, which is in good agreement with the $\Delta\varepsilon_{3p}$ value. Moreover this value is also in good agreement with the experimental spin-orbit splitting measured in ^{208}Pb, which is 0.9 MeV. The results are also confirmed with SGII interaction. This shows the relevance of the method.

5.1.2.2 Tin Isotopes

In order to investigate this possibility for Sn isotopes, the d and g gaps obtained from the neutron single particle spectrum in the ^{100,132}Sn isotopes are displayed in Fig. 5.5 and 5.6, respectively. For convenience the results for ^{106,116,120}Sn nuclei are also displayed. With the increase of the neutron number, especially for ^{120}Sn and ^{132}Sn nuclei, the spin-orbit splitting is slightly decreased both in $4\hbar\omega$ and $6\hbar\omega$ energy shells but remains roughly constant. In Figure 5.5, while the energy difference between $2d_{3/2}$ and $2d_{5/2}$ spin-orbit splitting is around 2.7-3.3 MeV, the energy difference between $3d_{3/2}$ and $3d_{5/2}$ spin-orbit partners is found at around 0.11-0.14 MeV and nearly zero for ^{132}Sn. This expected vanishing of the spin-orbit splitting for unbound states is due to the fact that this splitting is proportional to the convolution of the density gradient with the wave functions. The density gradient is localized in the surface of the nucleus whereas the unbound wave functions are diluted in space. For those states, the convolution leads to a weak spin-orbit splitting, as previously noted in Ref. [126, 127]. In Figure 5.6, the spin-orbit splittings of both $1g_{7/2}$, $1g_{9/2}$ and $2g_{7/2}$, $2g_{9/2}$ are displayed. The splitting between the spin-orbit orbit partners of 1g level decreases of about 1.5 MeV from ^{100}Sn to ^{132}Sn in the $4\hbar\omega$ energy shell and it becomes almost zero for 2g level in the $6\hbar\omega$ energy shell. For ^{132}Sn nucleus, all low-energy monopole modes are built from single neutron $2\hbar\omega$ excitations between $4\hbar\omega$ and $6\hbar\omega$ energy levels. In order to probe the 2d spin orbit splitting from the soft monopole states, we solved Eq. (5.1) for 2d and 3d states instead of 3p and 4p states, using degeneracy of the 3d states ($\varepsilon_{3d3/2} \simeq \varepsilon_{3d5/2}$):

$$\Delta\varepsilon_{2d} \equiv \varepsilon_{2d3/2} - \varepsilon_{2d5/2} \simeq \varepsilon_{2d3/2} - \varepsilon_{3d3/2} - \varepsilon_{2d5/2} + \varepsilon_{3d5/2} = \Delta\varepsilon_{5/2} - \Delta\varepsilon_{3/2} \tag{5.2}$$

where $\Delta\varepsilon_{5/2,3/2}$ are the $2\hbar\omega$ energy difference between the 3d and 2d states for j=5/2 and 3/2, respectively. $\Delta\varepsilon_{5/2,3/2}$ therefore corresponds to the centroids of the soft monopoles states, which are located in ^{132}Sn at 14.3 and 11.7 MeV, respectively. Hence, Eq. (5.2) provides $\Delta\varepsilon_{2d} \simeq$14.3-11.7=2.6 MeV, which is in good agreement with the spin-orbit splitting observed on Figure 5.5, illustrating the validity of the method. For the g states, the degeneracy raising is too important among the 1g levels ($\Delta\varepsilon_{2g} \simeq 9$ MeV, see Fig. 5.6) to gather the two corresponding states in the low energy part of the response: some of these states are mixed in the GMR. The experimental values of the 2d states spin-orbit splitting is not straightforward to extract because in the case of the Tin isotopes, the doubly magic nuclei are far from stability: ^{100,132}Sn. The isotopes in between are semi-magic nuclei, where pairing effects are expected and could blur the interpretation of single particle states. In the case of ^{100,132}Sn, the 2d spin-orbit splitting has been estimated from data [128] and is 1.9 MeV and 1.7 MeV but with large uncertainties (about $\pm$ 700 keV for ^{100}Sn).

The coupling of the single-particle states to vibrational states could be further considered.

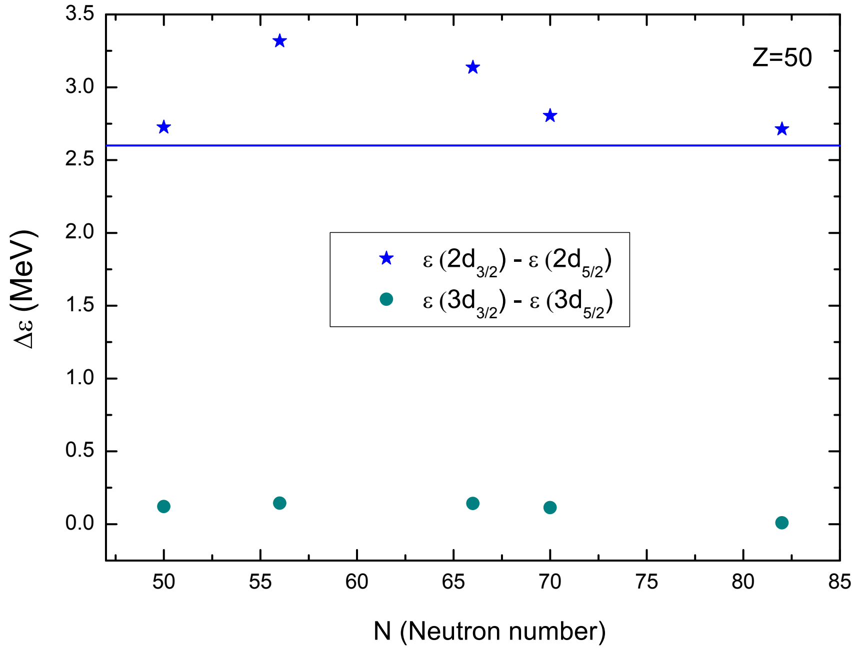

Figure 5.5 Single neutron energy differences predicted with the HF model between the $2d_{3/2}$ and $2d_{5/2}$ levels (stars) and the $3d_{3/2}$ and $3d_{5/2}$ levels (circles) along the Z=50 closed shell Tin isotopes. The horizontal line corresponds to the value deduced from the soft monopole modes in ^{132}Sn.

This effect is known to shift occupied and unoccupied states in opposite directions [129], increasing the level density around the Fermi surface. However, Eq. (5.2) involves differences between either occupied or unoccupied states, leading to smaller effects, of the order of several hundreds of keV in ^{132}Sn as noted in Ref. [51]. The particle-vibration coupling can affect the monopole response [130]. However, it seems more to affect the low energy tail of the GMR in N=Z nuclei. In (Fig 3.4) the case of the neutron-rich ^{48}Ca, there no effect of the ph vibration coupling on the soft monopole mode. Moreover, in the present work, we consider differences of soft monopoles modes, which could cancel possible systematic shift effects of the strength. Another limitation could come from the effect of the residual two body spin-orbit interaction which is neglected in the present work. It is known to shift the GMR centroid [131]. Similarly this possible effect is cancelled by the subtraction between two soft monopole modes.

Measurements of the soft monopole resonance in Tin isotopes are therefore called for.

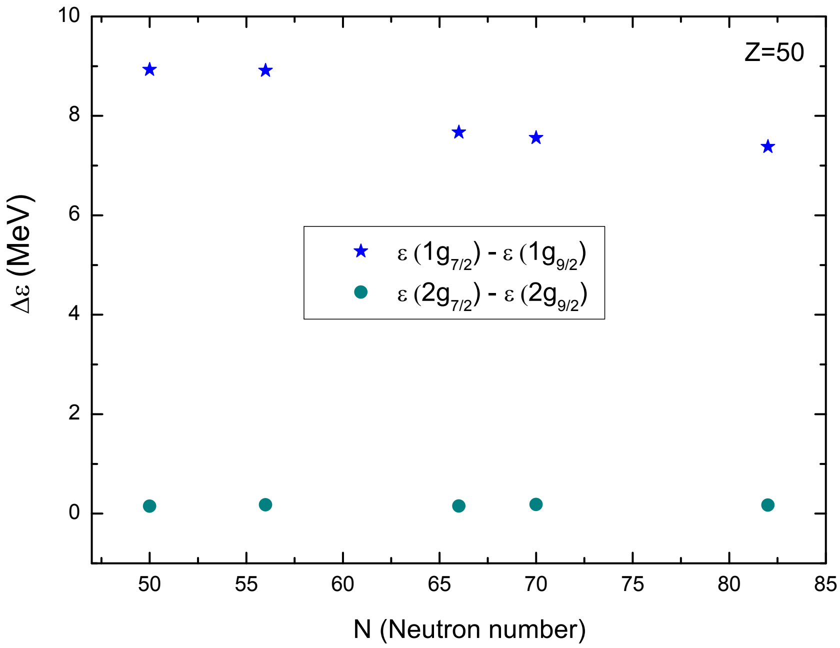

Figure 5.6 Same as Fig. 5.5 but for the g states

Such measurements have already been performed in the stable Tin isotopic chain. The corresponding data from Ref. [78] does not show a dramatic increase of the strength in stable Tin isotope at low energy, but some signal may be perceptible around 12 MeV in the case of ^{116}Sn. It should be noted however that the physical width of the monopole response (the spreading width, the decay width and the Landau damping) could also prevent from a clear separation between different low-energy states. More dedicated experiments focused on the low-energy part of the monopole response should be undertaken [41, 132].

The question arises if a similar analysis could be undertaken with the L=1 modes, which can also exhibit some rather non-collective features [133]. The collectivity of the soft dipole mode is currently under debate and may depend on the model considered. For instance, in the present Skyrme+RPA approach, the soft dipole mode is not a pure particle-hole configuration [104], and performing a similar analysis than in the monopole case is rather delicate.

5.2 Summary

The soft isoscalar monopole response has been predicted in doubly magic ^{208}Pb, ^{100,132}Sn nuclei using HF+RPA formalism and Skyrme SLy4 and SGII interactions. Pure particle-hole excitations are predicted in the low-energy region. Due to the specific L=0 multipolarity, these soft modes probe the shell structure through $2\hbar\omega$ gap excitations. They can be related to the spin-orbit splitting, providing a complementary information to transfer reaction measurements. The soft monopole mode is an excited states of the nucleus which is a different way to probe the shell structure compared to the transfer reactions, which is mostly sensitive to a specific single particle state of the nucleus.This last kind of experiment is of course advantageous to probe the spin-orbit splitting. However, fragmentation effects in the measurement through transfer reactions can be a drawback.

In the case of ^{132}Sn a good agreement is found between the 2d spin-orbit splitting and its evaluation from the soft monopole modes. Same calculations are performed for ^{208}Pb to check the validity of our results and 3p spin-orbit splitting is extracted from the low-energy single neutron excitations. Measurement of these modes are called for in order to check if they are distinguishable from the GMR.

CHAPTER 6

EFFECTS OF THE TENSOR FORCE ON THE FORMATION OF NEW MAGIC NUMBERS

One of the most important steps in the study of the atomic nuclei was the discovery of the nuclear magic numbers [43, 134]. Despite the great success of the spin-orbit force in explaining the closed shells and subshells in the nuclear stability valley, there is a long standing controversy about its adequacy near the drip lines. In recent years, both theoretical and experimental results indicate the formation of new magic numbers [44–50] and it seems that a large part of our knowledge about the location of magic numbers should be renewed in the near future.

Over the last few decades, there is an ongoing argument about the nature of the ^{54}Ca nucleus [135–139]. However, these studies could not reach a common conclusion about the magicity of the ^{54}Ca nucleus. One of the appropriate theoretical approach to predict nuclear shell effects is the self-consistent mean field method. This is the purpose of the present work.

In a recent experiment, very striking results were obtained by D. Steppenbeck et al. [50]. The data from the spectroscopic study of the neutron-rich ^{54}Ca nucleus using proton knock-out reactions reveal the doubly magic nature of this nucleus. The first 2^+ state is found at about 2 MeV, thus indicating a magic structure where the neutron $2p_{3/2} - 2p_{1/2}$ subshells would be occupied whereas the neutron $1f_{5/2}$ level would be empty. In order to get a clear understanding of the experimental results, theoretical predictions are thus needed.

In the last decade, it has been shown that the tensor force plays an active role in the shell evolution of nuclei. The tensor component of the effective N-N interaction contributes also to the spin-orbit part of the nuclear mean field and thus, it can affect considerably the single-particle (s.p.) energies [51, 97]. In the Hartree-Fock (HF) type of description, the tensor force is either added directly to the known Skyrme interactions (e.g., SLy5+T [51]) or all Skyrme terms including the tensor component are refitted on the empirical ground state properties (e.g., the TIJ family of force parameters, see Ref. [96]). Detailed explanations and more information about the tensor force can be found in Refs. [51, 97]. Recently, adding the tensor term to the known SLy5 force could explain well the experimental energy differences between the s.p. states of Z=50 isotopes and N=82 isotones [51]. In addition, the emergence of the magicity in the ^{52}Ca and ^{54}Ca nuclei occurs when Skyrme-Hartree-Fock calculations are performed with the SLy5 force plus an added tensor component [140]. In this framework, investigation of the tensor effects on the s.p. energies and the first J^{π}=2^{+} excited state can provide valuable information for the interpretation of the experimental results. This chapter is based on the publication 'Effects of the tensor force on the ground state and first 2^{+} states of the magic ^{54}Ca nucleus' [141].

6.1 Details of the Calculations

To study the effects of the tensor force on the s.p. energies of the N=34 isotonic chain, we compare the results obtained with SLy5, Sly5+T and T44 interactions. The SLy5+T and T44 interactions include tensor force components. In our calculations, the tensor interaction parameters are α_T =-170 MeV.fm^5, β_T =100 MeV.fm^5 for SLy5+T and α_T =8.96 MeV.fm^5, β_T =113.02 MeV.fm^5 for T44. In all calculations, we use a zero-range density-dependent surface-type pairing interaction (cite equation) [101]. The pairing strength ($V_0 = 350$ MeV. fm^3) is adjusted according to the experimental binding energies and two-neutron separation energies of the calcium isotopic chain (see 6.1). As can be seen from Figure 6.1, high pairing strength parameter creates unreliable results on the double magic ^{48}Ca. Also, binding energies of the Ca isotopic chain are more compatible with the experimental data [142] in case of the low pairing strength. Additionally, the first 2^{+} states of $^{42-46}$Ca isotopes have been used to obtain a proper pairing strength value. All Calculations are performed in a 20 fm box with 0.1 fm mesh size and a quasiparticle energy cut-off equal to 60 MeV. In our calculations, the maximum angular momentum value is taken as $j_{max.} = 39/2$ ($j_{max.} = 25/2$) for neutrons (protons). In the HFB approach the canonical quasiparticle energies E_i are given by $E_i = \sqrt{(\varepsilon_i - \lambda)^2 + \Delta_i^2}$ where ε_i is the so-called Hartree-Fock equivalent single-particle energy, λ is the chemical potential and Δ is the pairing gap which are defined in Ref. [143].

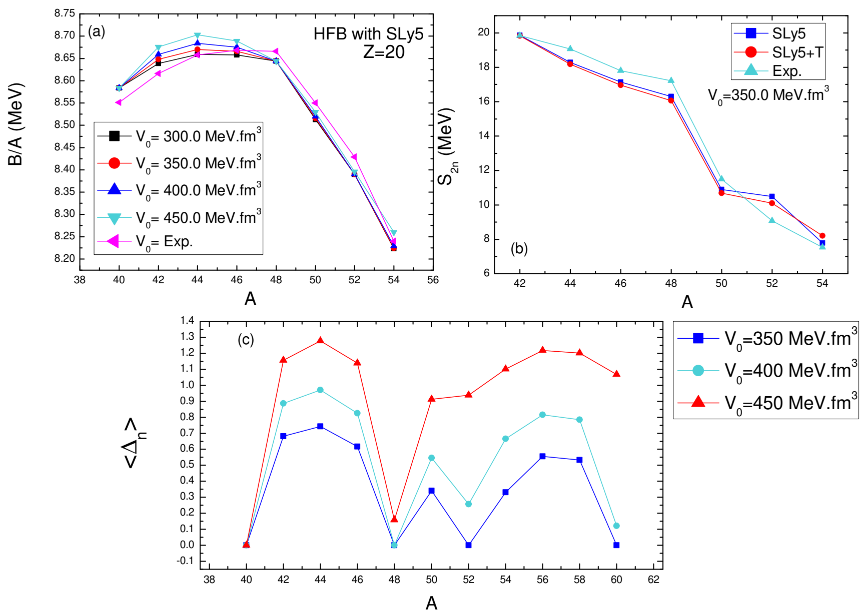

Figure 6.1 The Binding energies of Z=20 isotopes are calculated with HFB using Skyrme SLy5 interaction and different pairing interaction parameters (a). The two-neutron separation energies of nuclei with the selected pairing interaction parameter (b). Mean value of the neutron pairing gap as a function as a function of A (c). The experimental values are taken from [142] when needed.

In this work, as a first step we present the effect of the tensor force on the shell evolution of N=34 isotones: ^{60}Fe, ^{58}Cr, ^{56}Ti and ^{54}Ca nuclei with both Hartree-Fock-Bogoliubov (HFB) and HF+BCS models using the Skyrme-type SLy5 (without tensor) [108] and SLy5+T, T44 [96] (with tensor) interactions. For this purpose, The HF+BCS and HFB codes are modified in order to include tensor part of the Skyrme interaction. Among the many possible tensor parameter sets in the literature, we choose SLy5+T and T44 to illustrate the tensor force effects. The SLy5 interaction is designed for describing satisfactorily exotic nuclei [108]. Furthermore, addition of a tensor force on top of SLy5 helps to explain the observed s.p. spectrum [51], which makes Sly5+T appropriate for illustrating the tensor force effects. To check the reliability of the results, we also use T44 which is another Skyrme interaction containing a tensor component. Since the T44 interaction contains both the like-particle and proton-neutron tensor terms, it is also meaningful to study its predictions. The calculated s.p. energies with and without tensor force are compared at the mean field level. Then, the low-lying $J^{\pi}=2^{+}$ states are calculated within QRPA on top of HF+BCS for the Ca isotopic chain. Finally, conclusions are drawn on the possible magicity of ^{54}Ca. This chapter is based on the publication 'Effects of the tensor force on the ground state and First 2^{+} states of the magic ^{54}Ca nucleus' [141].

6.2 Single-Particle Spectra of N=34 Isotones

In this section, we discuss the calculated shell evolution of the N=34 isotonic chain using the HFB method [143]. In addition, we show that the HFB and HF+BCS methods yield very similar mean field properties, thus giving us more confidence in the quasi-particle (q.p.) RPA (QRPA) results presented in the next section. The details of the HF+BCS and HFB calculations can be found in Refs. [11, 143]. We present the results obtained with and without the tensor force in order to investigate the magic nature of the ^{54}Ca nucleus.

In the upper panel of Fig.6.2, we show the ε_i's in the N=34 isotones: ^{60}Fe, ^{58}Cr, ^{56}Ti and ^{54}Ca. They are calculated with the SLy5 interaction. With the removal of protons from ^{60}Fe to ^{54}Ca, the proton s.p. levels move down while the neutron s.p. levels move slightly up due to the increasing strength of the symmetry potential. Also, the spin-orbit splittings of proton (resp. neutron) p and f states increase (resp. decrease). The energy gap between the last occupied ($2p_{1/2}$) and first unoccupied ($1f_{5/2}$) neutron states increases by about 0.4 MeV when going from ^{60}Fe to ^{54}Ca. In ^{54}Ca, the neutron gap energy is 1.2 MeV with SLy5 and the pairing effects are weak. The results indicate a non-magic ^{54}Ca nucleus.

On the other hand, the results obtained with SLy5+T (lower panels of Fig.6.2) are somewhat different. They clearly indicate a neutron subshell closure at N=34. To better understand the influence of the tensor force on the neutron s.p. spectrum near the Fermi level in ^{54}Ca, we show in Fig. 6.3 the neutron s.p. levels for the p and f states. The HFB calculations are done with different Skyrme parametrizations, so as to check the model dependence of the results. Both SLy5+T and T44 interactions predict similar trends in the s.p. energies of N=34 isotones and they give no pairing in the ^{54}Ca nucleus. Comparing SLy5 and SLy5+T spectra clearly shows that the tensor force enhances the occupied-unoccupied level gap. To check the model dependence of the results, we have performed the same calculations with the T44 interaction [96]. The results obtained with SLy5+T and T44 indicate that this feature is not specific to a given parametrization of the tensor force but it seems to be general.

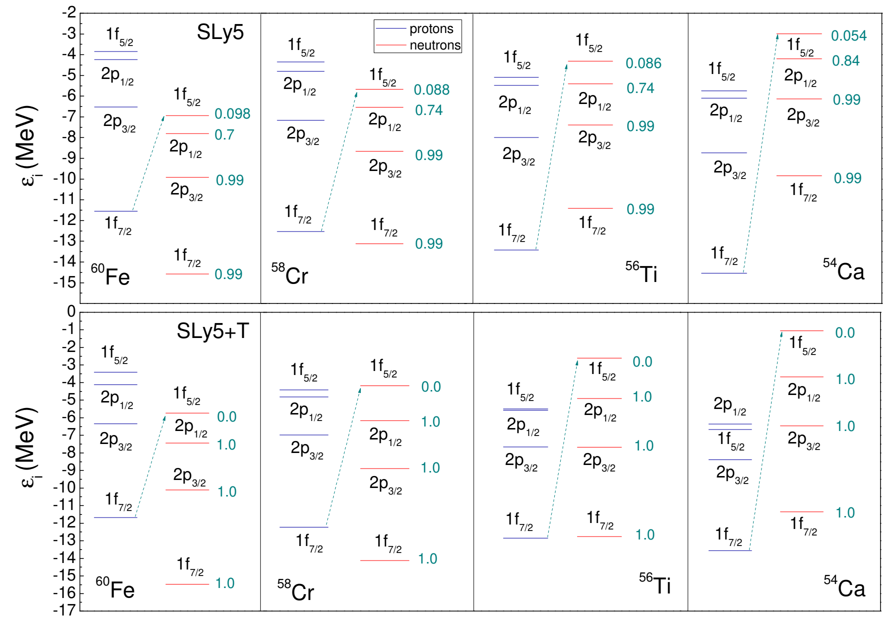

Figure 6.2 Evolution of the ε_i energies in N=34 isotones with two-proton removal in the nuclei ^{60}Fe, ^{58}Cr, ^{56}Ti and ^{54}Ca. The results with SLy5 and SLy5+T are displayed in the upper and lower panels, respectively. The occupation probabilities are shown for the neutron states.

We conclude that the inclusion of the tensor component of the Skyrme interaction is necessary for explaining the experimental results about the magic nature of the ^{54}Ca nucleus. We have also compared our HFB results with those of the HF+BCS method, with and without tensor interaction. Both HFB and HF+BCS methods give practically the same predictions. The maximum relative difference between the s.p. energies of the two methods is about 1.0%.

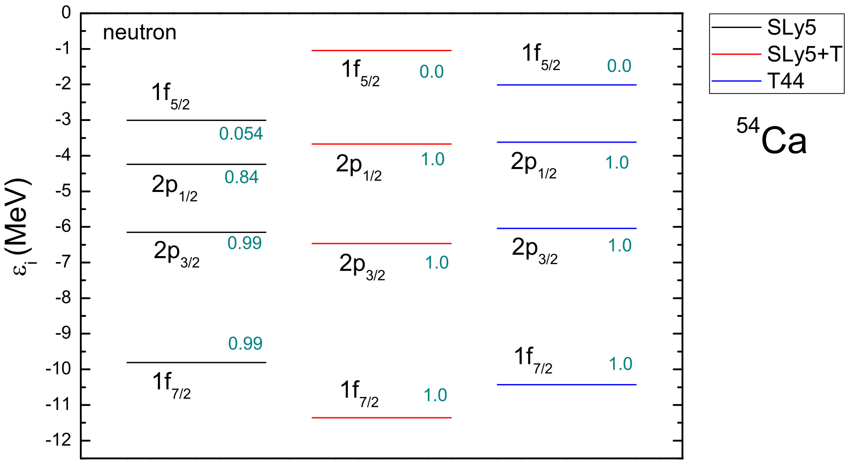

Figure 6.3 Same as in Fig. 6.2 for the neutron s.p. energies of ^{54}Ca calculated with SLy5, SLy5+T and T44 interactions.

6.3 Properties of the First 2^+ State in Calcium Isotopes

Another clue about the influence of pairing effects on the shell structure of Ca isotopes is found in the evolution of the first 2^+ state. Since the calculated q.p. spectra are very similar in HFB and HF+BCS descriptions, it is appropriate to perform QRPA calculations [11] on top of the HF+BCS scheme in order to study this evolution. Our aim is to see the effects of the tensor force on the first 2^+ state and to compare with the data in Ca isotopic chain. In the QRPA part of the calculations, Skyrme energy density functionals are used in the derivation of the p-h matrix elements which also includes spin-orbit and two-body Coulomb interactions [27]. It should be noted that the tensor force is just used in the mean field part of the calculations but it is not included in the residual interaction part of the present QRPA study. However, the effect of the residual p-h tensor interaction is expected to be rather small in the 2^+ excitations [144, 145].

The energies and B(E2) values of the first J^{π}=2^+ states are shown in Fig. 6.4. Experimental values are taken from Ref. [146]. In QRPA, the first 2^+ states of the Ca isotopes are coming from single 2-q.p. excitations. Inclusion of the tensor force has almost no effect from ^{42}Ca to ^{46}Ca and the predictions are in agreement with the data. However, the

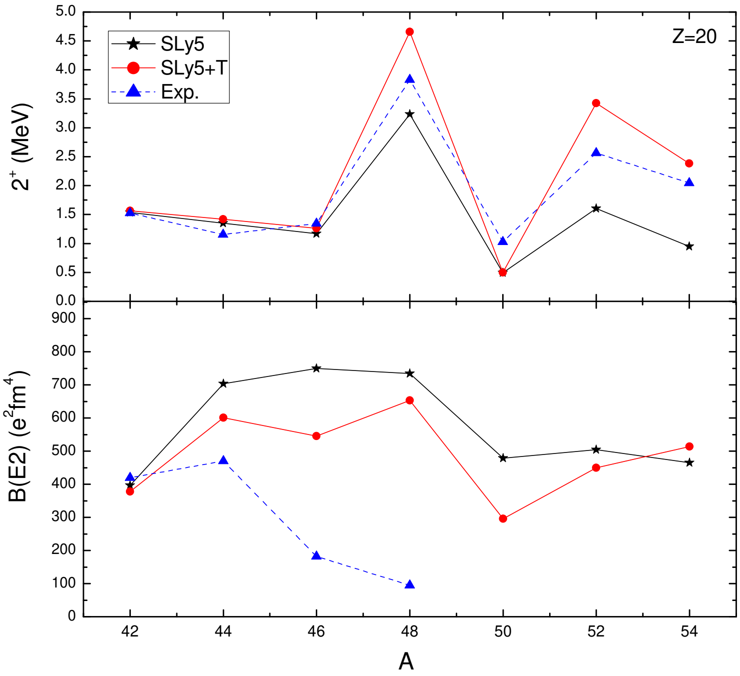

Figure 6.4 Upper panel: First J^{π}=2^+ energies in the $^{42-54}$Ca isotopic chain with and without tensor force in the mean field part. Experimental values are taken from Ref. [146] up to ^{52}Ca and Ref. [50] for ^{54}Ca nucleus. Lower Panel: B(E2) values. Experimental data are shown whenever available.

energies of the first 2^+ states in ^{48}Ca, ^{52}Ca and ^{54}Ca are increased by the tensor force. This increase is about 1.43 MeV, 1.82 MeV and 1.43 MeV, respectively. In addition, the first 2^+ states of the ^{48}Ca, ^{52}Ca and ^{54}Ca nuclei exhibit pure neutron s.p. excitations: ($1f_{7/2}$-$2p^{-1}_{3/2}$), ($2p_{3/2}$-$2p^{-1}_{1/2}$) and ($2p_{1/2}$-$1f^{-1}_{5/2}$), respectively.

The first 2^+ state of ^{54}Ca nucleus has been discussed before in shell model approach [136, 138] which are not able to predict the observed energies in Ref. [50]. In ^{54}Ca, we obtain a good agreement with the latest experimental results. Inclusion of the tensor force in the mean field part of the calculations explains well the behavior of the first 2^+ states in this nucleus.

In the lower panel of Fig. 6.4, we show the B(E2) values calculated with and without the tensor interaction. The tensor force does not modify much the B(E2) values, as expected. However, the QRPA B(E2) values with and without tensor force are not in agreement with the data. This is a general drawback of RPA and QRPA that the electromagnetic transition probabilities of collective low-lying states are generally not well described, even in stable nuclei. This may be related to the property that the RPA approach is better suited for describing collective modes corresponding to an irrotational flow in a hydrodynamic picture [147], which is the case for giant resonances but not so much so for low-lying electric modes.

6.4 Summary

In this work, we have employed both HFB and HF+BCS methods to study the ground states of N=34 isotones with the aim of exploring the possible magic nature of ^{54}Ca. The calculations were performed with Skyrme type interactions, without (SLy5) and with a tensor component (SLy5+T, T44). This choice is guided by the fact that the tensor force affects the s.p. spectra and thus, it can change the magicity behavior of those nuclei. The evolution of the s.p. spectra was explored. We do not obtain a clear sign of subshell closure with the SLy5 interaction, but the addition of a tensor force component quite enhances the energy difference between the s.p. states, thus leading to a subshell closure in ^{54}Ca. We have also investigated the first 2^+ states in the Ca isotopic chain, again with and without the tensor component in the Skyrme interaction. The tensor force leads to an increased energy of the first 2^+ state in the calcium isotopic chain. Both ^{52}Ca and ^{54}Ca show a magic nature. Especially, the first 2^+ state of ^{54}Ca is well reproduced when compared with the experimental results. However, the B(E2) values are not well reproduced, as it is often the case with QRPA applied to low-lying collective states in spherical nuclei. The results indicate the importance of the tensor force on the shell evolution of $p-f$ shell nuclei.

CHAPTER 7

EFFECT OF THE TEMPERATURE ON THE GROUND STATE PROPERTIES OF NUCLEI

Pairing correlations in open-shell nuclei are a crucial part of the mean field calculations which have been investigated over the years and taken into account within either Hartree Fock+BCS or HFB approximations at zero temperature. Over the last decades, the effect of temperature on mean field results has drawn attention due to the vanishing of pairing properties and the phase change of finite nuclei from superfluid to the normal state at critical temperatures. Extensions of the mean field models to the finite temperature case have been given in Refs. [52–54]. Thereafter, theoretical investigations have been undertaken with different models and interactions to investigate the relationship between pairing correlations and temperature.

First studies in hot finite nuclei were performed with Hartree-Fock-BCS model [52, 53]. It has been shown that pairing correlations disappear and nuclei undergo a sharp transition from superfluid to normal state at a critical temperature. Furthermore, the critical temperature and the pairing gap value at zero temperature follow the $T_c \simeq 0.567\Delta_{T=0}$ relation [52]. Pairing transitions in finite nuclei were also predicted within the finite temperature HFB models in Refs. [55–59]. Recently, the effect of different types of pairing interactions on the critical temperature and phase transition of Tin nuclei was investigated within FT-HFB approximation with zero-range Skyrme interaction. It was shown that the pairing gap value is sensitive to the type of the pairing force just below critical temperatures and the critical temperature follows the $T_c \simeq 0.5\Delta_{T=0}$ equation [148]. Very recently, the relationship between pairing and temperature effects was also investigated within the relativistic mean field (RMF) framework in even-even Ca, Ni, Sn and Pb isotopes in which the critical temperature follows the $T_c = 0.6\Delta_{T=0}$ relation [149]. Although the investigation of temperature effect on the pairing properties of nuclei is limited on the experimental side, some experimental signatures were also obtained from the level density measurements of the rare earth ^{161,162}Dy, ^{171,172}Yb nuclei. The observed S-shapes in the semi-experimental heat capacities of ^{161,162}Dy, ^{171,172}Yb [150] and ^{166,167}Er [151] nuclei were interpreted as the phase change of nuclei from superfluid to the normal state. In addition, the critical temperature at which the pairing correlations are disappearing was found at around 0.5 MeV.

Finite temperature effects are also important for astrophysical events, e.g., the reaction rates, r-process nucleosynthesis and core-collapse supernovae. Investigation of the superfluidity and specific heat in the inner crust matter of neutron stars have also been performed within the finite HFB framework in Refs. [152, 153]. It was shown that the temperature has an impact on the results and should be included in the calculations. Furthermore, the effect of temperature on the effective mass of nucleons, level density and symmetry energy is significant in the supernovae and electron capture rates which takes place at around $1 < T < 2$ MeV [129, 154–157]. Due to the influence of the temperature on the proton and neutron effective mass behavior and its connection with astrophysical events, effect of temperature on nuclei deserves further study. In this framework, the temperature sensitivity of the effective k-mass is revealed for the first time in a microscopic approach.

This chapter is based on the publication 'Effect of temperature on the effective mass and the neutron skin of nuclei' [158].

7.1 Finite Temperature Extension of Hartree Fock BCS Approximation

In the extension of the Hartree-Fock-BCS model to the finite temperature case, temperature dependent Fermi-Dirac distribution function is used:

$$f_i = [1 + exp(E_i/k_B T)]^{-1}, \tag{7.1}$$

where, E_k is quasiparticle energy, k_B is the Boltzmann constant and T is the temperature. In the BCS framework at finite temperature, the occupation factors are written as

$$v_i^2(1-f_i)+u_i^2 f_i \tag{7.2}$$

which also modifies the normal (particle, spin and kinetic energy) and abnormal densities. Such thermal averaged particle densities are given by [53, 152],

$$\rho_T(\mathbf{r}) = \frac{1}{4\pi}\sum_i (2j_i+1)\left[v_i^2(1-f_i)+u_i^2 f_i\right]|\phi_i(\mathbf{r})|^2, \tag{7.3}$$

$$\begin{aligned} J_T(\mathbf{r}) =& \frac{1}{4\pi}\sum_i (2j_i+1)\left[j_i(j_i+1)-l_i(l_i+1)-\frac{3}{4}\right] \\ &\times\left\{v_i^2(1-f_i)+u_i^2 f_i\right\}|\phi_i(\mathbf{r})|^2, \end{aligned} \tag{7.4}$$

$$\begin{aligned} \tau_T(\mathbf{r}) =& \frac{1}{4\pi}\sum_i (2j_i+1)\left[v_i^2(1-f_i)+u_i^2 f_i\right] \\ &\times\left[\left(\frac{d\phi_i(\mathbf{r})}{dr}-\frac{\phi_i(\mathbf{r})}{r}\right)^2+\frac{l_i(l_i+1)}{r^2}|\phi_i(\mathbf{r})|^2\right] \end{aligned} \tag{7.5}$$

$$\kappa_T(\mathbf{r}) = -\frac{1}{4\pi}\sum_i (2j_i+1)u_i v_i(1-2f_i)|\phi_i(\mathbf{r})|^2, \tag{7.6}$$

where v_i and u_i are the BCS variational parameters and $\phi_i(\mathbf{r})$ the single particle wave function. The Finite temperature Hartree-Fock BCS equations for the Skyrme interaction are obtained with the variation of the expectation value of $H^{'}$ 3.48.

At finite temperature, pairing field is given by

$$\Delta_T(\mathbf{r}) = \frac{V_{eff}(\rho(\mathbf{r}))}{2}\kappa_T(\mathbf{r}). \tag{7.7}$$

In addition, the particle number and pairing energy are also impacted with the temperature. The particle number is defined as

$$N_{q,T} = \sum_i (2j_i+1)\left[v_i^2(1-f_i)+u_i^2 f_i\right] \tag{7.8}$$

and the pairing energy is

$$E_{pair,T} = -\frac{\Delta_T(\mathbf{r})}{2}u_i v_i(2j+1). \tag{7.9}$$

7.2 Details of the Calculations

In this part of the thesis, fully self consistent calculations are performed for the first time within the finite temperature HFBCS (FT-HFBCS) framework using several types of Skyrme forces. Since we deal with u and v's in the HFBCS, the interpretation of the temperature effect is more straightforward when compared with HFB approximation. The density dependent surface-type pairing interaction (see Eq. 3.24) is used in the calculations. In order to provide a suitable pairing interaction, the pairing strength V_0 is fixed for each nuclei according to the $\Delta = 12/\sqrt{A}$MeV phenomenological rule.

Average neutron pairing gap is calculated via [159]:

$$\langle \Delta_n \rangle_\kappa = \frac{\int d\mathbf{r} \kappa_T(\mathbf{r}) \Delta_{T,n}(\mathbf{r})}{\int d\mathbf{r} \kappa_T(\mathbf{r})}. \tag{7.10}$$

Calculations are performed for temperatures up to 1.5 MeV to avoid occupation of unbound single particle levels and additional contributions from neutron vapour [160]. In the following study, it is relevant to derive the effective nucleon mass (m_q^*) in terms of the nucleon densities [10]

$$\begin{aligned} \frac{\hbar^2}{2m_q^*} =& \frac{\hbar^2}{2m} + \frac{1}{4}\left[t_1\left(1+\frac{x_1}{2}\right) + t_2\left(1+\frac{x_2}{2}\right)\right]\rho \\ &+ \frac{1}{8}\left[t_2\left(1+2x_2\right) - t_1\left(1+2x_1\right)\right]\rho_q. \end{aligned} \tag{7.11}$$

All calculations are performed in a 20 fm box with the assumption of spherical symmetry. The cut-off energy is determined with certain number of states around the Fermi energy. In our calculations, the pairing window (the number of levels above the Fermi level) is taken as 20 for both protons and neutrons. The energy difference between the Fermi and the last considered level is around 15 MeV which is large enough to take care of the occupation of levels due to temperature effects.

7.3 Numerical Results

7.3.1 About the Pairing Phase Transitions at Finite Temperatures

In panels (a) and (b) of Figure 7.1, the average neutron pairing gap is plotted as a function of temperature for ^{120}Sn and ^{112}Sn nuclei using various Skyrme interactions. The critical temperature for ^{120}Sn and ^{112}Sn nuclei are found at around 0.65 MeV. With the increase of the temperature, pairing correlations are destroyed below the Fermi level. As a result of the high temperature, Cooper pairs are broken and particles are excited to the higher energy levels which leads to the disappearance of pairing correlations [161].

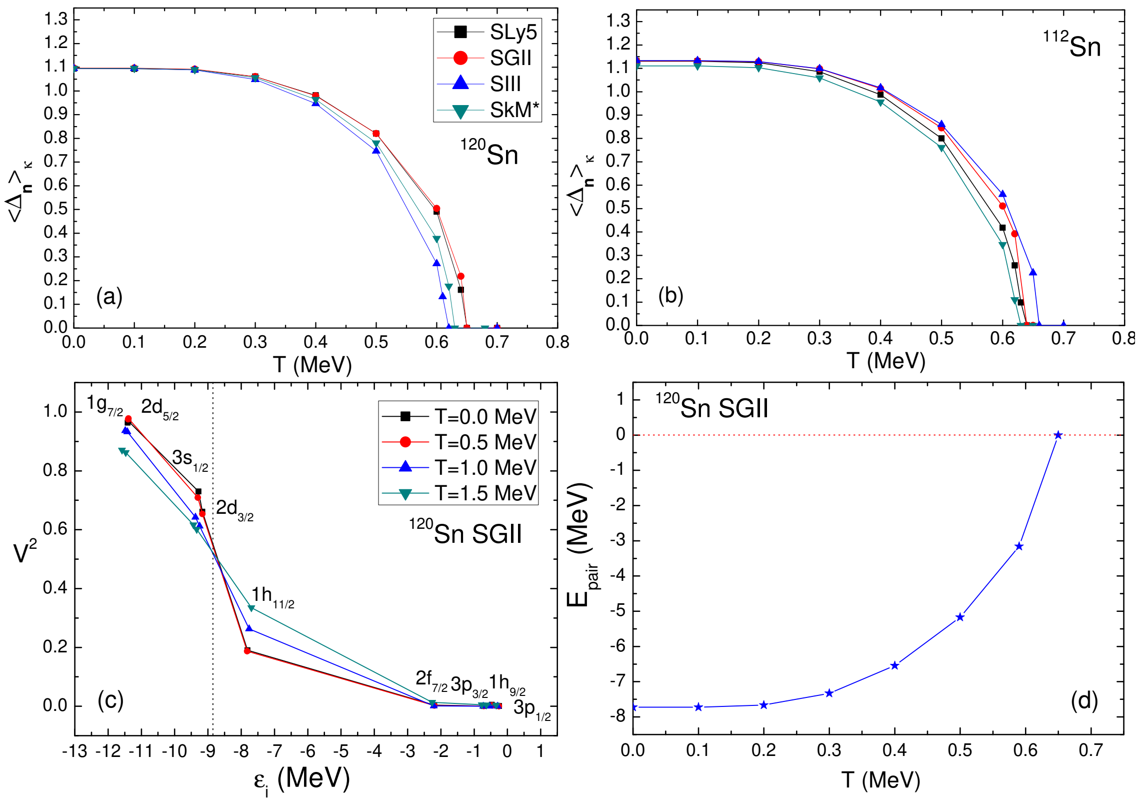

Figure 7.1 Mean value of the neutron pairing gap as a function of the temperature for ^{120}Sn (a) and ^{112}Sn nuclei (b), occupation probabilities for neutrons as a function of temperature around the Fermi level (c). In ^{120}Sn, the dotted line represents the Fermi level at T=0.0 MeV. Pairing energy as a function of temperature (d).

For the Skyrme interactions used (SLy5 [108], SGII [162], SIII [163], SkM* [164]), the critical temperature and the pairing gap value at zero temperature follow the $T_c \simeq 0.57\Delta_{T=0}$ rule. This is also consistent with the finite temperature HFB results in Ref. [148] in which the critical temperature was found around 0.7 MeV for the ^{124}Sn nucleus with

SLy4 interaction. Calculations are also performed in A=106 to A=124 even-even Tin isotopes and similar results are obtained. In order to provide a clear explanation for the vanishing pairing mechanism, in panel (c) of Fig. 7.1 we display the temperature dependence of the occupation probabilities with respect to the single particle energies of the ^{120}Sn nucleus using the SGII interaction. The single particle levels are chosen around the Fermi level, which are impacted by temperature. With the increase of the temperature, nucleons are excited to higher energies and occupation probabilities are increased above the Fermi level. Especially, the occupation probability of the $1h_{11/2}$ state just above the Fermi level increases above the critical temperature while the occupation probabilities of $3s_{1/2}$ and $2d_{3/2}$ states are decreasing below the Fermi level. In addition, the change of the pairing energy as a function of temperature is displayed in panel (d) of Fig. 7.1. Although the decrease of the pairing energy is small up to 0.3 MeV, a substantial decrease of the pairing energy is obtained for the temperatures between 0.3 MeV and 0.6 MeV. At critical temperature, the pairing energy is exactly zero, showing the vanishing of pairing correlations and interpreted as the phase change from superfluid to the normal state. The sharp transition is due to the limitation of the present approach which corresponds the grand-canonical ensemble [56]. Similar results are also obtained with other Tin isotopes and Skyrme interactions: SLy5, SIII and SkM*.

7.3.2 Effect of Temperature on the Neutron Skin

In panels (a) and (b) of Fig. 7.2, the change of the proton and neutron radii with respect to the temperature is displayed for the ^{120}Sn nucleus with SGII interaction. The interaction SGII [162] is one of the widely used parametrization of the Skyrme force. It has been derived from SkM*, by improving the Landau parameters and in particular $G_0^{'}$. This ensures a good description of spin states like the Gamow-Teller resonance, in addition to the reproduction of ground state masses and radii. The proton radius stays constant up to the critical temperature and then increases linearly. Although a small decrease is obtained in the case of the neutron radius up to the critical temperature, it also increases after critical temperature. The temperature dependence of the neutron skin $(R_n - R_p)$

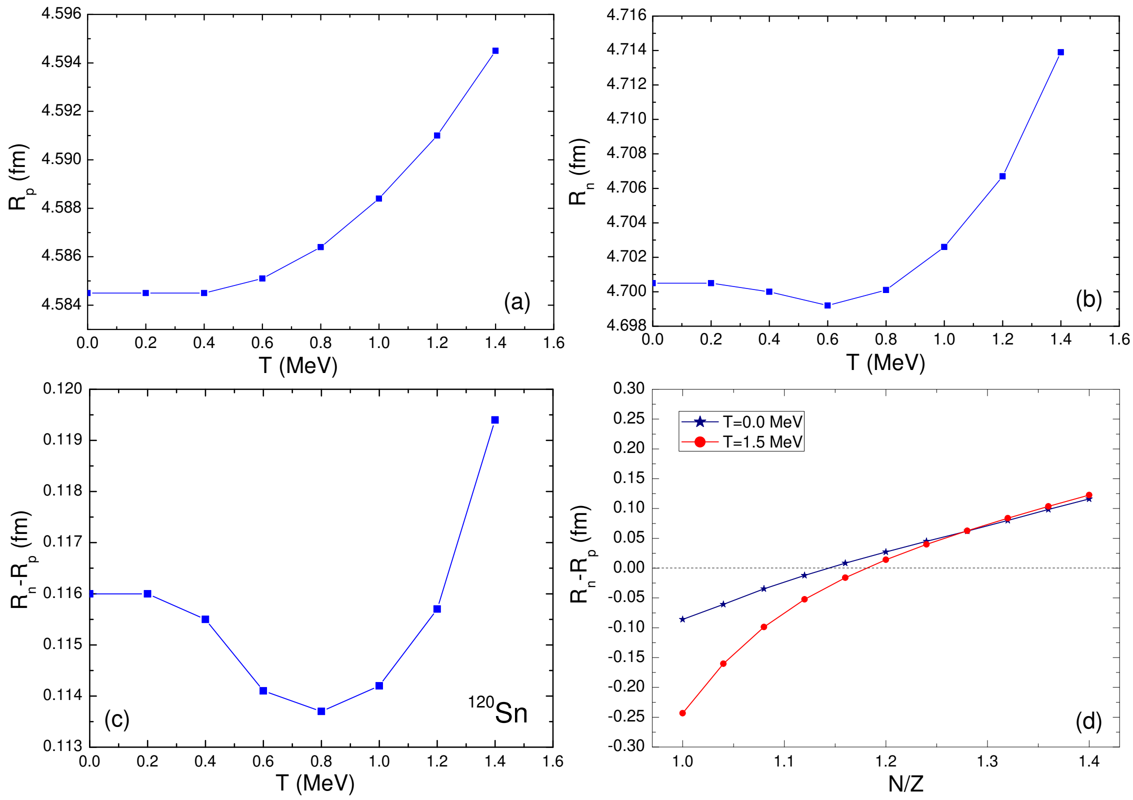

Figure 7.2 Proton (a) and neutron (b) radius with respect to the temperature for ^{120}Sn, calculated with SGII interaction and the change of neutron skin radius of ^{120}Sn nucleus with respect to the temperature (c). $R_n - R_p$ difference as a function of N/Z value for the Sn isotopes at T=0.0 MeV and T=1.5 MeV (d).

is also presented in the panels (c) and (d) of Fig. 7.2. In the case of ^{120}Sn although a small decrease is obtained before the critical temperature, the neutron skin increases of about 3% at temperatures above 1 MeV. This is due to the increasing population of larger single-particle states with larger angular momentum (l), such as the $1h_{11/2}$ state, as discussed above. Investigation of the effect of N/Z value on the temperature dependence of the neutron skin is also performed in the Tin isotopic chain. In panel (d) of Fig. 7.2, the $R_n - R_p$ difference with respect to N/Z value is displayed. It has been known that HFBCS is not suitable for drip line nuclei due to the formation of unphysical neutron gas [165].

Therefore, we limit our calculations up to ^{120}Sn nucleus in this part. Since both proton and neutron radii increase above the critical temperature, the proton radius weakens the formation of neutron skin in less neutron-rich Tin isotopes with the increase of the temperature. In order to further investigate the increase of the neutron skin with temperature, in Fig. 7.2 the neutron partial densities of states ($\rho_{nlj,T}(r)$) as a function of temperature

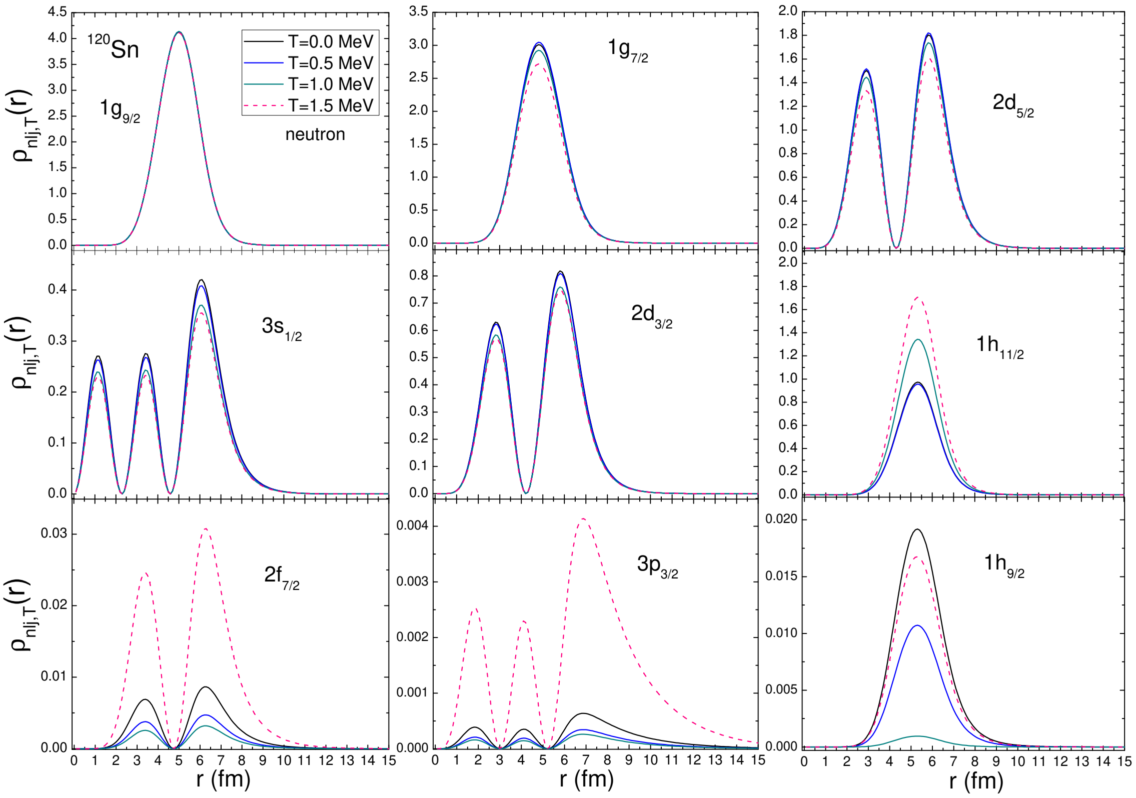

Figure 7.3 Neutron partial densities of states as a function of temperature for ^{120}Sn nucleus with SGII interaction.

are displayed for the ^{120}Sn nucleus. Since temperature impacts mostly the states around the Fermi level, the single neutron levels around the Fermi level are displayed. First, the effect of temperature is seen in the $1g_{7/2}$ single particle level which is below the Fermi level. While the neutron partial densities are decreasing below the Fermi level, an increase in the partial density of the $1h_{11/2}$ state just above the Fermi level is obtained at high temperatures. Proton partial densities also show a similar behavior: while partial densities decrease below Fermi level, an increase is obtained above the Fermi level at high temperatures. This causes an increase in the proton radius. In the case of the $2f_{7/2}$, $3p_{3/2}$ and $1h_{9/2}$ neutron states, a more subtle effect is at work: the partial densities decrease up to T=1.0 MeV and then increase. The decrease is due to the temperature effects which are destroying the small occupation number generated by pairing effects. Above 1 MeV, these states start to be repopulated by temperature effects, because of their increasing Fermi-Dirac factors (feeding from lower energy states).

7.3.3 Temperature Effects on Effective Masses

7.3.3.1 Effective Mass of Symmetric Nuclear Matter and T_c

In this section, our aim is to investigate the possible relation between the effective mass in symmetric nuclear matter (or equivalently m*(r=0)) and the critical temperature. The effective mass is known to impact the level density and pairing correlations which in turn may have an effect on the critical temperature [7, 129]. In our calculations, m^*/m values are ranging from 0.6 to 1.0 for the selected Skyrme energy density functionals.

In symmetric nuclear matter, effective masses for the Skyrme energy density functionals are defined as [108]:

$$\frac{m^*_{Sky.}}{m} = \left[1 + \frac{m\rho_0}{8\hbar^2}\left\{3t_1 + t_2\left(5 + 4x_2\right)\right\}\right]^{-1}, \tag{7.12}$$

where ρ_0 is the nuclear saturation density.

The upper panel of Figure 7.4 shows the influence of the effective mass values of the Skyrme energy density functionals (Eq.(7.12)) on the critical temperature of ^{120}Sn nucleus. Calculations are performed with 14 different Skyrme interactions, keeping the pairing strength constant, $V_0 = 680\ MeV.fm^3$, for all interactions used. A correlation between the effective mass and the critical temperature is obtained, namely with the increase in the effective mass values of the Skyrme interactions the critical temperature increases. Since a larger effective mass generates larger level densities and larger pairing gap values (see lower panel of Fig. 7.4) , the critical temperature at which the pairing correlations are disappearing is also larger. The pairing gap at zero temperature and the critical temperature are strongly correlated by the $T_c \simeq 0.57\Delta_{T=0}$ law and larger effective mass value generates a higher pairing gap value as expected. To check this interpretation, we also plot neutron single particle energies for the ^{120}Sn nucleus with SGI and SkX Skyrme interactions (see Fig. 7.5) which have 0.6 and 1.0 m^*/m values, respectively. SGI interaction has lower effective mass value and predicts larger energy difference between the $2d_{3/2}$ level and Fermi level (smaller level density).

This low level density around the Fermi level gives smaller pairing gap value. Therefore

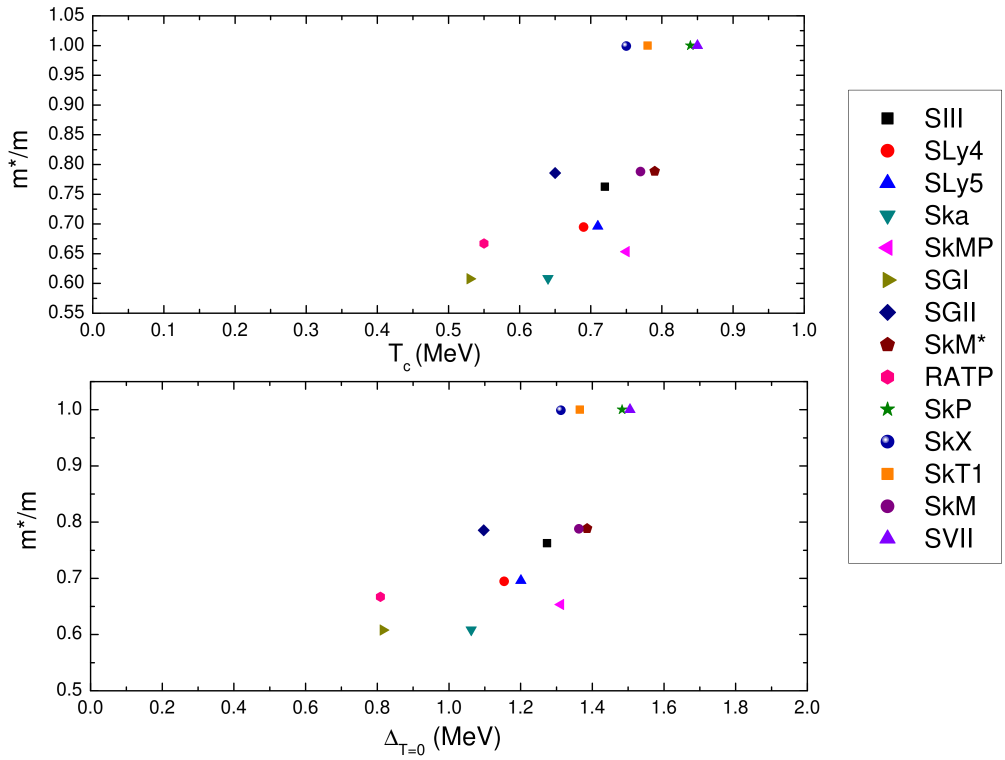

Figure 7.4 Upper Panel: Effective mass values with respect to the critical temperature. Lower Panel: Effective mass values with respect to the mean value of the pairing gap. Calculations are performed for ^{120}Sn nucleus using 14 different Skyrme interactions.

the critical temperature value for the phase transition is lowered. The SkX interaction has a larger effective mass and predicts smaller energy difference between the $2d_{3/2}$ level and Fermi level. Hence the level densities and pairing gap are enhanced which eventually causes a larger critical temperature value. We checked that same calculations with different Skyrme interactions give similar result.

It should be noted that in the case of imposing a constant pairing gap, the critical temperature is also constant due to the above relation between the pairing gap and the critical temperature. In this case the critical temperature dependence of the effective mass vanishes.

7.3.3.2 Temperature Dependence of the Effective Mass in Nuclei

In this section, we investigate the effect of temperature on the effective masses of nuclei. The total effective nucleon mass is obtained with the product of the effective k-mass and ω-mass ($m^*/m = m_w m_k/m^2$). While the k-mass comes from the spatial non-localities

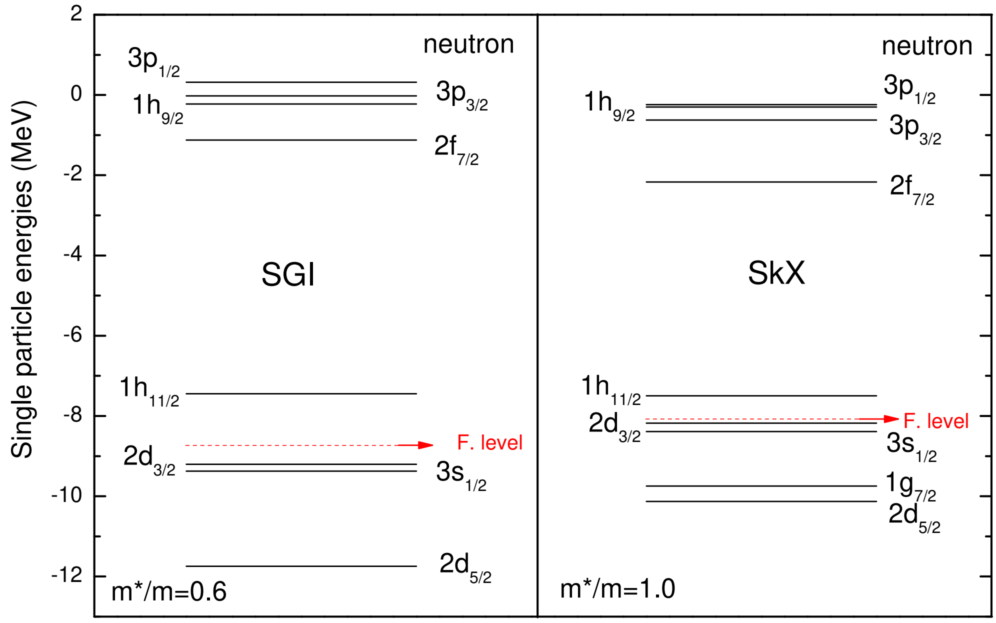

Figure 7.5 Neutron single particle energies around the Fermi level for ^{120}Sn nucleus with SGI and SkX interactions, at zero temperature.

and is obtained from the mean field calculations, the ω-mass is related to the frequency dependence of the mean field [155].

The level densities around the Fermi level are affected with the changes in the effective mass as discussed above. Therefore the determination of the temperature dependence of the effective mass is an important task for the level density calculations. The temperature dependence of the effective nucleon mass of nuclei have been previously studied in Refs. [154, 155, 166, 167]. The results indicate a decrease of the effective nucleon masses at high temperatures. Therefore the nuclear symmetry energy and electron capture rates in the stellar core collapse, which takes place at 1-2 MeV temperature are also affected [155]. In Ref. [154], the temperature dependence of the effective ω-mass was investigated with respect to the temperature. The effective mass was found to decrease which decreases the level density and increases symmetry energy at high temperatures. The changes in the effective proton and neutron masses might have some effects on astrophysical events; for example in the electron capture rates of stellar collapses [154]. Since the rate of the electron capture is closely related with the proton and neutron chemical potentials and consequently with the symmetry energy, an increase or decrease in the effective nucleon masses might lead significant changes in these rates.

In this framework, in the left part of Fig. 7.6, the effect of temperature on the effective k-masses (at r=0, Eq.(7.11)) of protons and neutrons are displayed. The results are shown for ^{120}Sn nucleus with SGII interaction.

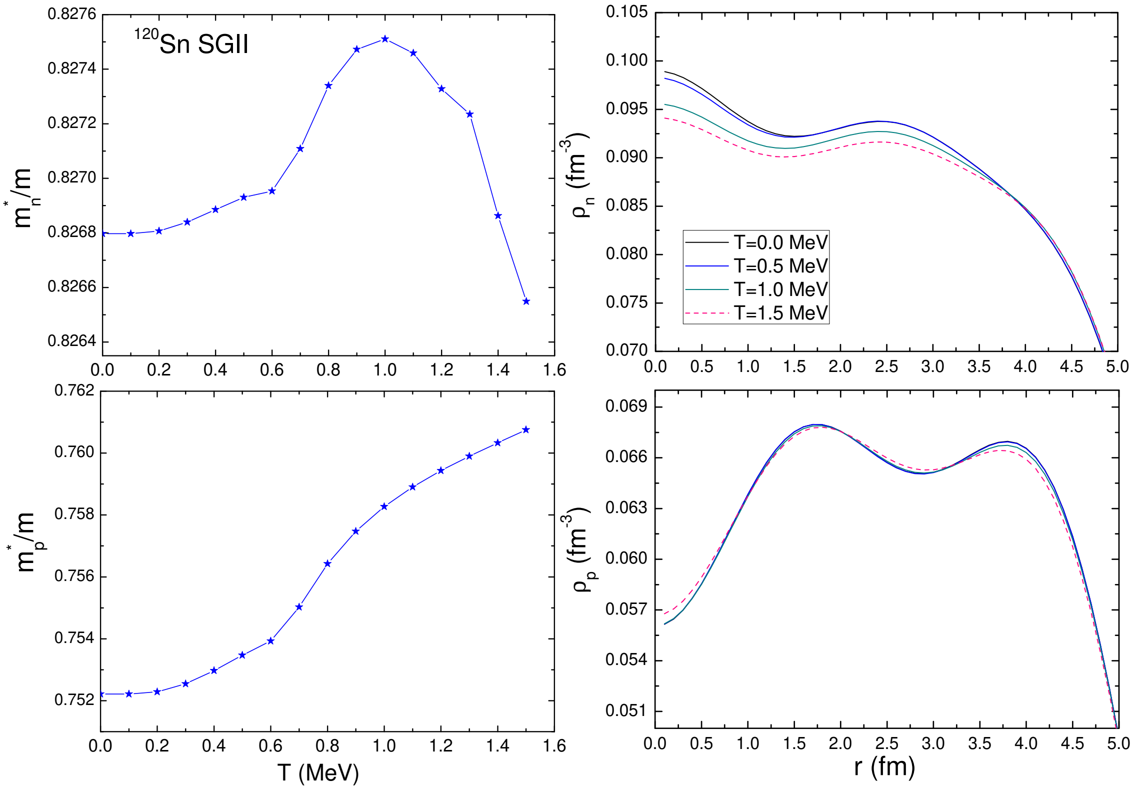

Figure 7.6 Left Panel: Effect of temperature on the neutron and proton effective masses (at r=0) for ^{120}Sn nucleus with SGII interaction. Right Panel: proton and neutron densities with respect to the temperature.

An increase of the effective neutron mass up to T=1.0 MeV is observed in the interior of the nuclei. Thereafter, the effective neutron mass suddenly decreases from T=1.0 MeV to T=1.5 MeV. In addition, the increase of the proton effective mass is much more pronounced after the critical temperature. The change is about 1.13% for proton effective mass. Although the changes in the effective masses are small in magnitude as mentioned in previous works [155], it may be relevant to accurately study its behavior. To explain the behavior of the effective proton and neutron masses, we rewrite Eq.(7.11) using the values of the SGII parameters:

$$\frac{\hbar^2}{2m_q^*} = \frac{\hbar^2}{2m} + \left(64.56(MeV.fm^5)\rho - 57.67(MeV.fm^5)\rho_q\right) \tag{7.13}$$

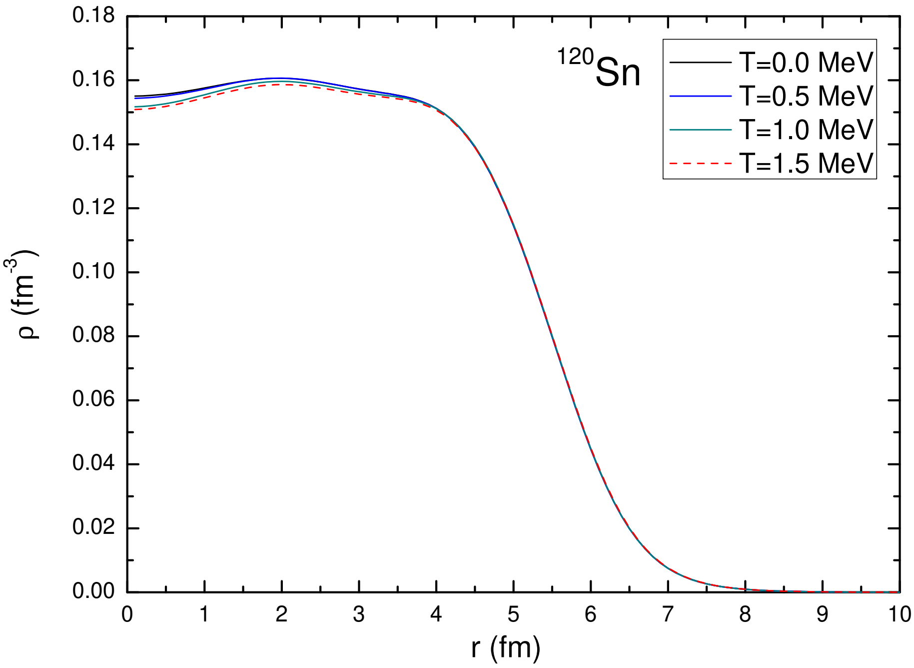

Figure 7.7 Change of the total density with respect to the temperature in ^{120}Sn.

The changes in the effective masses depend on the density but not explicitly on the temperature. Therefore, the temperature dependence of the effective masses come indirectly from the temperature dependence of the density. (Eq.(7.13)). The total density is displayed in Fig. 7.7. In the center of the nucleus, the total density decreases with increasing temperature. Therefore the effective mass is expected to increase with increasing temperature, but there is also the effect of the isospin dependent density in Eq.(7.13): in the right part of Fig. 7.6, we display the change of the neutron and proton densities with respect to the temperature. The effect of temperature on the densities are pronounced above T=1.0 MeV i.e., above critical temperature. After T=1.0 MeV, the neutron density decreases and the proton density increases in the interior of the nuclei. The decrease of the neutron density in the interior of the nuclei is directly linked to by the population of levels above the Fermi level, and depopulation of levels below (see Fig. 7.3), including the neutron

$3s_{1/2}$ state which contributes to the center of the nucleus. As a result, the neutron (proton) effective mass (m^*_q/m) at r=0 decreases (increases) after the critical temperature. The present results provide an accurate view of the temperature effects on the effective mass in nuclei. In order to provide a general trend for the behavior of the effective k-mass, we performed same calculations with other Skyrme interactions: SLy5, SIII and SkM* and also with other nuclei. The results reveal that the behavior of the effective k-mass depends on the interaction used and nuclei considered. The k-mass can either increase or decrease, however, the change is small and ranging between 0.15% and 1.1% from T=0 MeV to T=1.5 MeV. Although in most of the calculations temperature dependence of the k-mass is small and taken as constant at first order, our results show that the temperature dependence of the k-mass should not be ignored in the case of an accurate study of the total effective mass at high temperatures.

7.4 Summary

In summary, we have investigated the pairing properties of different nuclei within the finite temperature HF+BCS framework with Skyrme interactions. The relation between the critical temperature and the pairing gap value at zero temperature generally obeys the $T_c \cong 0.57\Delta_{T=0}$ equation, depending on the energy difference between the last occupied and first unoccupied states and the interaction used. The temperature dependence of the neutron skin is also investigated with different nuclei. A substantial increase in the proton and neutron radius of neutron rich nuclei is obtained above the critical temperatures. However for less-neutron rich nuclei, the increase in the proton radius cancels out the rapid increase of the neutron skin radius. The changes in the neutron skin is mainly due to the effect of temperature on the occupation probabilities of the single-particle states around the Fermi level. High temperature causes the occupation of the unoccupied levels which is leading an enhancement in the proton and neutron radius.

A correlation is obtained between the effective mass of Skyrme energy density functionals and the critical temperature of ^{120}Sn nucleus, relating $m*$, T$_c$ and $\Delta(T=0)$. It has been shown that with the enhancement in the effective mass, the level densities around the

Fermi level and pairing gap increase which eventually leads an increase in the critical temperature. However, this correlation depends on the pairing prescription. Temperature dependence of the effective k-masses of protons and neutrons are also investigated. Due to the changes in the proton and neutron densities, the effective nucleon masses show rather different fine behavior before and after the critical temperature, which is a new feature.

CHAPTER 8

EFFECT OF THE TEMPERATURE ON THE MULTIPOLE RESPONSE OF NUCLEI

As we already mentioned in the previous chapters, Giant Resonances are quite important in order to probe the properties of nuclei. Especially, formation of the low-lying dipole states is known as a property of neutron-rich nuclei which is related to the neutron skin and the symmetry energy of nuclei as well as the astrophysical processes which take place at finite temperature. Investigation of Giant Resonances under extreme conditions provides even more detailed information about the structure and properties of nuclei, and this brings further challenge for theory.

In the last decades, the GDR built on the excited states have been studied experimentally either using inelastic scattering of light particles or fusion-evaporation reactions [60–64] at excitation energies from 10 to 500 MeV and spins up to $J \approx 60$. In particular, several works have been devoted to investigate the GDR properties as a function of excitation energy and the spin of the nuclei [168]. It is known that the GDR properties depend on the angular momentum of the states as well as the excitation energy or temperature. The width of the GDR is not sensitive to the angular momentum of the states up to $35\hbar$. However, it is sensitive to the temperature effects and it increases with increasing temperature [169]. The reason of the increase in the GDR width is not obvious. It can be related either to the change of the nuclear potential with the temperature or the thermal damping of nucleons. On the theoretical side, several works have already been devoted to the calculation of the nuclear excited states at finite temperature. The first application of the finite temperature RPA was performed in Ref. [69] for the ^{40}Ca nucleus. It was shown that the low-energy part of the Giant Quadrupole response was sensitive to the temperature due to the p-p and h-h excitations. However, the Giant Dipole response of nuclei remained almost the same with increasing temperature. The finite temperature QRPA equations have been derived in Refs. [70,71]. Furthermore, different theoretical models: the extended TDHF [65,66], the Phonon Damping Model [67] and the quasiparticle-phonon model [68] have been applied in order to study the temperature effects on the multipole response of nuclei. However, calculations within the fully self-consistent RPA at finite temperature are still lacking. Additional works are needed in this field in order to clarify the nature and response of nuclei at finite temperatures.

In figure 8.1, we display the occupation probabilities of the states with respect to the single-particle energies of the ^{40}Ca nucleus at T=2 MeV in order to explain the underlying mechanism of the excitations at finite temperature. The single-particle levels are chosen around the Fermi level, because they are impacted by temperature. With the increase of the temperature, nucleons are excited to higher energies and occupation probabilities above the Fermi level are increased. Consequently, the Fermi surface becomes smooth. While we only have particle-hole (p-h) transitions at T=0, particle-particle (p-p) and hole-hole (h-h) transitions also become possible by increasing the temperature as can be seen from Fig. 8.1.

In the last part of this thesis, we aim at exploring the effects of the temperature on the multipole response (0^+, 1^-) of nuclei. In particular, the effect of the temperature on the low-energy modes of the selected nuclei are investigated within this framework. Firstly, the Finite Temperature Hartree-Fock calculations (FT-HF) are performed for obtaining the ground state properties of nuclei. Then, the Finite Temperature Random Phase Approximation (FT-RPA) is performed on top of the FT-HF calculations. In the present analysis, all calculations are performed self-consistently, namely, both the FT-HF equations and the matrix equations of FT-RPA are based on the same energy density functional. The Skyrme type SGII [103] interaction is used in the calculations. Calculations are also performed with the Skyrme SLy5 [108] interaction in order to check the reliability of the results. We work on closed-shell nuclei and the spherical symmetry is assumed. The continuum is discretized with the box boundary conditions, using a 20 fm box with a 0.1 fm mesh

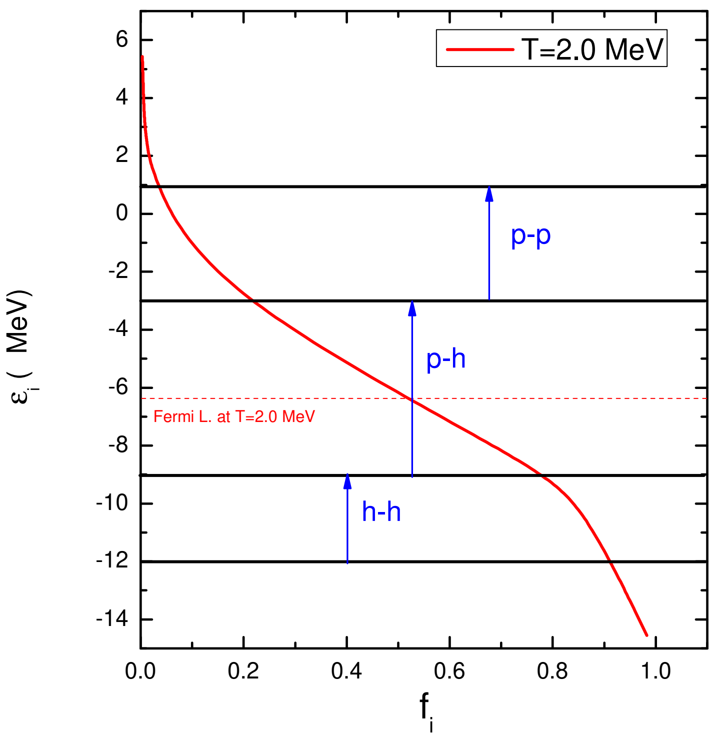

Figure 8.1 The occupation probabilities of the states as a function of the single-particle energies of ^{40}Ca nucleus at T=2 MeV. At finite temperatures, the p-p and h-h transitions also become possible as well as p-h transitions.

size and E_{cut}=100 MeV. The results for the strength functions are smeared out by using Lorentzian functions with a width of 1 MeV.

8.1 Finite Temperature RPA Equations

The derivation of the FT-RPA equations are similar to the RPA. To evaluate the Equation-of-Motion, we need the HF expectation values of the commutators of the single-particle operators. At finite temperature, the single-particle matrix reads $\rho_{ij} = \langle c_j^\dagger c_i \rangle = \delta_{ij} f_i$ or $\langle c_j c_i^\dagger \rangle = \delta_{ij}(1 - f_j)$. If we solve the Equation-of-Motion at finite temperatures, the A and B matrices of the FT-RPA are given by

$$A_{abcd} \equiv \langle HF| \left[c_b^\dagger c_a, \left[H, c_c^\dagger c_d \right] \right] |HF\rangle = (\varepsilon_a - \varepsilon_b)\delta_{ac}\delta_{bd} + \overline{V}_{ad,bc} \times (f_d - f_c), \tag{8.1}$$

$$B_{abcd} \equiv -\langle HF| \left[c_b^\dagger c_a, \left[H, c_d^\dagger c_c \right] \right] |HF\rangle = \overline{V}_{ac,bd} \times (f_d - f_c) \tag{8.2}$$

where f_i is the temperature dependent Fermi-Dirac distribution function:

$$f_i = [1 + exp(\varepsilon_i - \lambda)/k_B T]^{-1}. \tag{8.3}$$

Here, ε_i and λ represent the single-particle energies and the Fermi energy, respectively. As in the RPA case, the normalization condition for the FT-RPA is given by

$$\sum_{ab} (X^{\nu}_{ab} X^{\nu'}_{ab} - Y^{\nu}_{ab} Y^{\nu'}_{ab}) \times (f_b - f_a) = \delta_{\nu\nu'}. \tag{8.4}$$

Using the RPA forward and backward amplitudes, the transition strength is calculated as

$$B(J, E_\nu) = \left| \sum_{ab} (X^{\nu}_{ab} + Y^{\nu}_{ab}) \times \langle a || F_J || b \rangle \times (f_b - f_a) \right|^2 . \tag{8.5}$$

At the zero temperature limit, the FT-RPA equations becomes the well-known RPA equations.

8.2 The Dipole Spectrum of Nuclei at Finite Temperature

In this part, we investigate the effect of the temperature on the dipole response of nuclei from medium-heavy (^{48}Ca, ^{56}Ni) to heavy nuclei (^{132}Sn and ^{208}Pb). In Figure 8.2, we present the FT-RPA strength distributions in ^{48}Ca, ^{56}Ni, ^{132}Sn and ^{208}Pb nuclei for the isovector dipole operator, at temperatures T = 0, 1.0 and 2.0 MeV. The Giant Dipole Resonance exhibits strong peaks at the high-energy part of the spectrum of each nucleus as expected. At T=0 MeV, the GDR centroid energies of the ^{48}Ca, ^{56}Ni, ^{132}Sn and ^{208}Pb nuclei are found as 19.2 MeV, 19.2 MeV, 15.4 MeV and 13.7 MeV, respectively. Then, we perform the FT-RPA at T=1.0 and 2.0 MeV, respectively. In particular, the effect of the temperature is pronounced above T=1.0 MeV in each nucleus. All the nuclei considered exhibit similar behavior with the increase in the temperature: The GDR centroid energies are shifted slightly to the lower energies while the strength and width remain almost the same. At T=2.0 MeV, the GDR centroid energies of the ^{48}Ca, ^{56}Ni, ^{132}Sn and ^{208}Pb change to 18.4 MeV, 18.1 MeV, 14.8 MeV and 13.4 MeV, respectively. While the centroid energies of ^{48}Ca, ^{56}Ni nuclei change by about 1.0 MeV at T=2.0 MeV, the change becomes smaller in heavy nuclei ^{132}Sn and ^{208}Pb. This behavior can be explained by the shell properties of nuclei. Due to the strong shell effects of ^{208}Pb, the nucleus preserves its spherical shape and limits the thermal population of the states above the Fermi level. Consequently, the effect of the temperature is limited on the strength function and the width of the excitation.

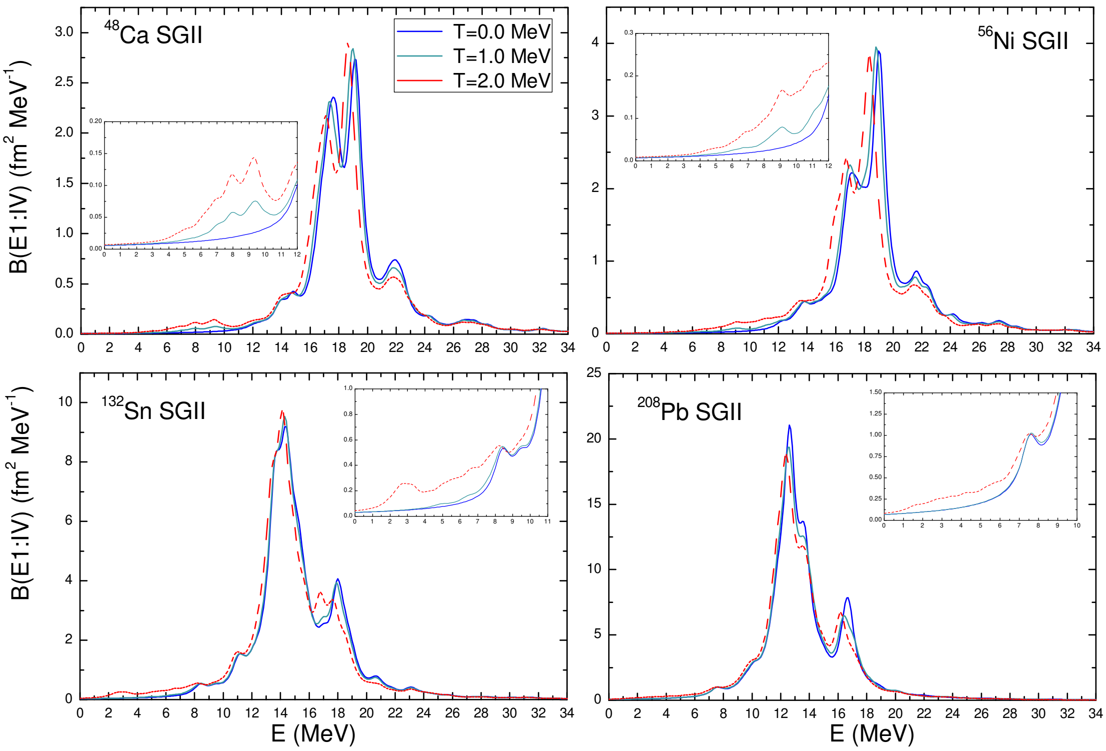

Figure 8.2 Isovector dipole transition strength distributions in in ^{48}Ca, ^{56}Ni, ^{132}Sn and ^{208}Pb nuclei using the FT-RPA and Skyrme type SGII interaction. The calculations are performed at T=0, 1.0 and 2.0 MeV. The low-energy part of the spectrum is also presented in the insertions.

In the insertions of Figure 8.2, we also focus on the low-energy part of the spectrum. With the increase of the temperature, the formation of the new low-energy states are obtained in each nucleus. Especially, the effect of the temperature is pronounced in the low-energy part of the neutron-rich medium-heavy nuclei. The formation of these low-energy states can be explained by the effect of the temperature on the shell structure of nuclei. At finite temperatures, the nucleons obey the temperature dependent Fermi-Dirac distribution function and spin pair correlations are destroyed. As a result, the Fermi surface become smoother due to the increased temperature. Especially, in neutron-rich nuclei, the neutrons becomes loosely bound with the temperature, additional transitions (p-p and h-h) become possible (see Fig. 8.1) and the new low-energy states appears. The results are also consistent with a recent work performed within the self-consistent relativistic FT-RPA framework [72]. In Table 8.1, we present the transitions of the selected low-energy states of ^{48}Ca and ^{132}Sn nuclei at T=2.0 MeV. In the last column, their transition amplitudes and the nature of the excitations are also presented. As it can be seen from Table 8.1, the contributions for the low-energy part mainly come from the neutron p-p excitation. Due to their large valence space, the p-p excitations have more contribution to the low-energy states of the excitations when compared with the h-h excitations. In addition, the low-energy part of the spectrum occurs mainly due to the single-particle excitations. i.e., they do not show a collective behavior as in the case of the GDR region. The calculations are also performed with the Skyrme SLy5 interaction and similar results are obtained.

Table 8.1 FT-RPA transitions at T=2.0 MeV for ^{48}Ca and ^{132}Sn nuclei. The percentage of the transition amplitudes and the nature of the excitation are presented in the third column of the table.

E (MeV)	Transition	% (type of excitation)
^{48}Ca		
6.06	$n2d_{3/2} \rightarrow n2p_{1/2}$	99.8 (p-p)
6.93	$n3s_{1/2} \rightarrow n2p_{3/2}$	98.2 (p-p)
7.81	$n2d_{5/2} \rightarrow n2p_{3/2}$	98.4 (p-p)
9.3	$n3d_{5/2} \rightarrow n2p_{3/2}$	88.5 (p-p)
	$n3d_{3/2} \rightarrow n1f_{5/2}$	3.5 (p-p)
^{132}Sn		
6.52	$n2g_{9/2} \rightarrow n2f_{7/2}$	98.9 (p-p)
6.84	$n3g_{7/2} \rightarrow n2f_{5/2}$	99.3 (p-p)
7.6	$n4d_{5/2} \rightarrow n2f_{7/2}$	95.6 (p-p)
8.05	$n3g_{9/2} \rightarrow n2f_{7/2}$	90.5 (p-p)
	$n3p_{3/2} \rightarrow n2d_{3/2}$	3.84 (p-p)

8.3 The Monopole Spectrum of Nuclei at Finite Temperature

In this part, we investigate the effect of the temperature on the isoscalar monopole response of nuclei. In Figure 8.3, we display the strength function of the isoscalar Giant Monopole Resonance for ^{48}Ca, ^{56}Ni, ^{132}Sn and ^{208}Pb nuclei at T=0, 1.0 and 2.0 MeV. As it can be seen from Fig. 8.3, the ISGMR strengths and energies almost do not change with the temperature. However, the temperature affects the low-energy part of the monopole response considerably, namely, new low-energy states appear. As in the case of the low-energy dipole spectrum, the low-energy isoscalar monopole part of the spectrum is not collective, i.e., almost all excitations come from the proton or neutron p-p single-particle excitations.

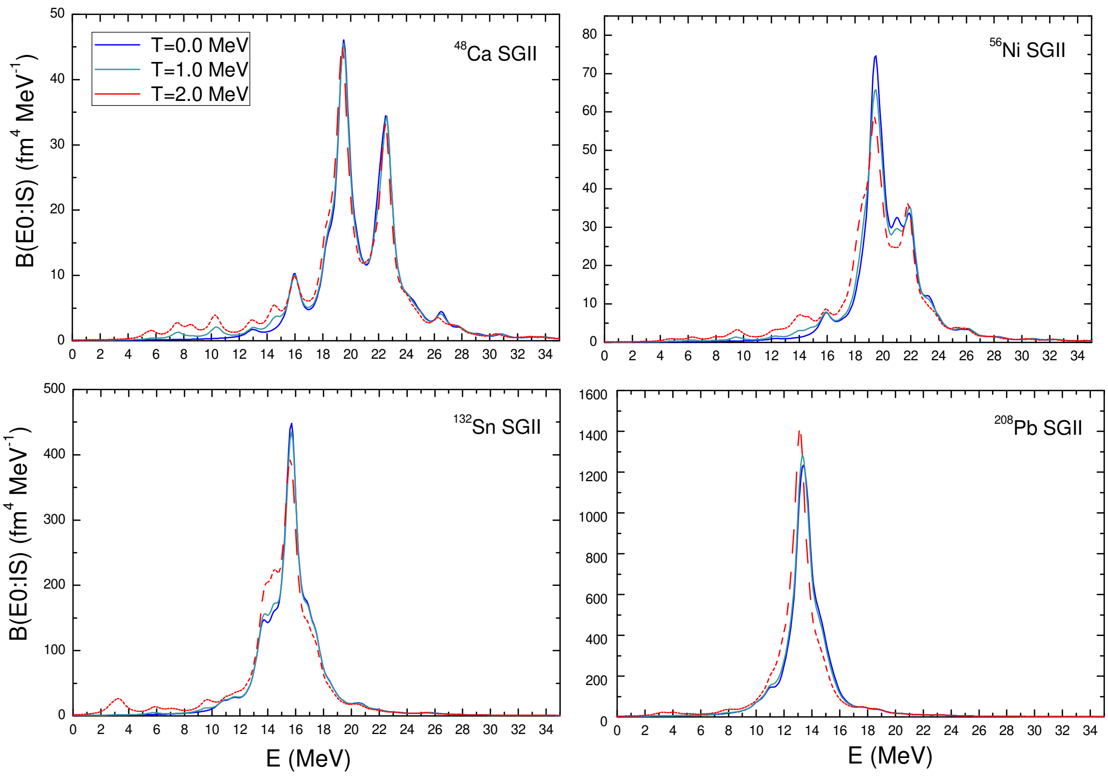

Figure 8.3 Same as in Fig. 8.2 but for the isoscalar monopole transition strength distributions.

In Figure 8.4, we also present the change of the averaged energies of the ^{48}Ca and ^{132}Sn nuclei with respect to the temperature. The average energies of nuclei decrease with increasing temperature. As it is mentioned in Chapter 2, the centroid energies of the ISGMR are used in the determination of the nuclear incompressibility. So, it could be important to know the temperature dependence of the centroid energies of the ISGMR in order to obtain the information about the incompressibility of nuclear matter at finite temperatures.

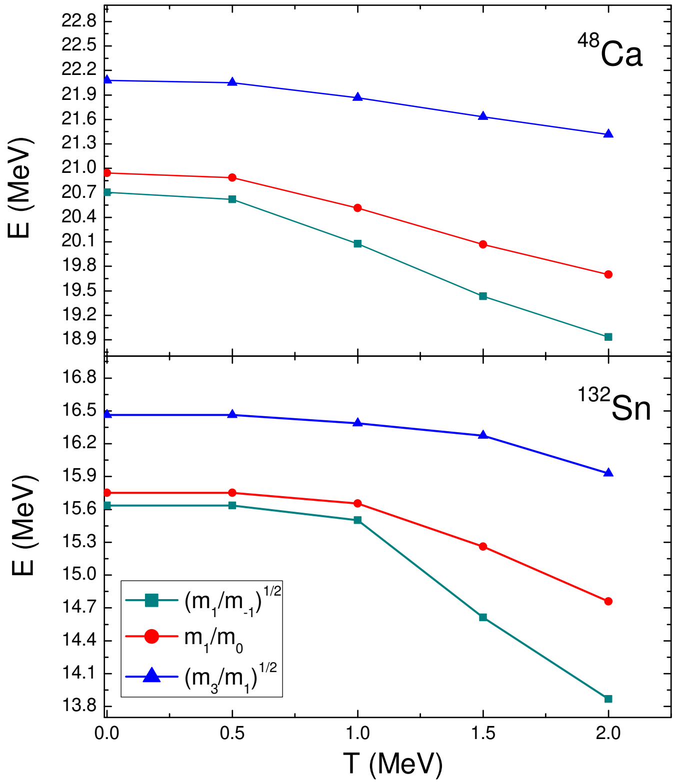

Figure 8.4 Averaged energies of the ^{48}Ca and ^{132}Sn nuclei with respect to the temperature.

8.4 The First Application of the FT-QRPA

In this section, we perform the fully self-consistent FT-QRPA in order to calculate the multipole response of the open-shell nucleus ^{120}Sn. Detailed derivations of the FT-QRPA equations are provided in Appendix D. In the calculations, we use Skyrme SLy5 interaction and the pairing strength (V_0=650.0 $MeV.fm^3$) is adjusted according to the $12/\sqrt{A}$ empirical rule. The spherical symmetry is assumed in all calculations. The continuum is discretized with the box boundary conditions, using a 20 fm box with a 0.1 fm mesh size and E_{cut}=100 MeV. The preliminary results are presented for the monopole and dipole responses of ^{120}Sn. Figure 8.5 displays the monopole response for ^{120}Sn at T=0, 1.0, 1.5

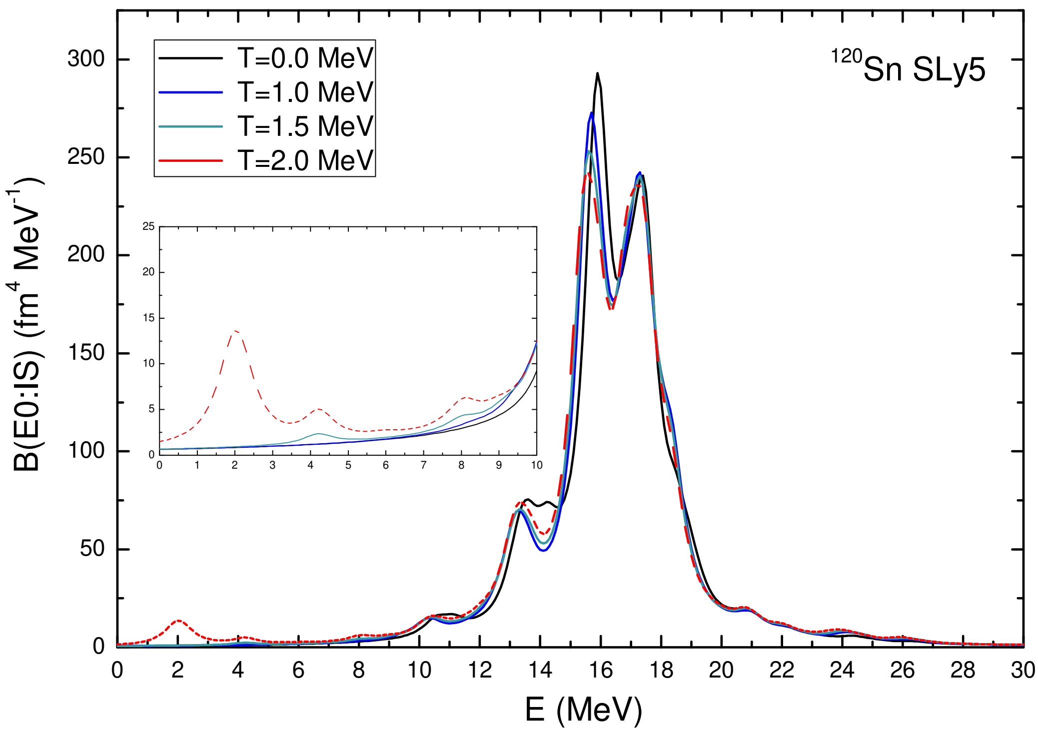

Figure 8.5 Isoscalar monopole transition strength distributions in ^{120}Sn using the FT-QRPA and Skyrme type SLy5 interaction. The calculations are performed at T=0, 1.0, 1.5 and 2.0 MeV. The low-energy part of the spectrum is also presented in the insertion.

and 2.0 MeV. The position and the width of the GMR are practically unchanged with the increase in temperature. In addition, the effect of the temperature is not pronounced until T=2.0 MeV. The new low-energy excitations occur with increasing temperature due to the thermally excited nucleons above the Fermi level. It should be noted that similar results are also obtained in the monopole excitations of the closed-shell nuclei with the FT-RPA. In Figure 8.6, we present the QRPA (T=0 MeV), FT-RPA and FT-QRPA results at T=2.0 MeV in order to see the effects of the pairing correlations on the monopole excitations of ^{120}Sn. As it can be seen from Figure 8.6, the FT-RPA and FT-QRPA results are almost the same in the GMR case. In the low-energy part, at around $E \approx 2.0$ MeV, the strength function decreases slightly in the FT-QRPA due to the pairing effects in the residual interaction. The averaged energies (m_1/m_0) for ^{120}Sn using the QRPA, FT-RPA and FT-QRPA at T=2.0 MeV are 16.5 MeV, 15.7 MeV and 16.1 MeV, respectively. While the averaged energy decreases by about 0.4 MeV in the FT-QRPA, nand by around 0.8 MeV in the FT-RPA.

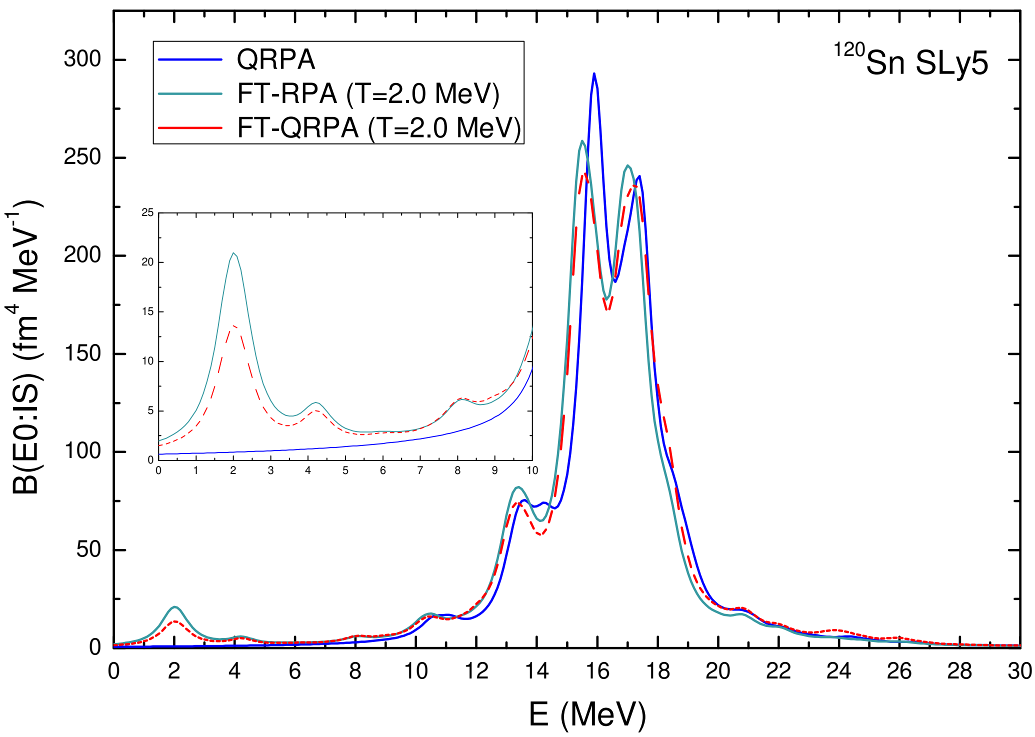

Figure 8.6 Isoscalar monopole transition strength distributions of ^{120}Sn using the QRPA at T=0 MeV, the FT-RPA and FT-QRPA at T=2.0 MeV. Skyrme type SLy5 interaction is used in the calculations. The low-energy part of the spectrum is also presented in the insertion.

Figure 8.7 illustrates the evolution of the dipole response of ^{120}Sn with respect to the temperature. Since the data are experimentally accessible along the isotopic chain, the tin isotopic chain is of special interest. Recently, the low-energy dipole mode was observed at 8.3 MeV for ^{120}Sn nucleus in a (γ,γ') experiment where the total strength corresponds to 2.3(2) of EWSR [170]. In Figure 8.7, the low-energy dipole mode is found at 8.71 MeV and it exhausts 0.59% of EWSR at zero temperature. The calculated PDR excitation energy and strength decrease slightly with increasing temperature. The PDR is obtained at 8.45 MeV and exhausts 0.17% of EWSR at T=2.0 MeV. In addition, it shows a collective behavior, namely, several p-h, p-p and h-h excitations are feeding this state. However, the contribution of the p-p and h-h excitations to the strength function is rather low for this state (less than 2%). The smaller strength in the PDR region shows that the p-h, p-p and h-h pairs interfere destructively. In addition, new low-energy single-particle transitions appear below E=8.0 MeV with increasing temperature, due to p-p and h-h excitations.

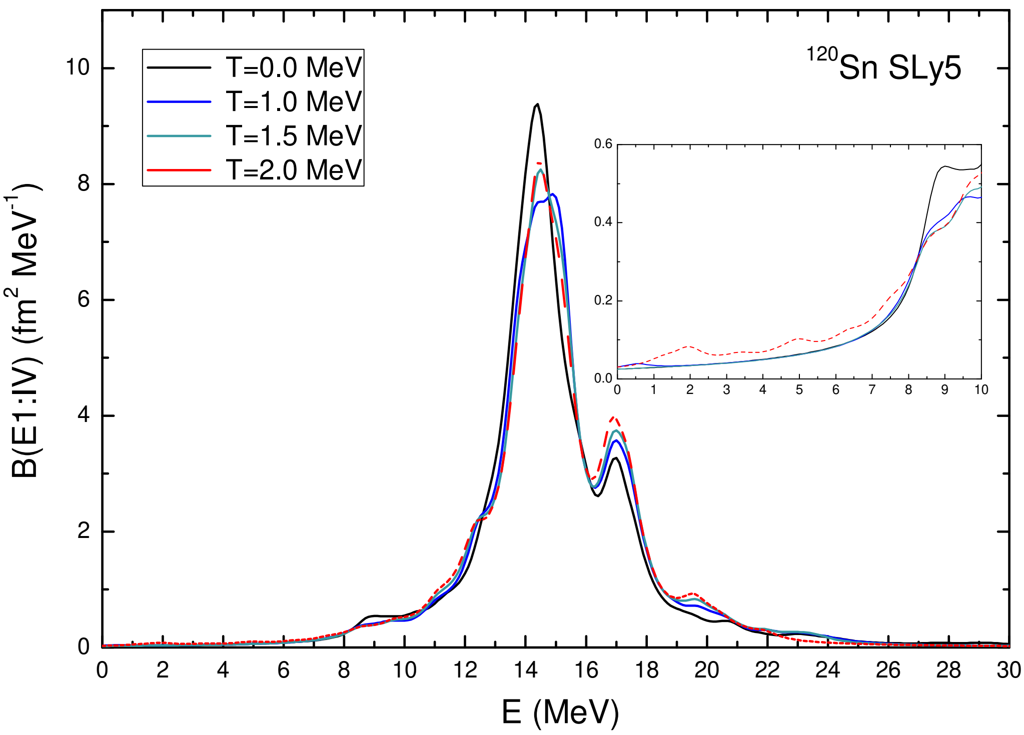

Figure 8.7 Same as in Figure 8.5 but for the isovector dipole transition strength distribution.

Finally, In Figure 8.8, we present the FT-RPA and FT-QRPA results of ^{120}Sn at T=2 MeV. As in the case of the monopole case, the FT-QRPA strength function slightly changes in the low-energy part of the spectrum at around 2.0 MeV. The averaged energies for ^{120}Sn using the QRPA, FT-RPA and FT-QRPA at T=2.0 MeV are 15.1 MeV, 14.9 MeV and

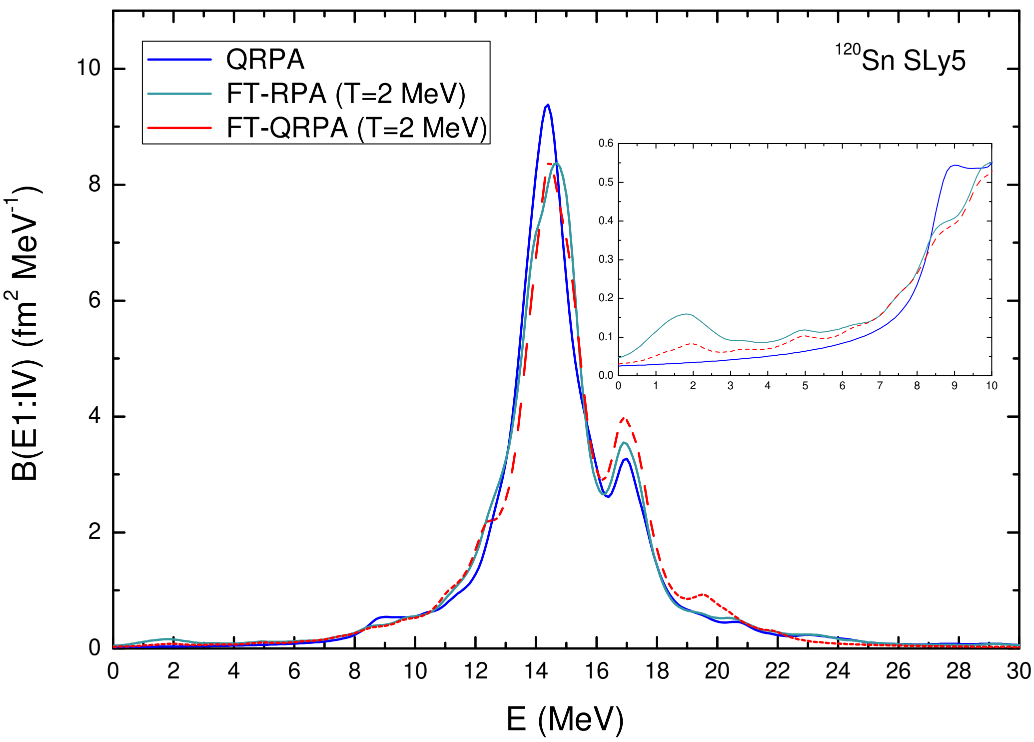

Figure 8.8 Same as in Figure 8.6 but for the isovector dipole transition strength distribution.

15.2 MeV, respectively. While the averaged energy decreases by about 0.2 MeV in the FT-RPA, it increases slightly in the FT-QRPA.

CHAPTER 9

RESULTS AND DISCUSSION

"An expert is a person who has made all the mistakes that can be made in a very narrow field."

Niels Bohr, 1885-1962

Today, the self-consistent mean-field models are the best tools in the description of the static and dynamic properties of nuclei over the entire nuclear chart. Since it becomes possible to reach the nuclei through the drip lines with the advances in the experimental facilities, investigation of the properties and dynamics of the nuclei under extreme conditions of isospin and temperature is quite essential to improve the energy density functionals. Within the framework of this work, the static and dynamic properties of the nuclei are undertaken under extreme conditions of isospin and temperature.

In the first part of this thesis, we focused on the static and dynamic properties of nuclei at zero temperature. Firstly, the low-energy dipole and monopole excitations of the closed-shell nuclei have been investigated with the Skyrme Hartree-Fock Random Phase Approximation. The behavior and nature of the low-energy dipole modes have been clarified using the transition densities and collectivity of the excited states. Analyzing the transition densities, it was shown that the behavior of the low-energy dipole modes is quite different from that of the high-energy part of the excitations. The proton and neutron transition densities display a rather complex character inside and outside the nuclei: both the isoscalar and isovector motions can be observed. The collectivity analysis shows that the low-energy dipole modes are formed mainly from several particle-hole excitations and have a non-negligible collectivity. Similar results are also obtained in the case of the low-energy monopole excitations. While the proton and neutron transition densities show a complex pattern as in the case of the low-energy dipole modes, it has been shown that the low-energy monopole modes are formed by the pure single particle-hole excitations and do not show a collective character. We conclude that the non-collective character of the low-energy monopole modes can be used in order to probe the shell structure of nuclei due to its specific $L = 0$ multipolarity. A good agreement has been obtained with the low-energy monopole excitation energies and the spin-orbit splittings of doubly magic ^{132}Sn and ^{208}Pb nuclei. It should be noted that the proper continuum treatment is an important factor in the determination and interpretation of the configurations of the single-particle excitations in the low-energy part of the excitations. Using the exact continuum treatment, the interpretation for the low energy monopole is changed, hindering the LS measurement. However, the proper continuum treatment does not change the results quantitatively. The low-energy monopole strength has also been predicted with and without proper continuum treatment and measurements of the low-energy GMR are still necessary. The measurement of giant resonances in exotic nuclei is still a challenge in the experimental part. Additional works are needed in this field to clarify the nature of the low-energy part of the excitations. In addition, the effects of pairing on the behavior of the dipole and monopole responses of nuclei remain as a future work in this field.

Additionally, the formation of new magic numbers in neutron-rich nuclei have been investigated within the HF-BCS and HFB approaches. The role of the tensor interaction has been studied on the single-particle evolution and the formation of the new shell gaps. In the non-relativistic framework, the tensor force is included in the interaction separately. We have worked with the well-known Skyrme SLy5 (without tensor) and Sly5+T (with tensor) interactions. It has been shown that tensor force affects the single-particle spectra considerably and leads to the vanishing of pairing correlations in some exotic nuclei. We confirm the magicity of $^{52-54}$Ca nuclei with the HF-BCS and HFB approximations. We have also investigated the First 2^+ states in the Ca isotopic chain, again with and without the tensor component in the Skyrme interaction. The tensor force leads to an increased energy of the first 2^+ state in the calcium isotopic chain. Both ^{52}Ca and ^{54}Ca show a magic nature. The results indicate the important role of the tensor interaction in the shell evolution of drip line nuclei. The results are also pointing out the deficiencies of the energy density functionals through the drip lines of the nuclear chart.

In the second part, we have used the FT-HFBCS in order to study the phase transitions, neutron skin and proton-neutron effective mass of nuclei around the stability line at finite temperatures. Apart from the critical temperature for the pairing phase transitions, the changes in the neutron skin and the proton-neutron effective mass of nuclei have also been discussed. The relation between the critical temperature and the pairing gap value at zero temperature generally obeys the $T_c \approx 0.57\Delta_{T=0}$ law, depending on the energy difference between the last occupied and first unoccupied states and the interaction used. Due to the thermal population of the states at finite temperatures, an increase in the neutron skin of the nuclei is obtained. Additionally, it has been shown that the temperature changes the proton-neutron effective mass slightly, and this can be important in the fine tuning of the energy density functionals at finite temperature. The development of the FT-HFBCS to the FT-HFB or investigations of the deformed systems at finite temperatures can be helpful, and remains as an extension of this work in the future.

The multipole response of the nuclei have been investigated using the fully self-consistent Finite temperature RPA. We have performed the fully self-consistent calculations on the closed shell nuclei at finite temperatures. It is shown that the high-energy part of the excitations changes slightly with the temperature. However, the low-energy part of the spectrum is rather sensitive to the temperature due to the thermal excitation of the nucleons above the Fermi level: new low-energy states appear with increasing temperature. In the last part of the thesis, the finite temperature QRPA calculations have been performed to investigate the monopole and dipole response of open-shell ^{120}Sn nucleus for the first time. By increasing the temperature, the new low-energy monopole states are also obtained in ^{120}Sn as in the case of the closed-shell nuclei. In the dipole case, the PDR energy and strength function decrease slightly with the increase in the temperature. Additionally, new low-energy dipole states appear below the PDR region which emerges mainly from p-p and h-h excitations.

APPENDIX A

REMARKS

A.1 The Quasiparticle Representation of the Hamiltonian

The Hamiltonian is defined in particle basis as [11, 12] :

$$H = \sum_{ab} T_{ab} c_a^\dagger c_b + \frac{1}{4} \sum_{abcd} v_{abcd} c_a^\dagger c_b^\dagger c_d c_c \tag{A.1}$$

here, T represents the kinetic energy and the v_{abcd} are antisymmetrized matrix elements of the nuclear interaction. The transformation from particles to quasiparticles is performed through

$$c_a^\dagger = u_a a_a^\dagger - v_a \tilde{a}_a \tag{A.2}$$

$$\tilde{c}_a = u_a a_a - v_a \tilde{a}_a^\dagger \tag{A.3}$$

and we obtain the Hamiltonian as

$$H = H_0 + \sum_b H_{11}(b)[a_b^\dagger \tilde{a}_b] + \sum_b H_{20}(b)([a_b^\dagger a_b^\dagger] - [\tilde{a}_b \tilde{a}_b]) + V_{RES} \tag{A.4}$$

The residual interaction is given in compact form as

$$V_{RES} = \frac{1}{4} \sum_{abcd} \bar{v}_{abcd} N \left[c_a^\dagger c_b^\dagger c_d c_c \right] \tag{A.5}$$

where $N[\ldots]$BCS denotes normal ordering with respect to the BCS vacuum ($|BCS\rangle$). Expressing the residual interaction in terms of the quasiparticle creation and annihilation operators, V_{RES} is written as

$$V_{RES} = H_{40} + H_{31} + H_{22} \tag{A.6}$$

where

$$H_{40} = \sum_{abcd} \bar{v}_{abcd} \left[\frac{1}{4} u_a u_b v_c v_d (: a_a^\dagger a_b^\dagger \tilde{a}_d^\dagger \tilde{a}_c^\dagger : + H.c.) \right] \tag{A.7}$$

$$H_{31} = \sum_{abcd} \bar{v}_{abcd} \left[-\frac{1}{2} (u_a u_b u_c v_d - v_a v_b v_c u_d)(: a_a^\dagger a_b^\dagger \tilde{a}_d^\dagger a_c : + H.c.) \right] \tag{A.8}$$

$$H_{22} = \sum_{abcd} \bar{v}_{abcd} \left[\frac{1}{4} (u_a u_b u_c u_d + v_a v_b v_c v_d) : a_a^\dagger a_b^\dagger a_d a_c : - u_a v_b u_c v_d : a_a^\dagger \tilde{a}_d^\dagger \tilde{a}_b a_c : \right] \tag{A.9}$$

Also, we can express H_{40}, H_{22} and H_{31} in angular-momentum-coupled form,

$$H_{40} = \frac{1}{2} \sum_{abcdJ} (-)^J V_{abcd}^{40}(J) \left(: A_{ab}^\dagger(J) A_{cd}^\dagger(J) : + : A_{cd}(J) A_{ab}(J) : \right) \tag{A.10}$$

$$H_{22} = \frac{1}{2} \sum_{abcdJ} (-)^J V_{abcd}^{22}(J) : A_{ab}^\dagger(J) A_{\tilde{c}\tilde{d}}(J) : \tag{A.11}$$

$$H_{31} = \sum_{abcdJ} (-)^J V_{abcd}^{31}(J) \left(: A_{ab}^\dagger(J) B_{cd}^\dagger(J) : + : B_{cd}(J) A_{ab}(J) : \right) \tag{A.12}$$

and the matrix elements are

$$V_{abcd}^{40}(J) = (u_a u_b v_c v_d) G(abcdJ) \tag{A.13}$$

$$V_{abcd}^{22}(J) = (u_a u_b u_c u_d + v_a v_b v_c v_d) G(abcdJ) + 4 u_a v_b u_c v_d F(abcdJ) \tag{A.14}$$

$$V_{abcd}^{31}(J) = (u_a u_b v_c u_d - v_a v_b u_c v_d) G(abcdJ) \tag{A.15}$$

with

$$G(abcdJ) = -\frac{1}{2} \sqrt{1 + (-)^J \delta_{ab}} \sqrt{1 + (-)^J \delta_{cd}} \langle ab; J | V | cd; J \rangle \tag{A.16}$$

$$F(abcdJ) = -\frac{1}{2} \left\langle ab^{-1}; J | V | cd^{-1}; J \right\rangle \tag{A.17}$$

A.2 The Wigner-Eckart Theorem

According to the Wigner−Eckart theorem, it is possible to factorize out the projection quantum number dependence in the matrix element. For example, consider a matrix element $\langle j'm' | F_{JM} | jm \rangle$ where F_{JM} is an operator and (j, m) angular momentum j and its z projection m of single-particle states. As we mentioned above, we can write the matrix element as

$$\langle j'm'|F_{JM}|jm\rangle = C(jLj', mMm')\langle j'||F_{JM}||j\rangle \tag{A.18}$$

where the projection number dependence of the matrix is given by the $C(jLj', mMm')$ geometrical factor which is known as the Clebsh-Gordon coefficient. In addition, $\langle j'||F_{JM}||j\rangle$ is called the reduced matrix element.

APPENDIX B

FIXING THE CHEMICAL POTENTIAL

In this part, we explain the treatment of the chemical potential at finite temperature when dealing with the particle number conservation in the Hartree Fock-BCS calculations. In order to calculate the chemical potential, we perform $\lambda = \lambda_0 - \delta\lambda$ and $\delta\lambda = \delta N/(\partial N/\partial\lambda)$. At finite temperatures the particle number is calculated as

$$N = \sum_j (2j+1)\left[v_j^2(1-f_j) + u_j^2 f_j\right] \tag{B.1}$$

where f_j is the temperature dependent Fermi-Dirac function and $u_j^2 = 1 - v_j^2$ Then,

$$N = \sum_j (2j+1)\left[v_j^2(1-2f_j) + f_j\right] \tag{B.2}$$

The derivative of the particle number with respect to the chemical potential is

$$\begin{aligned} \frac{\partial N}{\partial\lambda} &= \sum_j (2j+1)\left[\frac{\partial v_j^2}{\partial\lambda}(1-2f_j) + 2v_j^2\frac{\partial f_j}{\partial\lambda} + \frac{\partial f_j}{\partial\lambda}\right] \\ &= \sum_j (2j+1)\left[\frac{\partial v_j^2}{\partial\lambda}(1-2f_j) + (1-2v_j^2)\frac{\partial f_j}{\partial\lambda}\right] \end{aligned} \tag{B.3}$$

Here, the derivative of v_j^2 (see Eq. 3.49) with respect to the chemical potential is

$$\begin{aligned} \frac{\partial v_j^2}{\partial\lambda} &= \frac{\partial}{\partial\lambda}\frac{1}{2}\left(1 - \frac{\varepsilon_j - \lambda}{E_j}\right) \\ &= -\frac{1}{2}\left(\frac{-E_j - (\varepsilon_j - \lambda)^2 - 1/E_j}{E_j^2}\right) = \frac{1}{2}\frac{\Delta_j^2}{E_j^3} \end{aligned} \tag{B.4}$$

and the derivative of the Fermi-Dirac function with respect to the chemical potential is

$$\begin{aligned}\frac{\partial f_j}{\partial \lambda} &= -(1+e^{\beta E_j})\frac{\partial}{\partial \lambda}e^{\beta E_j} \\ &= -f_j^2 e^{\beta E_j}\beta\frac{\partial E_j}{\partial \lambda} = f_j^2 e^{\beta E_j}\beta\frac{(\varepsilon_j - \lambda)}{E_j}\end{aligned} \tag{B.5}$$

where $\beta = 1/kT$, and k and T are the Boltzmann constant and temperature, respectively.

APPENDIX C

DERIVATION OF THE ELECTROMAGNETIC TRANSITIONS IN THE RPA

In this appendix, we give a detailed derivation of the reduced matrix element of the RPA. In angular momentum coupled scheme, the creation operator is written as

$$\Gamma_\nu^\dagger \left|RPA\right\rangle = \sum_{ab} X_{ab}^{\nu J} A_{ab}^\dagger(JM) - Y_{ab}^{\nu J} A_{ab}(\widetilde{JM}) \left|RPA\right\rangle . \tag{C.1}$$

where $A_{ab}^\dagger$ and $A_{ab}(\widetilde{JM})$ are the coupled p-h creation and destruction operators:

$$A_{ab}^\dagger(JM) = \sum_{m_a m_b} (-)^{j_b - m_b} \langle j_a m_a j_b - m_b \left| JM \right\rangle c_{j_a m_a}^\dagger c_{j_b m_b}, \tag{C.2}$$

$$A_{ab}(\widetilde{JM}) = \sum_{m_a m_b} (-)^{J+M+j_b-m_b} \langle j_a m_a j_b - m_b \left| J - M \right\rangle c_{j_b m_b}^\dagger c_{j_a m_a}. \tag{C.3}$$

Also, the RPA states satisfy $\left|\nu\right\rangle = \Gamma_\nu^\dagger \left|0\right\rangle$ and $\Gamma_\nu \left|0\right\rangle = 0$. We need the matrix elements of the one-body operator $\hat{F}_{\lambda\mu} = \sum_{cd} \langle c|F_{\lambda\mu}|d\rangle c_c^\dagger c_d$:

$$\langle j_f m_f | F_{\lambda\mu} | j_i m_i \rangle = \sum_{cd} \langle c|F_{\lambda\mu}|d\rangle \langle j_f m_f | c_c^\dagger c_d | j_i m_i \rangle \tag{C.4}$$

If we apply the Wigner$-$Eckart theorem, we obtain

$$\langle j_f m_f || F_\lambda || j_i m_i \rangle = \hat{\lambda}^{-1} \sum_{cd} \langle c||F_\lambda||d\rangle \langle j_f m_f || [c_c^\dagger c_d]_\lambda || j_i m_i \rangle \tag{C.5}$$

In order to find the reduced transition probability, we need to evaluate

$$\langle RPA|F_{\lambda\mu}|\nu\rangle = \langle RPA|[F_{\lambda\mu}, \Gamma_\nu^\dagger]|RPA\rangle \tag{C.6}$$

In the Quasi-Boson approximation, the RPA ground state can be replaced with the HF ground state as

$$\langle RPA|[F_{\lambda\mu},\Gamma_\nu^\dagger]|RPA\rangle \cong \langle HF|[F_{\lambda\mu},\Gamma_\nu^\dagger]|HF\rangle. \tag{C.7}$$

Using the definitions of the excitation operator and the one-body operator, the commutators give

$$\langle HF|[F_{\lambda\mu},A_{ab}^\dagger(JM)]|HF\rangle = \hat{\lambda}^{-1}\sum_{cd}\langle c||F_\lambda||d\rangle\delta_{\lambda,J}\delta_{\mu-M}(-)^{j_c+j_d+M+1}\delta_{bc}\delta_{ad}, \tag{C.8}$$

$$\langle HF|[F_{\lambda\mu},A_{ab}(\widetilde{JM})]|HF\rangle = \hat{\lambda}^{-1}\sum_{cd}\langle c||F_\lambda||d\rangle\delta_{\lambda,J}\delta_{\mu-M}(-)^{J+M+1}\delta_{ac}\delta_{db}. \tag{C.9}$$

If we sum up the two equations, we obtain

$$\langle RPA|F_{\lambda\mu}|\nu\rangle = \hat{\lambda}^{-1}\sum_{cd}\langle c||F_\lambda||d\rangle\delta_{\lambda,J}\delta_{\mu-M}\times[X_{dc}^\nu(-)^{j_c+j_d+M+1} - Y_{dc}^\nu(-)^{J+M+1}]. \tag{C.10}$$

After applying Wigner−Eckart theorem to the left hand side of the Eq. C.10,

$$\langle RPA||F_\lambda||\nu\rangle = \delta_{\lambda,J}\sum_{cd}\langle c||F_\lambda||d\rangle\times[X_{dc}^\nu(-)^{j_c+j_d+J+1} + Y_{dc}^\nu] \tag{C.11}$$

and recognizing the symmetry properties of matrices:

$$\langle d||F_\lambda||c\rangle = (-)^{j_c+j_d+J+1}\langle c||F_\lambda||d\rangle. \tag{C.12}$$

After arranging the equations, we have

$$\langle RPA||F_\lambda||\nu\rangle = \delta_{\lambda,J}\sum_{cd}[X_{cd}^\nu + Y_{cd}^\nu]\times\langle c||F_\lambda||d\rangle. \tag{C.13}$$

for the electromagnetic excitations. Then, the reduced transition probability can be calculated using

$$B(E\lambda:\nu\rightarrow 0_{g.s.}^+) = \left|\sum_{cd}[X_{cd}^\nu + Y_{cd}^\nu]\times\langle c||F_\lambda||d\rangle\right|^2. \tag{C.14}$$

C.1 Commutation Relations at Zero Temperature

In this section, we calculate some commutation relations which are used in the derivation of the QRPA equations. Firstly, we consider the expectation values of the commutators of

A_{ab} and $A^{\dagger}_{cd}$. Using the definitions in (3.89),

$$\begin{aligned}
&\langle BCS|[A_{ab}(JM), A^{\dagger}_{cd}(J'M')]|BCS\rangle \\
&= N_{ab}(J)N_{cd}(J) \sum_{\substack{m_a m_b \\ m_c m_d}} \langle j_a m_a j_b m_b\,|JM\rangle\,\langle j_c m_c j_d m_d\,|JM\rangle\,\langle [a_b a_a, a^{\dagger}_c a^{\dagger}_d]\rangle
\end{aligned} \tag{C.15}$$

where N is a normalization factor and defined as

$$N_{ab} = \frac{\sqrt{1+\delta_{ab}(-)^J}}{1+\delta_{ab}}. \tag{C.16}$$

We proceed with the expectation values of the commutators of the quasiparticle operators:

$$\begin{aligned}
\langle [a_b a_a, a^{\dagger}_c a^{\dagger}_d]\rangle &= \langle a_b a_a a^{\dagger}_c a^{\dagger}_d\rangle - \langle a^{\dagger}_c a^{\dagger}_d a_b a_a\rangle \\
&= \langle a_b a^{\dagger}_d\rangle \delta_{ac} - \langle a_a a^{\dagger}_d\rangle \delta_{bc} + \langle a^{\dagger}_c a_b\rangle \delta_{ad} - \langle a^{\dagger}_c a_a\rangle \delta_{bd} \\
&= \delta_{ac}\delta_{bd} - \delta_{ad}\delta_{bc}.
\end{aligned} \tag{C.17}$$

In angular momentum coupled form:

$$\begin{aligned}
&\langle BCS|[A_{ab}(JM), A^{\dagger}_{cd}(J'M')]|BCS\rangle \\
&= N_{ab}(J)N_{cd}(J) \sum_{\substack{m_a m_b \\ m_c m_d}} \langle j_a m_a j_b m_b|JM\rangle\langle j_c m_c j_d m_d|JM\rangle(\delta_{ac}\delta_{bd} - \delta_{ad}\delta_{bc}).
\end{aligned} \tag{C.18}$$

Finally, we have

$$\begin{aligned}
&\langle BCS|[A_{ab}(JM), A^{\dagger}_{cd}(J'M')]|BCS\rangle \\
&= N_{ab}(J)^2 \delta_{JJ'}\delta_{MM'}[\delta_{ac}\delta_{bd} - (-1)^{j_a+j_b+J}\delta_{ad}\delta_{bc}].
\end{aligned} \tag{C.19}$$

C.2 Derivation of the Electromagnetic Transitions in the QRPA

In the QRPA case, the electromagnetic transitions are defined as

$$\langle QRPA||F_\lambda||\nu\rangle = \sum_{cd}\langle c||F_\lambda||d\rangle\langle QRPA||[c^{\dagger}_c\tilde{c}_d],\Gamma^{\dagger}_\nu||QRPA\rangle. \tag{C.20}$$

In order to evaluate the right hand side of the equation, we should express the single-particle operators in terms of the quasiparticle operators using the definition in Eq.A.2:

$$[c_c^\dagger \tilde{c}_d^\dagger]_{\lambda\mu} = \left\langle j_c m_c j_d m_d | _{\lambda\mu} \right\rangle c_c^\dagger \tilde{c}_d$$
$$= \left\langle j_c m_c j_d m_d | _{\lambda\mu} \right\rangle (u_c a_c^\dagger - v_c \tilde{a}_c)(u_d \tilde{a}_d + v_d a_d^\dagger) \quad \text{(C.21)}$$
$$= u_c u_d [a_c^\dagger \tilde{a}_d]_{\lambda\mu} + u_c v_d [a_c^\dagger a_d^\dagger]_{\lambda\mu} - v_c u_d [\tilde{a}_c \tilde{a}_d]_{\lambda\mu} - v_c v_d [\tilde{a}_c a_d^\dagger]_{\lambda\mu}.$$

In the QRPA, the excitation operator (see Eq. 3.89) is defined as

$$\Gamma_\nu^\dagger = \sum_{a \geq b} \left[X_{ab}^\nu A_{ab}^\dagger (JM) - Y_{ab}^\nu A_{ab}(\widetilde{JM}) \right]. \quad \text{(C.22)}$$

Now, we can evaluate the transition to the ground state as:

$$\langle QRPA || [c_c^\dagger \tilde{c}_d^\dagger], \Gamma_\nu^\dagger || QRPA \rangle$$
$$= N_{cd}^{-1}(J) \sum_{a \geq b} [v_c u_d X_{ab}^\nu \langle QRPA | [A_{cd}(\widetilde{JM}), A_{ab}^\dagger] | QRPA \rangle - u_c v_d Y_{ab}^\nu \langle QRPA | [A_{cd}^\dagger, A_{ab}(\widetilde{JM})] | QRPA \rangle]. \quad \text{(C.23)}$$

Using the QBA and performing the commutation relations, we obtain

$$\langle QRPA || [c_c^\dagger \tilde{c}_d^\dagger], \Gamma_\nu^\dagger || QRPA \rangle \cong \langle BCS || [c_c^\dagger \tilde{c}_d^\dagger], \Gamma_\nu^\dagger || BCS \rangle$$
$$\cong (-)^{J+M} \delta_{\lambda J} \delta_{\mu - M} N_{cd}(J) \times \sum_{a \geq b} (v_c u_d X_{ab}^\nu + u_c v_d Y_{ab}^\nu)[\delta_{ac}\delta_{bd} - (-)^{j_a + j_b + J} \delta_{ad}\delta_{bc}]. \quad \text{(C.24)}$$

Using Eq. C.24 in Eq. C.20 we obtain

$$\langle QRPA || F_\lambda || \nu \rangle = (-)^{J+M} \delta_{\lambda\mu J} \delta_{\mu - M} \hat{\lambda}^{-1} \sum_{a \geq b} N_{ab}(J) [\langle a || F_\lambda || b \rangle (v_a u_b X_{ab}^\nu + u_a v_b Y_{ab}^\nu)$$
$$- (-)^{j_a + j_b + J} \langle b || F_{JM} || a \rangle (v_b u_u X_{ab}^\nu + u_b v_a Y_{ab}^\nu)]. \quad \text{(C.25)}$$

After using the symmetry properties of the reduced matrix elements (see Eq. C.12), the Equation C.25 can be reduced to

$$\langle QRPA || F_{JM} || \nu \rangle = \sum_{a \geq b} N_{ab}(J) [\langle a || F_{JM} || b \rangle (v_a u_b + u_a v_b)(X_{ab}^\nu + Y_{ab}^\nu) \quad \text{(C.26)}$$

for the electromagnetic transitions. Finally, the reduced transition probability for the electromagnetic transtions can be calculated using

$$B(E\lambda : \nu \to 0^+_{g.s.}) = \left| \sum_{a \geq b} N_{ab}(J)[\langle a||F_{JM}||b\rangle (v_a u_b + u_a v_b)(X^{\nu}_{ab} + Y^{\nu}_{ab}) \right|^2 . \tag{C.27}$$

APPENDIX D

DERIVATION OF THE FINITE TEMPERATURE QRPA EQUATIONS

It is known that the RPA is suitable for calculating the nuclear excitations in closed shell nuclei. However, pairing correlations must be taken into account in the case of the open shell nuclei. If we go beyond closed shell nuclei, one should use the Random Phase Approximation (QRPA) in order to calculate nuclear excitations.

In this work, we investigate the effect of temperature on the multipole excitations of the nuclei. For this purpose, the well known QRPA is extended to Finite Temperature QRPA (FT-QRPA) in order to take into account the temperature effects. At finite temperature, we have both two-quasiparticle creation/destruction operators and one-quasiparticle creation/destruction operators.

In this section, we make the derivation of the finite temperature Quasiparticle Random Phase Approximation equations. The starting point in the Equation of Motion (EOM) method is the definition of a suitable excitation operator

$$\Gamma_\nu^\dagger = \sum_{a\geq b} X_{ab}^\nu A_{ab}^\dagger(JM) - Y_{ab}^\nu A_{ab}(\widetilde{JM}) + P_{ab}^\nu B_{ab}^\dagger(JM) - Q_{ab}^\nu B_{ab}(\widetilde{JM}) \tag{D.1}$$

here $\nu = nJ^\pi M$ and the summation is restricted to avoid double counting. The Hermitian of $\Gamma_\nu^\dagger$ is:

$$\Gamma_\nu = \sum_{a\geq b} X_{ab}^{\nu *} A_{ab}(JM) - Y_{ab}^{\nu *} A_{ab}^\dagger(\widetilde{JM}) + P_{ab}^{\nu *} B_{ab}(JM) - Q_{ab}^{\nu *} B_{ab}^\dagger(\widetilde{JM}). \tag{D.2}$$

We define the coupled operators as:

$$A^{\dagger}_{ab}(JM) = N_{ab}(J) \sum_{m_a m_b} \langle j_a m_a j_b m_b | JM \rangle a^{\dagger}_a a^{\dagger}_b, \tag{D.3}$$

$$A_{ab}(\widetilde{JM}) = N_{ab}(J)(-)^{J+M} \sum_{m_a m_b} \langle j_a m_a j_b m_b | J - M \rangle a_b a_a, \tag{D.4}$$

$$B^{\dagger}_{ab}(JM) = N_{ab}(J) \sum_{m_a m_b} (-)^{j_b - m_b} \langle j_a m_a j_b - m_b | JM \rangle a^{\dagger}_a a_b, \tag{D.5}$$

$$B_{ab}(\widetilde{JM}) = N_{ab}(J)(-)^{J+M} \sum_{m_a m_b} (-)^{j_b - m_b} \langle j_a m_a j_b - m_b | J - M \rangle a^{\dagger}_b a_a. \tag{D.6}$$

ahere $a^{\dagger}$ and a are the quasiparticle operators and N_{ab} is defined as

$$N_{ab}(J) = \frac{\sqrt{1 + (-)^J \delta_{ab}}}{1 + \delta_{ab}}. \tag{D.7}$$

Basic variations can be written as

$$\delta\Gamma = A_{ab}(JM)(B_{ab}(JM)), \qquad \delta\Gamma = A^{\dagger}_{ab}(\widetilde{JM})(B^{\dagger}_{ab}(\widetilde{JM})) \tag{D.8}$$

The calculations are still complicated since we do not know the ground state of $|QRPA\rangle$. If we assume that the correlated ground state does not differ very much from the BCS ground state, we can calculate all the expectation values in the BCS approximation. This approximation is known as the quasi-boson approximation. With $|BCS\rangle$ as the approximate vacuum the equation of motion can be written as:

$$\langle BCS| \left[\delta\Gamma, H, \Gamma^{\dagger}_{\nu}\right] |BCS\rangle = E_{\nu} \langle BCS| \left[\delta\Gamma, \Gamma^{\dagger}_{\nu}\right] |BCS\rangle \tag{D.9}$$

where H is the complete Hamiltonian expressed in terms of quasiparticle operators (See Appendix A) To evaluate the right-hand side of Eq. (D.9) we need the BCS expectation values of the commutators of the quasiparticle pair operators which are defined above. In QRPA, the ground state (vacuum) is defined by $a|BCS\rangle = 0$. However, it is not a vacuum at finite temperatures, i.e., $a|BCS\rangle \neq 0$. Furthermore, the single quasiparticle density matrix reads $\rho_{ij} = \langle a^{\dagger}_j a_i \rangle = \delta_{ij} f_i$ or $\langle a_j a^{\dagger}_i \rangle = \delta_{ij}(1 - f_j)$ where f_i is the Fermi-Dirac Distribution function defined as

$$f_i = [1 + exp(E_i/T)]^{-1}. \tag{D.10}$$

At zero temperature, f_i goes to zero and also $\rho_{ij} = 0$ represents the quasiparticle vacuum. With the increase of temperature, the importance of the Fermi-Dirac function increases. By using Eq. (D.9), the equations of the FT-QRPA are written as

$$\widetilde{A}_{abcd} = \left\langle \left[A_{ab}(JM), \left[H, A^{\dagger}_{cd}(JM) \right] \right] \right\rangle, \tag{D.11}$$

$$\widetilde{B}_{abcd} = -\left\langle \left[A_{ab}(JM), \left[H, A_{cd}(\widetilde{JM}) \right] \right] \right\rangle, \tag{D.12}$$

$$\widetilde{C}_{abcd} = \left\langle \left[B_{ab}(JM), \left[H, B^{\dagger}_{cd}(JM) \right] \right] \right\rangle, \tag{D.13}$$

$$\widetilde{D}_{abcd} = -\left\langle \left[B_{ab}(JM), \left[H, B_{cd}(\widetilde{JM}) \right] \right] \right\rangle, \tag{D.14}$$

$$\widetilde{a}_{abcd} = \left\langle \left[B_{ab}(JM), \left[H, A^{\dagger}_{cd}(JM) \right] \right] \right\rangle, \tag{D.15}$$

$$\widetilde{b}_{abcd} = -\left\langle \left[B_{ab}(JM), \left[H, A_{cd}(\widetilde{JM}) \right] \right] \right\rangle, \tag{D.16}$$

$$\widetilde{a}^{+}_{abcd} = \widetilde{a}^{T}_{abcd} = \left\langle \left[A_{ab}(JM), \left[H, B^{\dagger}_{cd}(JM) \right] \right] \right\rangle, \tag{D.17}$$

$$\widetilde{b}^{+}_{abcd} = \widetilde{b}^{T}_{abcd} = -\left\langle \left[A_{ab}(JM), \left[H, B_{cd}(\widetilde{JM}) \right] \right] \right\rangle. \tag{D.18}$$

The amplitudes $\widetilde{P}, \widetilde{X}, \widetilde{Y}$ and $\widetilde{Q}$ can be obtained using the following relations

$$\left\langle \left[a^{\dagger}_{b} a_{a}, \Gamma^{\dagger}_{\nu} \right] \right\rangle = (f_b - f_a) P_{ab}, \tag{D.19}$$

$$\left\langle \left[a_{b} a_{a}, \Gamma^{\dagger}_{\nu} \right] \right\rangle = (1 - f_a - f_b) X_{ab}, \tag{D.20}$$

$$\left\langle \left[a^{\dagger}_{a} a^{\dagger}_{b}, \Gamma^{\dagger}_{\nu} \right] \right\rangle = (1 - f_a - f_b) Y_{ab}, \tag{D.21}$$

$$\left\langle \left[a^{\dagger}_{a} a_{b}, \Gamma^{\dagger}_{\nu} \right] \right\rangle = (f_b - f_a) Q_{ab}. \tag{D.22}$$

The finite temperature QRPA equations can be combined into a single matrix as

$$\begin{pmatrix} \tilde{C} & \tilde{a} & \tilde{b} & \tilde{D} \\ \tilde{a}^{+} & \tilde{A} & \tilde{B} & \tilde{b}^{T} \\ -\tilde{b}^{+} & -\tilde{B}^{*} & -\tilde{A}^{*} & -\tilde{a}^{T} \\ -\tilde{D}^{*} & -\tilde{b}^{*} & -\tilde{a}^{*} & -\tilde{C}^{*} \end{pmatrix} \begin{pmatrix} \tilde{P} \\ \tilde{X} \\ \tilde{Y} \\ \tilde{Q} \end{pmatrix} = \hbar\omega \begin{pmatrix} \tilde{P} \\ \tilde{X} \\ \tilde{Y} \\ \tilde{Q} \end{pmatrix} \tag{D.23}$$

This is known as the Finite temperature QRPA matrix equation. Here, the matrices are defined as

$$\widetilde{A}_{abcd} = \sqrt{1 - f_a - f_b} A'_{abcd} \sqrt{1 - f_c - f_d} + (E_a + E_b)\delta_{ac}\delta_{bd}, \tag{D.24}$$

$$\widetilde{B}_{abcd} = \sqrt{1 - f_a - f_b} B_{abcd} \sqrt{1 - f_c - f_d}, \tag{D.25}$$

$$\widetilde{C}_{abcd} = \sqrt{f_b - f_a} C'_{abcd} \sqrt{f_d - f_c} + (E_a - E_b)\delta_{ac}\delta_{bd}, \tag{D.26}$$

$$\widetilde{D}_{abcd} = \sqrt{f_b - f_a} D_{abcd} \sqrt{f_d - f_c}, \tag{D.27}$$

$$\widetilde{a}_{abcd} = \sqrt{f_b - f_a} a_{abcd} \sqrt{1 - f_c - f_d}, \tag{D.28}$$

$$\widetilde{b}_{abcd} = \sqrt{f_b - f_a} b_{abcd} \sqrt{1 - f_c - f_d}, \tag{D.29}$$

$$\widetilde{a}^{+}_{abcd} = \sqrt{f_b - f_a} a^{+}_{abcd} \sqrt{1 - f_c - f_d}, \tag{D.30}$$

$$\widetilde{b}^{T}_{abcd} = \sqrt{f_b - f_a} b^{T}_{abcd} \sqrt{1 - f_c - f_d}. \tag{D.31}$$

In these equations, the matrix elements read

$$\begin{aligned} A'_{abcd} &= (u_a u_b u_c u_d + v_a v_b v_c v_d) V_{abcd} \\ &\quad + N_{ab}(J) N_{cd}(J) \big[(u_a v_b u_c v_d + v_a u_b v_c u_d) V_{a\bar{d}\bar{b}c} \\ &\quad - (-1)^{j_c + j_d + J} (u_a v_b v_c u_d + v_a u_b u_c v_d) V_{a\bar{c}\bar{b}d} \big] \end{aligned} \tag{D.32}$$

$$\begin{aligned} B_{abcd} &= -(u_a u_b v_c v_d + v_a v_b u_c u_d) V_{ab\bar{c}\bar{d}} \\ &\quad + N_{ab}(J) N_{cd}(J) \big[(u_a v_b v_c u_d + v_a u_b u_c v_d) V_{ad\bar{c}\bar{b}} \\ &\quad - (-1)^{j_c + j_d + J} (u_a v_b u_c v_d + v_a u_b v_c u_d) V_{ac\bar{b}\bar{d}} \big] \end{aligned} \tag{D.33}$$

$$\begin{aligned} C'_{abcd} &= +(u_a v_b u_c v_d + v_a u_b v_c u_d) V_{a\bar{b}c\bar{d}} \\ &\quad + N_{ab}(J) N_{cd}(J) \big[(u_a u_b u_c u_d + v_a v_b v_c v_d) V_{adbc} \\ &\quad + (-1)^{j_c + j_d + J} (u_a u_b v_c v_d + v_a v_b u_c u_d) V_{a\bar{c}b\bar{d}} \big] \end{aligned} \tag{D.34}$$

$$\begin{aligned} D_{abcd} &= +(u_a v_b v_c u_d + v_a u_b u_c v_d) V_{a\bar{b}\bar{c}d} \\ &\quad - N_{ab}(J) N_{cd}(J) \big[(u_a u_b v_c v_d + v_a v_b u_c u_d) V_{a\bar{d}b\bar{c}} \\ &\quad - (-1)^{j_c + j_d + J} (u_a u_b u_c u_d + v_a v_b v_c v_d) V_{acbd} \big] \end{aligned} \tag{D.35}$$

$$
\begin{aligned}
a_{abcd} = &(v_a u_b v_c v_d - u_a v_b u_c u_d) V_{a\bar{b}cd} \\
&- N_{ab}(J) N_{cd}(J) \big[(v_a v_b v_c u_d - u_a u_b u_c v_d) V_{a\bar{d}bc} \\
&+ (-1)^{j_c + j_d + J} (v_a v_b u_c v_d - u_a u_b v_c u_d) V_{a\bar{c}bd} \big]
\end{aligned} \tag{D.36}
$$

$$
\begin{aligned}
b_{abcd} = &-(v_a u_b u_c u_d - u_a v_b v_c v_d) V_{\bar{a}bcd} \\
&- N_{ab}(J) N_{cd}(J) \big[(v_a v_b u_c v_d - u_a u_b v_c u_d) V_{adb\bar{c}} \\
&+ (-1)^{j_c + j_d + J} (v_a v_b v_c u_d - u_a u_b u_c v_d) V_{a\bar{c}bd} \big]
\end{aligned} \tag{D.37}
$$

$$
\begin{aligned}
a^{+}_{abcd} = &(v_a v_b v_c u_d - u_a u_b u_c v_d) V_{a\bar{b}cd} \\
&- N_{ab}(J) N_{cd}(J) \big[(v_a u_b v_c v_d - u_a v_b u_c u_d) V_{a\bar{d}bc} \\
&- (-1)^{j_c + j_d + J} (v_a u_b u_c u_d - u_a v_b v_c v_d) V_{a\bar{c}bd} \big]
\end{aligned} \tag{D.38}
$$

$$
\begin{aligned}
b^{T}_{abcd} = &+(v_a v_b u_c v_d - u_a u_b v_c u_d) V_{\bar{a}bcd} \\
&+ N_{ab}(J) N_{cd}(J) \big[(v_a u_b u_c u_d - u_a v_b v_c v_d) V_{adb\bar{c}} \\
&+ (-1)^{j_c + j_d + J} (v_a u_b v_c v_d - u_a v_b u_c u_d) V_{a\bar{c}bd} \big]
\end{aligned} \tag{D.39}
$$

Since the matrix elements are independent of M, the X, Y, P and Q amplitudes must also be independent of M. The eigenvectors and eigenenergies of Eq. (D.23) will be denoted in the following by ($\tilde{P}$, $\tilde{X}$, $\tilde{Y}$, $\tilde{Q}$) and E_N, respectively. The "core" of the RPA matrix containing $\tilde{A}$ and $\tilde{B}$ (and their complex conjugates) describes the effects of two-quasiparticle excitations ($a^{\dagger}a^{\dagger}$ and aa). We are left with this core in the zero temperature limit. When the temperature of the system is raised, the remaining outer parts of the matrix become important and the quasi-particle occupation probabilities increase above the Fermi level. Due to the effect of one-quasiparticle excitations at finite temperature, the strength function and the width of the resonances change considerably.

Normalization condition for the FT-QRPA equation (D.23) are given as

$$\begin{aligned}\delta_{\nu\nu'} &= \langle \nu|\nu'\rangle = \left\langle QRPA\left|\Gamma_\nu\Gamma^\dagger_{\nu'}\right|QRPA\right\rangle = \left\langle QRPA\left|\left[\Gamma_\nu\Gamma^\dagger_{\nu'}\right]\right|QRPA\right\rangle \\ &= \sum_{\substack{a\geq b\\ c\geq d}}\Bigg[\widetilde{X}^{\nu*}_{ab}\widetilde{X}^{\nu'}_{cd}\left\langle QRPA\left|\left[A_{ab}(JM),A^\dagger_{cd}(J'M')\right]\right|QRPA\right\rangle \\ &+\widetilde{Y}^{\nu*}_{ab}\widetilde{Y}^{\nu'}_{cd}\left\langle QRPA\left|\left[A^\dagger_{ab}(\widetilde{JM}),A_{cd}(\widetilde{J'M'})\right]\right|QRPA\right\rangle \\ &+\widetilde{P}^{\nu*}_{ab}\widetilde{P}^{\nu'}_{cd}\left\langle QRPA\left|\left[B_{ab}(JM),B^\dagger_{cd}(J'M')\right]\right|QRPA\right\rangle \\ &+\widetilde{Q}^{\nu*}_{ab}\widetilde{Q}_{cd}\left\langle QRPA\left|\left[B^\dagger_{ab}(\widetilde{JM}),B_{cd}(\widetilde{J'M'})\right]\right|QRPA\right\rangle\Bigg]\end{aligned} \tag{D.40}$$

If we perform expectation values of commutators, equation (D.40) becomes

$$\delta_{\nu,\nu'} = \delta_{J,J'}\delta_{M,M'}\delta_{ac}\delta_{bd}\sum_{a\geq b}\left(\widetilde{X}^{\nu*}_{ab}\widetilde{X}^{\nu'}_{ab}-\widetilde{Y}^{\nu*}_{ab}\widetilde{Y}^{\nu'}_{ab}+\widetilde{P}^{\nu*}_{ab}\widetilde{P}^{\nu'}_{ab}-\widetilde{Q}^{\nu*}_{ab}\widetilde{Q}^{\nu'}_{ab}\right). \tag{D.41}$$

which gives the normalization condition for FT-QRPA. This Normalization condition can be written as

$$\sum_{a\geq b}\left(\left|\widetilde{X}^{\nu}_{ab}\right|^2-\left|\widetilde{Y}^{\nu}_{ab}\right|^2+\left|\widetilde{P}^{\nu}_{ab}\right|^2-\left|\widetilde{Q}^{\nu}_{ab}\right|^2\right)=1. \tag{D.42}$$

At finite temperature, the reduced transition probability is given by

$$\begin{aligned}B(EJ,J_i\to J_f) = \frac{1}{2J_i+1}\Bigg|\sum_{c\geq d}N_{cd}(J)\Big[&(X^\nu_{cd}+Y^\nu_{cd})(v_cu_d+u_cv_d)(1-f_c-f_d) \\ &+(P^\nu_{cd}+Q^\nu_{cd})(u_cu_d-v_cv_d)(f_d-f_c)\Big]\Bigg|^2.\end{aligned} \tag{D.43}$$

At finite temperature, the transition density reads

$$\begin{aligned}\delta\rho^{n(p)}(r) = \sum_{cd}\Big[&(X^\nu_{cd}+Y^\nu_{cd})\,(u_cv_d+v_du_c)\,(1-f_d-f_c) \\ &+(P^\nu_{cd}+Q^\nu_{cd})\,(u_cu_d+v_cv_d)\,(f_d-f_c)\Big]\,\langle c||Y_J||d\rangle\, R_a(r)R_b(r).\end{aligned} \tag{D.44}$$

After the calculation of the transition probabilities, we can obtain the strength functions of the excitations.

D.1 Commutation Relations at Finite Temperature

In this part, we present some of the commutation relations which are used throughout the derivation of the FT-QRPA equations. Consider,

$$\begin{aligned}
&\langle BCS|[A_{ab}(JM), A^{\dagger}_{cd}(J'M')]|BCS\rangle \\
&= N_{ab}(J)N_{cd}(J)\sum_{\substack{m_a m_b \\ m_c m_d}} \langle j_a m_a j_b m_b\,|JM\rangle \,\langle j_c m_c j_d m_d\,|JM\rangle \left\langle \left[a_b a_a, a^{\dagger}_c a^{\dagger}_d\right]\right\rangle .
\end{aligned} \tag{D.45}$$

Then, we proceed with the commutators of the operators. At finite temperature, $\langle a^{\dagger}_j a_i\rangle = \delta_{ij} f_i$ and $\langle a_j a^{\dagger}_i\rangle = \delta_{ij}(1-f_j)$ where f_i is the temperature dependent Fermi-Dirac Distribution function

$$\begin{aligned}
\langle [a_b a_a, a^{\dagger}_c a^{\dagger}_d]\rangle &= \langle a_b a_a a^{\dagger}_c a^{\dagger}_d\rangle - \langle a^{\dagger}_c a^{\dagger}_d a_b a_a\rangle \\
&= \langle a_b a^{\dagger}_d\rangle \delta_{ac} - \langle a_a a^{\dagger}_d\rangle \delta_{bc} + \langle a^{\dagger}_c a_b\rangle \delta_{ad} - \langle a^{\dagger}_c a_a\rangle \delta_{bd} \\
&= \delta_{ac}\delta_{bd}(1-f_a-f_b) - \delta_{ad}\delta_{bc}(1-f_a-f_b),
\end{aligned} \tag{D.46}$$

and we obtain

$$\begin{aligned}
&\langle BCS|[A_{ab}(JM), A^{\dagger}_{cd}(J'M')]|BCS\rangle \\
&= N_{ab}(J)^2 \delta_{JJ'}\delta_{MM'}\left[\delta_{ac}\delta_{bd} - (-1)^{j_a+j_b+J}\delta_{ad}\delta_{bc}\right](1-f_a-f_b).
\end{aligned} \tag{D.47}$$

Secondly, consider

$$\begin{aligned}
&\langle BCS|[B_{ab}(JM), B^{\dagger}_{cd}(J'M')]|BCS\rangle \\
&= N_{ab}(J)N_{cd}(J)\sum_{\substack{m_a m_b \\ m_c m_d}} \langle j_a m_a j_b - m_b\,|JM\rangle \,\langle j_c m_c j_d - m_d\,|JM\rangle \\
&\times (-)^{j_b-m_b}(-)^{j_d-m_d}\left\langle \left[a^{\dagger}_b a_a, a^{\dagger}_c a_d\right]\right\rangle
\end{aligned} \tag{D.48}$$

and the commutation relations give

$$\begin{aligned}
\langle [a^{\dagger}_b a_a, a^{\dagger}_c a_d]\rangle &= \langle a^{\dagger}_b a_a a^{\dagger}_c a_d\rangle - \langle a^{\dagger}_c a_d a^{\dagger}_b a_a\rangle \\
&= \langle a^{\dagger}_b a_d\rangle \delta_{ac} - \langle a^{\dagger}_b a^{\dagger}_c a_a a_d\rangle + \langle a^{\dagger}_c a_a\rangle \delta_{bd} + \langle a^{\dagger}_c a^{\dagger}_b a_a a_a\rangle \\
&= \delta_{ac}\delta_{bd}(f_d-f_a).
\end{aligned} \tag{D.49}$$

Finally, we have

$$\begin{aligned}&\langle BCS|[B_{ab}(JM),B^{\dagger}_{cd}(J'M')]|BCS\rangle\\&=N_{ab}(J)^2\delta_{JJ'}\delta_{MM'}\delta_{ac}\delta_{bd}(f_d-f_c).\end{aligned}\tag{D.50}$$

D.1.1 The A Matrix at Finite Temperatures

In this section, we present the analytical solution for the A matrix of the QRPA at finite temperatures. The coupled operators can be defined as:

$$A_{ab}(JM)=N_{ab}(J)\sum_{m_am_b}\langle j_am_aj_bm_b|JM\rangle a_ba_a,\tag{D.51}$$

$$A^{\dagger}_{cd}(JM)=N_{cd}(J)\sum_{m_cm_d}\langle j_cm_cj_dm_d|JM\rangle a^{\dagger}_ca^{\dagger}_d,\tag{D.52}$$

and the part of the Hamiltonian, the residual interaction (H_{22}) is written as:

$$H_{22}=V_{a'b'c'd'}\left[\frac{1}{4}(u_{a'}u_{b'}u_{c'}u_{d'}+v_{a'}v_{b'}v_{c'}v_{d'})a^{\dagger}_{a'}a^{\dagger}_{b'}a_{d'}a_{c'}-(u_{a'}v_{b'}u_{c'}v_{d'})a^{\dagger}_{a'}\tilde{a}^{\dagger}_{d'}\tilde{a}_{b'}a_{c'}\right]\tag{D.53}$$

The A matrix of the FT-QRPA is given by

$$\widetilde{A}_{abcd}=\left\langle\left[A_{ab}(JM),\left[H_{22},A^{\dagger}_{cd}(JM)\right]\right]\right\rangle.\tag{D.54}$$

Since we have two creation and two annihilation operators in the A operator, only H_{22} part of the residual interaction contributes to the commutator. If we expand Eq. D.54, we obtain

$$\begin{aligned}\widetilde{A}_{abcd}=&\left\langle A_{ab}(JM)H_{22}A^{\dagger}_{cd}(JM)\right\rangle-\left\langle H_{22}A^{\dagger}_{cd}(JM)A_{ab}(JM)\right\rangle\\&-\left\langle A_{ab}(JM)A^{\dagger}_{cd}(JM)H_{22}\right\rangle+\left\langle A^{\dagger}_{cd}(JM)H_{22}A_{ab}(JM)\right\rangle.\end{aligned}\tag{D.55}$$

In order to evaluate the expectation values, we need the BCS expectation values of the commutators of the quasiparticle pair operators which are defined above. In QRPA, the ground state (vacuum) is defined by $a|BCS\rangle=0$. However, it is not vacuum at finite temperatures, i.e., $a|BCS\rangle\neq 0$. Furthermore, the single quasiparticle density matrix reads $\rho_{ij}=\langle a^{\dagger}_ja_i\rangle=\delta_{ij}f_i$ or $\langle a_ja^{\dagger}_i\rangle=\delta_{ij}(1-f_j)$ where f_i is the temperature dependent Fermi-

Dirac Distribution function.

To simplify the the derivation of the A matrix, we divide the H_{22} into two parts in order to perform analytical expressions. Form the first part og H_{22}, we have

$$\left\langle A_{ab}(JM) : H_{22} : A^{\dagger}_{cd}(JM) \right\rangle = \left\langle a_b a_a : a^{\dagger}_{a'} a^{\dagger}_{b'} a_{d'} a_{c'} : a^{\dagger}_{c} a^{\dagger}_{d} \right\rangle . \tag{D.56}$$

Using the Wick's theorem at finite temperature, we obtain

$$\begin{aligned}\left\langle a_b a_a : a^{\dagger}_{a'} a^{\dagger}_{b'} a_{d'} a_{c'} : a^{\dagger}_{c} a^{\dagger}_{d} \right\rangle =&[\delta_{aa'}\delta_{bb'}\delta_{cc'}\delta_{dd'} - \delta_{ab'}\delta_{ba'}\delta_{cc'}\delta_{dd'} \\ &- \delta_{aa'}\delta_{bb'}\delta_{cd'}\delta_{dc'} + \delta_{ab'}\delta_{ba'}\delta_{cd'}\delta_{dc'}] \\ &\times (1-f_a)(1-f_b)(1-f_{c'})(1-f_{d'}).\end{aligned} \tag{D.57}$$

In a similar fashion, the expectation values of other parts are

$$\begin{aligned}-\left\langle H_{22} A^{\dagger}_{cd}(JM) A_{ab}(JM) \right\rangle =& -\left\langle : a^{\dagger}_{a'} a^{\dagger}_{b'} a_{d'} : a_{c'} a^{\dagger}_{c} a^{\dagger}_{d} a_b a_a \right\rangle \\ =& -[\delta_{aa'}\delta_{bb'}\delta_{cc'}\delta_{dd'} - \delta_{ab'}\delta_{ba'}\delta_{cc'}\delta_{dd'} \\ &- \delta_{aa'}\delta_{bb'}\delta_{cd'}\delta_{dc'} + \delta_{ab'}\delta_{ba'}\delta_{cd'}\delta_{dc'}] \\ &\times (f_a f_b)(1-f_{c'})(1-f_{d'}),\end{aligned} \tag{D.58}$$

$$\begin{aligned}-\left\langle A_{ab}(JM) A^{\dagger}_{cd}(JM) H_{22} \right\rangle =& -\left\langle a_b a_a a^{\dagger}_{c} a^{\dagger}_{d} : a^{\dagger}_{a'} a^{\dagger}_{b'} a_{d'} a_{c'} : \right\rangle \\ =& -[\delta_{aa'}\delta_{bb'}\delta_{cc'}\delta_{dd'} - \delta_{ab'}\delta_{ba'}\delta_{cc'}\delta_{dd'} \\ &- \delta_{aa'}\delta_{bb'}\delta_{cd'}\delta_{dc'} + \delta_{ab'}\delta_{ba'}\delta_{cd'}\delta_{dc'}] \\ &\times (f_{c'} f_{d'})(1-f_a)(1-f_b),\end{aligned} \tag{D.59}$$

$$\begin{aligned}\left\langle A^{\dagger}_{cd}(JM) H_{22} A_{ab}(JM) \right\rangle =& \left\langle a^{\dagger}_{c} a^{\dagger}_{d} : a^{\dagger}_{a'} a^{\dagger}_{b'} a_{d'} a_{c'} : a_b a_a \right\rangle \\ =& [\delta_{aa'}\delta_{bb'}\delta_{cc'}\delta_{dd'} - \delta_{ab'}\delta_{ba'}\delta_{cc'}\delta_{dd'} \\ &- \delta_{aa'}\delta_{bb'}\delta_{cd'}\delta_{dc'} + \delta_{ab'}\delta_{ba'}\delta_{cd'}\delta_{dc'}] \\ &\times (f_{c'} f_{d'} f_a f_b)\end{aligned} \tag{D.60}$$

with the summation of all expectation values we obtain:

$$
\begin{aligned}
A_{ab,cd}(JM) =& \frac{1}{4} N_{ab}(J) N_{cd}(J) \sum_{\substack{m_a m_b \\ m_c m_d}} \langle j_a m_a j_b m_b | JM \rangle \langle j_c m_c j_d m_d | JM \rangle \\
& \times \sum_{\substack{m_{a'} m_{b'} \\ m_{c'} m_{d'}}} (u_{a'} u_{b'} u_{c'} u_{d'} + v_{a'} v_{b'} v_{c'} v_{d'}) V_{a'b'c'd'} \\
& \times [\delta_{aa'} \delta_{bb'} \delta_{cc'} \delta_{dd'} - \delta_{ab'} \delta_{ba'} \delta_{cc'} \delta_{dd'} \\
& - \delta_{aa'} \delta_{bb'} \delta_{cd'} \delta_{dc'} + \delta_{ab'} \delta_{ba'} \delta_{cd'} \delta_{dc'}] \\
& \times (1 - f_{a'} - f_{b'})(1 - f_{c'} - f_{d'}).
\end{aligned}
\tag{D.61}
$$

The different terms of the A matrix are processed below.

$$
(u_{a'} u_{b'} u_{c'} u_{d'} + v_{a'} v_{b'} v_{c'} v_{d'}) V_{a'b'c'd'} \times \delta_{aa'} \delta_{bb'} \delta_{cc'} \delta_{dd'} \tag{D.62}
$$

where $a = a'$, $b = b'$, $c = c'$ and $d = d'$ makes

$$
V_{abcd}(u_a u_b u_c u_d + v_a v_b v_c v_d). \tag{D.63}
$$

Similarly, for the second part of the dirac delta functions, we obtain

$$
V_{bacd}(u_a u_b u_c u_d + v_a v_b v_c v_d). \tag{D.64}
$$

If we continue with the other parts,

$$
V_{abdc}(u_a u_b u_c u_d + v_a v_b v_c v_d), \tag{D.65}
$$

$$
V_{badc}(u_a u_b u_c u_d + v_a v_b v_c v_d), \tag{D.66}
$$

using the symmetry relations,

$$
V_{bacd} = V_{abdc} = V_{badc} = V_{abcd}. \tag{D.67}
$$

The interaction is given by

$$
\begin{aligned}
V_{abcd} = [N_{ab}(J') N_{cd}(J')]^{-1} \sum_{J'M'} & \langle j_a m_a j_b m_b | JM \rangle \langle j_c m_c j_d m_d | JM \rangle \\
& \times \left\langle ab; J' \right| V \left| cd; J' \right\rangle
\end{aligned}
\tag{D.68}
$$

Summation of the four terms gives the A matrix in angular momentum coupled form:

$$
\begin{aligned}
A_{ab,cd}(JM) =& \frac{1}{4} N_{ab}(J) N_{cd}(J) \sum_{\substack{m_a m_b \\ m_c m_d}} \langle j_a m_a j_b m_b | JM \rangle \langle j_c m_c j_d m_d | JM \rangle \\
& \times [N_{ab}(J') N_{cd}(J')]^{-1} \sum_{J'M'} \langle j_a m_a j_b m_b | JM \rangle \langle j_c m_c j_d m_d | JM \rangle \\
& \times 4(u_a u_b u_c u_d + v_a v_b v_c v_d) \times \langle ab;J|V|cd;J \rangle \\
& \times (1 - f_a - f_b)(1 - f_c - f_d)
\end{aligned}
\tag{D.69}
$$

after checking the signs of the angular momentum couplings, we obtain the one part of the A matrix:

$$
\begin{aligned}
A_{ab,cd}(JM) =& (u_a u_b u_c u_d + v_a v_b v_c v_d) \times \langle ab;J|V|cd;J \rangle \\
& \times (1 - f_a - f_b)(1 - f_c - f_d).
\end{aligned}
\tag{D.70}
$$

Since we have $u-u$ and $v-v$ pairs, this interaction is an p-p interaction. Now, we continue with the second term of H_{22}:

$$
H_{22}^2 = - \sum_{a'b'c'd'} V_{a'b'c'd'} (u_{a'} v_{b'} u_{c'} v_{d'}) : a_{a'}^\dagger \tilde{a}_{d'}^\dagger \tilde{a}_{b'} a_{c'} : \tag{D.71}
$$

Then, we remove tildes from the operators using the relation $\tilde{a}_d = (-1)^{j_d + m_d} a_{d,-m_d} = (-1)^{j_d - m_d} a_{d,m_d}$. Finally, H_{22} reads:

$$
H_{22}^2 = - \sum_{a'b'c'd'} V_{a'b'c'd'} (u_{a'} v_{b'} u_{c'} v_{d'}) : a_{a'}^\dagger a_{d'}^\dagger a_{b'} a_{c'} : (-)^{j_{b'} - m_{b'}} (-)^{j_{d'} - m_{d'}}. \tag{D.72}
$$

Now, we evaluate the expectation values of the following:

$$
\left\langle A_{ab}(JM) : H_{22} : A_{cd}^\dagger(JM) \right\rangle = - \left\langle a_b a_a : a_{a'}^\dagger a_{d'}^\dagger a_{b'} a_{c'} : a_c^\dagger a_d^\dagger \right\rangle \tag{D.73}
$$

$$
\begin{aligned}
- \left\langle a_b a_a : a_{a'}^\dagger a_{d'}^\dagger a_{b'} a_{c'} : a_c^\dagger a_d^\dagger \right\rangle =& [\delta_{ad'} \delta_{ba'} \delta_{cb'} \delta_{dc'} - \delta_{ad'} \delta_{ba'} \delta_{cc'} \delta_{db'} \\
& + \delta_{aa'} \delta_{bd'} \delta_{cc'} \delta_{db'} - \delta_{aa'} \delta_{bd'} \delta_{cb'} \delta_{dc'}] \\
& \times (1 - f_b)(1 - f_a)(1 - f_{b'})(1 - f_{c'})
\end{aligned}
\tag{D.74}
$$

Second term :

$$\left\langle : H_{22} : A^{\dagger}_{cd}(JM) A_{ab}(JM) \right\rangle = -\left\langle : a^{\dagger}_{a'} a^{\dagger}_{d'} a_{b'} a_{c'} : a^{\dagger}_{c} a^{\dagger}_{d} a_{b} a_{a} \right\rangle \tag{D.75}$$

$$\begin{aligned} -\left\langle : a^{\dagger}_{a'} a^{\dagger}_{d'} a_{b'} a_{c'} : a^{\dagger}_{c} a^{\dagger}_{d} a_{b} a_{a} \right\rangle =& [\delta_{ad'}\delta_{ba'}\delta_{cb'}\delta_{dc'} - \delta_{ad'}\delta_{ba'}\delta_{cc'}\delta_{db'} \\ & + \delta_{aa'}\delta_{bd'}\delta_{cc'}\delta_{db'} - \delta_{aa'}\delta_{bd'}\delta_{cb'}\delta_{dc'}] \\ & \times (1-f_{b'})(1-f_{c'}) f_a f_b \end{aligned} \tag{D.76}$$

We obtain similar results from third and fourth expectation values. At the end, the A matrix is:

$$\begin{aligned} A_{ab,cd}(JM) =& N_{ab}(J) N_{cd}(J) \sum_{\substack{m_a m_b \\ m_c m_d}} \langle j_a m_a j_b m_b | JM \rangle \langle j_c m_c j_d m_d | JM \rangle \\ & \times \sum_{a'b'c'd'} (-)^{j_{b'}-m_{b'}} (-)^{j_{d'}-m_{d'}} (u_{a'} v_{b'} u_{c'} v_{d'}) V_{a'\tilde{b}'c'\tilde{d}'} \\ & \times [-\delta_{ad'}\delta_{ba'}\delta_{cb'}\delta_{dc'} + \delta_{ad'}\delta_{ba'}\delta_{cc'}\delta_{db'} - \delta_{aa'}\delta_{bd'}\delta_{cc'}\delta_{db'} + \delta_{aa'}\delta_{bd'}\delta_{cb'}\delta_{dc'}] \\ & \times (1-f_a-f_b)(1-f_{c'}-f_{b'}) \end{aligned} \tag{D.77}$$

If we evaluate the A matrix in Eq. D.77:

$$\begin{aligned} & 1)\delta_{ad'}\delta_{ba'}\delta_{cb'}\delta_{dc'} \times V_{a'\tilde{b}'c'\tilde{d}'} (-)^{j_{b'}-m_{b'}} (-)^{j_{d'}-m_{d'}} \\ & \times (u_{a'} v_{b'} u_{c'} v_{d'}) \times (1-f_a-f_b)(1-f_{c'}-f_{b'}) \\ & = -V_{b\tilde{c}d\tilde{a}} \times (v_a u_b v_c u_d) \times (-)^{j_a-m_a} (-)^{j_c-m_c} \times (1-f_a-f_b)(1-f_c-f_d) \end{aligned} \tag{D.78}$$

$$\begin{aligned} & 2)\delta_{ad'}\delta_{ba'}\delta_{cc'}\delta_{db'} \times V_{a'\tilde{b}'c'\tilde{d}'} (-)^{j_{b'}-m_{b'}} (-)^{j_{d'}-m_{d'}} \\ & \times (u_{a'} v_{b'} u_{c'} v_{d'}) \times (1-f_a-f_b)(1-f_{c'}-f_{b'}) \\ & = V_{b\tilde{d}c\tilde{a}} \times (v_a u_b u_c v_d) \times (-)^{j_a-m_a} (-)^{j_d-m_d} \times (1-f_a-f_b)(1-f_c-f_d) \end{aligned} \tag{D.79}$$

$$3)\delta_{bd'}\delta_{aa'}\delta_{cb'}\delta_{dc'}\times V_{a'\tilde{b}'c'\tilde{d}'}(-)^{j_{b'}-m_{b'}}(-)^{j_{d'}-m_{d'}}$$
$$\times(u_{a'}v_{b'}u_{c'}v_{d'})\times(1-f_a-f_b)(1-f_{c'}-f_{b'}) \tag{D.80}$$
$$=V_{a\tilde{c}d\tilde{b}}\times(u_a v_b v_c u_d)\times(-)^{j_c-m_c}(-)^{j_b-m_b}\times(1-f_a-f_b)(1-f_c-f_d)$$

$$4)-\delta_{aa'}\delta_{bd'}\delta_{cc'}\delta_{db'}\times V_{a'\tilde{b}'c'\tilde{d}'}(-)^{j_{b'}-m_{b'}}(-)^{j_{d'}-m_{d'}}$$
$$\times(u_{a'}v_{b'}u_{c'}v_{d'})\times(1-f_a-f_b)(1-f_{c'}-f_{b'}) \tag{D.81}$$
$$=-V_{a\tilde{d}c\tilde{b}}\times(u_a v_b u_c v_d)\times(-)^{j_b-m_b}(-)^{j_d-m_d}\times(1-f_a-f_b)(1-f_c-f_d)$$

Using the symmetry properties $-v_{b\tilde{c}d\tilde{a}}=-v_{d\tilde{a}b\tilde{c}}=v_{a\tilde{d}b\tilde{c}}$. It should be noted that 1(2) and 4(3)are equal in interaction. We define the p-h interaction in angular momentum coupled form as:

$$V_{a\tilde{d}\tilde{b}c}=N_{ab}(J')N_{cd}(J')\sum_{J'M'}\langle j_a m_a j_b m_b|J'M'\rangle\langle j_c m_c j_d m_d|J'M'\rangle \\ \times(-)^{j_b+m_b+j_d+m_d}v_{a\tilde{d}\tilde{b}c} \tag{D.82}$$

we can use Eq. D.82 in order to derive $v_{a\tilde{c}\tilde{b}d}$ as:

$$V_{a\tilde{c}\tilde{b}d}=N_{ab}(J')N_{cd}(J')\sum_{J'M'}\langle j_a m_a j_b m_b|J'M'\rangle\langle j_d m_d j_c m_c|J'M'\rangle \\ \times(-)^{j_b+m_b+j_c+m_c}v_{a\tilde{c}\tilde{b}d} \tag{D.83}$$

After checking the phase factors, from 1 and 4 we have

$$N_{ab}(J')N_{cd}(J')(u_a v_b u_c v_d+v_a u_b v_c u_d)\times V_{a\tilde{d}\tilde{b}c}\times(1-f_a-f_b)(1-f_c-f_d) \tag{D.84}$$

Since we have $u-v$ and $v-u$ pairs, we have p-h interaction in this part. From 2 and 3 we have

$$-(-)^{j_c+j_d+J}N_{ab}(J')N_{cd}(J')(u_a v_b v_c u_d+v_a u_b u_c v_d)\times V_{a\tilde{c}\tilde{b}d}\times(1-f_a-f_b)(1-f_c-f_d) \tag{D.85}$$

again we have a p-h interaction. If we combine the equations, the finite temperature QRPA

A matrix is:

$$
\begin{aligned}
A_{ab,cd} =&(u_a u_b u_c u_d + v_a v_b v_c v_d)V_{abcd} \\
&N_{ab}(J')N_{cd}(J')[(u_a v_b u_c v_d + v_a u_b v_c u_d) \times V_{ad\tilde{\tilde{b}}c} \\
&-(-)^{j_c+j_d+J}(u_a v_b v_c u_d + v_a u_b u_c v_d)V_{a\tilde{c}\tilde{b}d}] \times (1 - f_a - f_b)(1 - f_c - f_d).
\end{aligned} \tag{D.86}
$$

D.2 The FT-QRPA Limit to the FT-RPA

In this section, we give the FT-QRPA limit to FT-RPA in which $V_{pair} = 0$. As it is mentioned in Chapter 8, the p-p and h-h excitations also become possible at finite temperature. Here, we present the contribution of each matrix to the FT-QRPA matrix by analyzing their contribution one by one. Consider p-h and p-h excitations. In this case, we have $v_a = v_c = 0$, $u_a = u_c = 1$, $v_b = v_d = 1$ and $u_b = u_d = 0$ and the FT-QRPA matrices become

$$
\begin{aligned}
A =&V_{adbc} + (E_a + E_b) \\
B =&V_{acbd} \\
C =&(E_a - E_b) \\
D =&0 \\
a =&0 \\
b =&0 \\
a^{+} =&0 \\
b^{T} =&0
\end{aligned} \tag{D.87}
$$

Secondly, we can have p-p and p-p excitations. In this case, we have $v_a = v_b = v_c = v_d = 0$ and $u_a = u_b = u_c = u_d = 1$ and matrices give

$$\begin{aligned}
A =& (E_a + E_b) \\
B =& 0 \\
C =& V_{adbc} + (E_a - E_b) \\
D =& V_{acbd} \\
a =& 0 \\
b =& 0 \\
a^+ =& 0 \\
b^T =& 0
\end{aligned} \tag{D.88}$$

For the h-h and h-h excitations, we have $v_a = v_b = v_c = v_d = 1$ and $u_a = u_b = u_c = u_d = 0$ which gives

$$\begin{aligned}
A =& (E_a + E_b) \\
B =& 0 \\
C =& V_{adbc} + (E_a - E_b) \\
D =& V_{acbd} \\
a =& 0 \\
b =& 0 \\
a^+ =& 0 \\
b^T =& 0
\end{aligned} \tag{D.89}$$

We can also have p-p and p-h excitations, $v_a = v_b = 0$, $u_a = u_b = 1$ and $v_c = u_d = 0$, $u_c = v_d = 1$. In this case,

$$
\begin{aligned}
A =& 0 \\
B =& 0 \\
C =& 0 \\
D =& 0 \\
a =& -V_{adbc} \\
b =& -V_{acbd} \\
a^{+} =& 0 \\
b^{T} =& 0
\end{aligned}
\tag{D.90}
$$

For h-h and p-h excitations, $v_a = v_b = 1$, $u_a = u_b = 0$ and $v_c = u_d = 0$, $u_c = v_d = 1$ which give

$$
\begin{aligned}
A =& 0 \\
B =& 0 \\
C =& 0 \\
D =& 0 \\
a =& V_{acbd} \\
b =& V_{adbc} \\
a^{+} =& 0 \\
b^{T} =& 0
\end{aligned}
\tag{D.91}
$$

For p-h and p-p excitations, $v_a = v_b = 1$, $u_a = u_b = 0$ and $v_c = u_d = 1$, $u_c = v_d = 0$

$$
\begin{aligned}
A =& 0 \\
B =& 0 \\
C =& 0 \\
D =& 0 \\
a =& 0 \\
b =& 0 \\
a^{+} =& -V_{adbc} \\
b^{T} =& -V_{acbd}
\end{aligned}
\tag{D.92}
$$

For p-h and h-h excitations, $v_a = v_b = 0$, $u_a = u_b = 1$ and $v_c = u_d = 1$, $u_c = v_d = 0$ which give

$$
\begin{aligned}
A =& 0 \\
B =& 0 \\
C =& 0 \\
D =& 0 \\
a =& 0 \\
b =& 0 \\
a^{+} =& -V_{acbd} \\
b^{T} =& -V_{adbc}
\end{aligned}
\tag{D.93}
$$

APPENDIX E

THE PARAMETERS OF THE SKYRME INTERACTIONS

In this section, we present the parameters of the Skyrme interactions which are used in the calculations.

Interaction	SLy4	Sly5	SGII	T44	SkX	SGI
$t_0(MeV fm^3)$	-2488.91	-2484.88	-2645.0	-2485.670	-1445.3	-1603.0
$t_1(MeV fm^5)$	486.82	483.13	340.0	494.477	246.9	515.9
$t_2(MeV fm^5)$	-546.39	-549.40	-41.9	-337.961	-131.8	84.5
$t_3(MeV fm^{3+3\sigma})$	13777.0	13763.0	15595.0	13794.75	12103.9	8000.0
x_0	0.834	0.778	0.090	0.721557	0.34	-0.02
x_1	-0.344	-0.328	-0.0588	-0.661848	0.58	-0.5
x_2	-1.0	-1.0	1.425	-0.803184	0.127	-1.731
x_3	1.354	1.267	0.06044	1.175908	0.03	0.1381
σ	1/6	1/6	1/6	1/6	1/6	1/6
$W_0(MeV fm^5)$	123.0	126.0	105.0	161.367	148.0	115.0
$\rho_\infty(fm^{-3})$	0.159	0.16	0.158	0.16	0.155	0.154
$m*/m$	0.6946	0.696	0.785	0.7	0.993	0.607
$J(MeV)$	32.0	32.02	26.83	32 .0	31.09	28.33
$L(MeV)$	45.96	48.269	37.63	50.05	33.18	-63.86

Table E.1 Skyrme interaction parameters.

REFERENCES

[1] Rutherford, E., (1911). “The Scattering of α and β Particles by Matter and the Structure of the Atom”, Philosophical Magazine Series 6, 21: 669-688.

[2] Chadwick, J., (1932). “Possible Existence of a Neutron”, Nature, 129: 312.

[3] Bazin, D., (2012). “Nuclear physics: Symmetrical tin”, Nature, 486: 330-331.

[4] Bender, M., Heenen, P.-H. and Reinhard, P.-G., (2003). “Self-consistent mean-field models for nuclear structure”, Rev. Mod. Phys., 75: 121–180.

[5] Skyrme, T. H. R., (1958). “The effective nuclear potential”, Nuclear Physics, 9: 615 - 634.

[6] Dechargé, J. and Gogny, D., (1980). “Hartree-Fock-Bogolyubov calculations with the $D1$ effective interaction on spherical nuclei”, Phys. Rev. C, 21: 1568–1593.

[7] Vautherin, D. and Brink, D. M., (1972). “Hartree-Fock Calculations with Skyrme’s Interaction. I. Spherical Nuclei”, Phys. Rev. C, 5: 626–647.

[8] Brink, D. M. and Stancu, F., (2007). “Evolution of nuclear shells with the Skyrme density dependent interaction”, Phys. Rev. C, 75: 064311.

[9] Paar, N., Vretenar, D., Khan, E. and Colò, G., (2007). “Exotic modes of excitation in atomic nuclei far from stability”, Reports on Progress in Physics, 70: 691.

[10] Dobaczewski, J., Flocard, H. and Treiner, J., (1984). “Hartree-Fock-Bogolyubov description of nuclei near the neutron-drip line”, Nuclear Physics A, 422: 103 - 139.

[11] Ring, P. and Schuck, P., (1980). The Nuclear Many-Body Problem, Springer-Verlag Berlin Heidelberg.

[12] Suhonen, J., (2007). From Nucleons to Nucleus: Concepts of Microscopic Nuclear Theory, Springer Verlag Berlin Heidelberg.

[13] Sarchi, D., Bortignon, P. and Colò, G., (2004). “Dipole states in stable and unstable nuclei”, Physics Letters B, 601: 27 - 33.

[14] Reinhard, P.-G., (1999). “Skyrme forces and giant resonances in exotic nuclei”, Nuclear Physics A, 649: 305 - 314.

[15] Vitturi, A., (1998). “Excitation of collective modes in neutron-rich nuclei”, Journal of Physics G: Nuclear and Particle Physics, 24: 1439.

[16] Sagawa, H. and Esbensen, H., (2001). “Giant resonances in exotic nuclei”, Nuclear Physics A, 693: 448 - 462.

[17] Adams, J. P., Castel, B. and Sagawa, H., (1996). “Neutron halos and E 1 resonances in ^{208}Pb”, Phys. Rev. C, 53: 1016–1017.

[18] Hamamoto, I., Sagawa, H. and Zhang, X. Z., (1998). “Isoscalar and isovector dipole mode in drip line nuclei in comparison with β-stable nuclei”, Phys. Rev. C, 57: R1064–R1068.

[19] Catara, F., Lanza, E., Nagarajan, M. and Vitturi, A., (1997). “Effect of large neutron excess on the dipole response in the region of the giant dipole resonance”, Nuclear Physics A, 624: 449 - 458.

[20] Roca-Maza, X., Pozzi, G., Brenna, M., Mizuyama, K. and Colò, G., (2012). “Low-lying dipole response: Isospin character and collectivity in ^{68}Ni, ^{132}Sn, and ^{208}Pb”, Phys. Rev. C, 85: 024601.

[21] Hamamoto, I., Sagawa, H. and Zhang, X. Z., (1997). “Giant monopole resonances in nuclei near stable and drip lines”, Phys. Rev. C, 56: 3121–3133.

[22] Terasaki, J. and Engel, J., (2006). “Self-consistent description of multipole strength: Systematic calculations”, Phys. Rev. C, 74: 044301.

[23] Khan, E., Paar, N. and Vretenar, D., (2011). “Low-energy monopole strength in exotic nickel isotopes”, Phys. Rev. C, 84: 051301.

[24] Khan, E., (2009). “Giant monopole resonance in Pb isotopes”, Phys. Rev. C, 80: 057302.

[25] Khan, E., Margueron, J. and Vidaña, I., (2012). “Constraining the Nuclear Equation of State at Subsaturation Densities”, Phys. Rev. Lett., 109: 092501.

[26] Terasaki, J., Engel, J., Bender, M., Dobaczewski, J., Nazarewicz, W. and Stoitsov, M., (2005). “Self-consistent description of multipole strength in exotic nuclei: Method”, Phys. Rev. C, 71: 034310.

[27] Cao, L.-G., Sagawa, H. and Colò, G., (2012). “Microscopic study of the isoscalar giant monopole resonance in Cd, Sn, and Pb isotopes”, Phys. Rev. C, 86: 054313.

[28] Migdal, A. B., (1944). “check”, J. Phys., 8: 331.

[29] Goldhaber, M. and Teller, E., (1948). “On Nuclear Dipole Vibrations”, Phys. Rev., 74: 1046–1049.

[30] Steinwedel, H., Jensen, J. H. D. and Jensen, P., (1950). “Nuclear Dipole Vibrations”, Phys. Rev., 79: 1019–1019.

[31] Kobayashi T., et. al., (1989). “Electromagnetic dissociation and soft giant dipole resonance of the neutron-dripline nucleus 11Li”, Physics Letters B, 232: 51 - 55.

[32] Aumann T., et. al., (1999). “Giant resonances in unstable oxygen isotopes”, Nuclear Physics A, 649: 297 - 304.

[33] Hartmann, T., Babilon, M., Kamerdzhiev, S., Litvinova, E., Savran, D., Volz, S. and Zilges, A., (2004). “Microscopic Nature of the Pygmy Dipole Resonance: The Stable Ca Isotopes”, Phys. Rev. Lett., 93: 192501.

[34] Adrich P., et. al., (2005). “Evidence for Pygmy and Giant Dipole Resonances in ^{130}Sn and ^{132}Sn”, Phys. Rev. Lett., 95: 132501.

[35] Vretenar, D., Paar, N., Ring, P. and Lalazissis, G., (2001). “Collectivity of the low-lying dipole strength in relativistic random phase approximation”, Nuclear Physics A, 692: 496 - 517.

[36] Vretenar, D., Paar, N., Ring, P. and Lalazissis, G. A., (2001). “Pygmy dipole resonances in the relativistic random phase approximation”, Phys. Rev. C, 63: 047301.

[37] Piekarewicz, J., (2006). “Pygmy dipole resonance as a constraint on the neutron skin of heavy nuclei”, Phys. Rev. C, 73: 044325.

[38] Piekarewicz, J., (2011). “Pygmy resonances and neutron skins”, Phys. Rev. C, 83: 034319.

[39] Klimkiewicz A., et. al., (2007). “Nuclear symmetry energy and neutron skins derived from pygmy dipole resonances”, Phys. Rev. C, 76: 051603.

[40] Goriely, S., Khan, E. and Samyn, M., (2004). “Microscopic {HFB} + {QRPA} predictions of dipole strength for astrophysics applications”, Nuclear Physics A, 739: 331 - 352.

[41] Vandebrouck M., et. al., (2014). “Measurement of the Isoscalar Monopole Response in the Neutron-Rich Nucleus ^{68}Ni”, Phys. Rev. Lett., 113: 032504.

[42] Vandebrouck M., et. al., (2015). “Isoscalar response of ^{68}Ni to α-particle and deuteron probes”, Phys. Rev. C, 92: 024316.

[43] Mayer, M. G., (1949). “On Closed Shells in Nuclei. II”, Phys. Rev., 75: 1969–1970.

[44] Liddick S., et. al., (2004). “Lowest Excitations in ^{56}Ti and the Predicted $N = 34$ Shell Closure”, Phys. Rev. Lett., 92: 072502.

[45] Fridmann J., et. al., (2005). “Magic nucleus Si-42”, Nature, 435: 922-924.

[46] Gade A., et. al., (2006). “Cross-shell excitation in two-proton knockout: Structure of ^{52}Ca”, Phys. Rev. C, 74: 021302.

[47] Sorlin, O. and Porquet, M.-G., (2008). “Nuclear magic numbers: New features far from stability”, Progress in Particle and Nuclear Physics, 61: 602 - 673.

[48] Kanungo R., et. al., (2009). “One-Neutron Removal Measurement Reveals ^{24}**O** as a New Doubly Magic Nucleus”, Phys. Rev. Lett., 102: 152501.

[49] Hoffman C. R., et. al., (2009). "Evidence for a doubly magic 24O", Physics Letters B, 672: 17 - 21.

[50] Steppenbeck D., et. al., (2013). "Evidence for a new nuclear magic number from the level structure of 54Ca", Nature, 502: 207-210.

[51] Colò, G., Sagawa, H., Fracasso, S. and Bortignon, P., (2007). "Spin orbit splitting and the tensor component of the Skyrme interaction", Physics Letters B, 646: 227 - 231.

[52] Sano, M. and Yamasaki, S., (1963). "Phase Transition and Level Density of Atomic Nuclei", Progress of Theoretical Physics, 29: 397-414.

[53] Goodman, A. L., (1981). "Finite-temperature HFB theory", Nuclear Physics A, 352: 30-44.

[54] Gambacurta, D., Lacroix, D. and Sandulescu, N., (2013). "Pairing and specific heat in hot nuclei", Phys. Rev. C, 88: 034324.

[55] Goodman, A. L., (1986). "Finite-temperature Hartree-Fock-Bogoliubov calculations in rare earth nuclei", Phys. Rev. C, 34: 1942–1949.

[56] Egido, J. L. and Ring, P., (1993). "The decay of hot nuclei", Journal of Physics G: Nuclear and Particle Physics, 19: 1.

[57] Martin, V., Egido, J. L. and Robledo, L. M., (2003). "Thermal shape fluctuation effects in the description of hot nuclei", Phys. Rev. C, 68: 034327.

[58] Khan, E., Giai, N. V. and Grasso, M., (2004). "Collective motions in hot exotic nuclei: the finite temperature continuum-QRPA", Nuclear Physics A, 731: 311 - 316.

[59] Margueron, J. and Khan, E., (2012). "Suppression, persistence, and reentrance of superfluidity near and beyond the neutron drip", Phys. Rev. C, 86: 065801.

[60] Ramakrishnan E., et. al., (1996). "Giant Dipole Resonance Built on Highly Excited States of ^{120}Sn Nuclei Populated by Inelastic α Scattering", Phys. Rev. Lett., 76: 2025–2028.

[61] Baumann T., et. al., (1998). "Evolution of the giant dipole resonance in excited 120Sn and 208Pb nuclei populated by inelastic alpha scattering", Nuclear Physics A, 635: 428 - 445.

[62] Kelly, M., Snover, K., Schagen, vanJ., Kicinska-Habior, M. and Trznadel, Z., (1999). "The GDRwidth in hot Sn nuclei", Nuclear Physics A, 649: 123 - 129.

[63] Kelly, M. P., Snover, K. A., Van Schagen, J. P. S., Kicinska-Habior, M. and Trznadel, Z., (1999). "Giant Dipole Resonance in Highly Excited Nuclei: Does the Width Saturate?", Phys. Rev. Lett., 82: 3404–3407.

[64] Heckman P., et. al., (2003). "Low-temperature measurement of the giant dipole resonance width", Physics Letters B, 555: 43 - 48.

[65] Lacroix, D., Chomaz, P. and Ayik, S., (1998). “Finite temperature nuclear response in the extended random phase approximation”, Phys. Rev. C, 58: 2154–2160.

[66] Lacroix, D., Chomaz, P. and Ayik, S., (2000). “Collisional effects in the finite temperature dipole response of 120Sn and 208Pb”, Physics Letters B, 489: 137 - 142.

[67] Dang, N. D. and Arima, A., (2003). “Pairing effect on the giant dipole resonance width at low temperature”, Phys. Rev. C, 68: 044303.

[68] Storozhenko, A. N., Vdovin, A. I., Ventura, A. and Blokhin, A. I., (2004). “Temperature dependence of spreading width of giant dipole resonance”, Phys. Rev. C, 69: 064320.

[69] Sagawa, H. and Bertsch, G., (1984). “Self-consistent calculations of finite temperature nuclear response function”, Physics Letters B, 146: 138 - 142.

[70] Sommermann, H., (1983). “Microscopic description of giant resonances in highly excited nuclei”, Annals of Physics, 151: 163 - 203.

[71] Khan, E., Giai, N. V. and Grasso, M., (2004). “Collective motions in hot exotic nuclei: the finite temperature continuum-QRPA”, Nuclear Physics A, 731: 311 - 316.

[72] Niu, Y., Paar, N., Vretenar, D. and Meng, J., (2009). “Low-energy monopole and dipole response in nuclei at finite temperature”, Physics Letters B, 681: 315 - 319.

[73] Harakeh, M. and Van Der Woude, A., (2001). Giant Resonances: Fundamental High-Frequency Modes of Nuclear Excitation, OUP Oxford.

[74] Bothe, W. and Gentner, W., (1937). “Giant Dipole Resonance”, Z. Phys., 71: 236.

[75] Baldwin, G. C. and Klaiber, G. S., (1947). “Photo-Fission in Heavy Elements”, Phys. Rev., 71: 3–10.

[76] Lui, Y.-W., Youngblood, D. H., Tokimoto, Y., Clark, H. L. and John, B., (2004). “Giant resonances in ^{112}Sn and ^{124}Sn: Isotopic dependence of monopole resonance energies”, Phys. Rev. C, 70: 014307.

[77] Youngblood, D. H., Lui, Y.-W., Clark, H. L., John, B., Tokimoto, Y. and Chen, X., (2004). “Isoscalar $E0$-$E3$ strength in ^{116}Sn, ^{144}Sm, ^{154}Sm, and ^{208}Pb”, Phys. Rev. C, 69: 034315.

[78] Li T., et. al., (2010). “Isoscalar giant resonances in the Sn nuclei and implications for the asymmetry term in the nuclear-matter incompressibility”, Phys. Rev. C, 81: 034309.

[79] Pitthan, R. and Walcher, T., (1971). “Inelastic electron scattering in the giant resonance region of La, Ce and Pr”, Physics Letters B, 36: 563 - 564.

[80] Fukuda, S. and Torizuka, Y., (1972). “Giant Multipole Resonances in ^{90}Zr Observed by Inelastic Electron Scattering”, Phys. Rev. Lett., 29: 1109–1111.

[81] Fukunishi, N., Otsuka, T. and Tanihata, I., (1993). “Neutron-skin and proton-skin formations in exotic nuclei far from stability”, Phys. Rev. C, 48: 1648–1655.

[82] Hamamoto, I. and Zhang, X. Z., (1995). “Neutron skin of nuclei near the neutron drip line”, Phys. Rev. C, 52: R2326–R2329.

[83] Aumann, T., (2005). “Reactions with fast radioactive beams of neutron-rich nuclei”, Eur. Phys. J. A, 26: 441-478.

[84] Leistenschneider A., et. al., (2001). “Photoneutron Cross Sections for Unstable Neutron-Rich Oxygen Isotopes”, Phys. Rev. Lett., 86: 5442–5445.

[85] Aumann, T., (2008). “Giant Resonances in Exotic Nuclei Experimental Status and Perspectives”, Nuclear Physics A, 805: 198c - 209c.

[86] Wieland O., et. al., (2009). “Search for the Pygmy Dipole Resonance in ^{68}Ni at 600 MeV/nucleon”, Phys. Rev. Lett., 102: 092502.

[87] Govaert K., et.al., (1998). “Dipole excitations to bound states in ^{116}Sn and ^{124}Sn”, Phys. Rev. C, 57: 2229–2249.

[88] Hartmann, T., Enders, J., Mohr, P., Vogt, K., Volz, S. and Zilges, A., (2002). “Dipole and electric quadrupole excitations in ^{40,48}Ca”, Phys. Rev. C, 65: 034301.

[89] Paar, N., Niu, Y. F., Vretenar, D. and Meng, J., (2009). “Isoscalar and Isovector Splitting of Pygmy Dipole Structures”, Phys. Rev. Lett., 103: 032502.

[90] Endres J., et. al., (2009). “Splitting of the pygmy dipole resonance in ^{138}Ba and ^{140}Ce observed in the $(\alpha,\alpha'\gamma)$ reaction”, Phys. Rev. C, 80: 034302.

[91] Endres J., et. al., (2010). “Isospin Character of the Pygmy Dipole Resonance in ^{124}Sn”, Phys. Rev. Lett., 105: 212503.

[92] Slater, J. C., (1951). “A Simplification of the Hartree-Fock Method”, Phys. Rev., 81: 385–390.

[93] Gaudefroy L., et. al., (2006). “Reduction of the Spin-Orbit Splittings at the $N=28$ Shell Closure”, Phys. Rev. Lett., 97: 092501.

[94] Bastin B., et. al., (2007). “Collapse of the $N=28$ Shell Closure in ^{42}Si”, Phys. Rev. Lett., 99: 022503.

[95] Schiffer J. P., et. al., (2004). “Is the Nuclear Spin-Orbit Interaction Changing with Neutron Excess?”, Phys. Rev. Lett., 92: 162501.

[96] Lesinski, T., Bender, M., Bennaceur, K., Duguet, T. and Meyer, J., (2007). “Tensor part of the Skyrme energy density functional: Spherical nuclei”, Phys. Rev. C, 76: 014312.

[97] Otsuka, T., Suzuki, T., Fujimoto, R., Grawe, H. and Akaishi, Y., (2005). "Evolution of Nuclear Shells due to the Tensor Force", Phys. Rev. Lett., 95: 232502.

[98] Otsuka, T., Matsuo, T. and Abe, D., (2006). "Mean Field with Tensor Force and Shell Structure of Exotic Nuclei", Phys. Rev. Lett., 97: 162501.

[99] Otsuka, T., Suzuki, T., Honma, M., Utsuno, Y., Tsunoda, N., Tsukiyama, K. and Hjorth-Jensen, M., (2010). "Novel Features of Nuclear Forces and Shell Evolution in Exotic Nuclei", Phys. Rev. Lett., 104: 012501.

[100] Otsuka, T. and Abe, D., (2007). "Mean field properties of exotic nuclei and the tensor force", Progress in Particle and Nuclear Physics, 59: 425 - 431.

[101] Bertsch, G. and Esbensen, H., (1991). "Pair correlations near the neutron drip line", Annals of Physics, 209: 327 - 363.

[102] Bohm, D. and Pines, D., (1953). "A Collective Description of Electron Interactions: III. Coulomb Interactions in a Degenerate Electron Gas", Phys. Rev., 92: 609–625.

[103] Giai, N. V. and Sagawa, H., (1981). "Monopole and dipole compression modes in nuclei", Nuclear Physics A, 371: 1 - 18.

[104] Yüksel, E., Khan, E. and Bozkurt, K., (2012). "Analysis of the neutron and proton contributions to the pygmy dipole mode in doubly magic nuclei", Nuclear Physics A, 877: 35-50.

[105] Khan, E., Sandulescu, N., Grasso, M. and Van Giai, N., (2002). "Continuum quasiparticle random phase approximation and the time-dependent Hartree-Fock-Bogoliubov approach", Phys. Rev. C, 66: 024309.

[106] Gambacurta, D., Grasso, M. and Catara, F., (2011). "Low-lying dipole response in the stable ^{40,48}Ca nuclei with the second random-phase approximation", Phys. Rev. C, 84: 034301.

[107] Daoutidis, I. and Ring, P., (2011). "Relativistic continuum quasiparticle random-phase approximation in spherical nuclei", Phys. Rev. C, 83: 044303.

[108] Chabanat, E., Bonche, P., Haensel, P., Meyer, J. and Schaeffer, R., (1998). "A Skyrme parametrization from subnuclear to neutron star densities Part II. Nuclei far from stabilities", Nuclear Physics A, 635: 231 - 256.

[109] Fuller, E., (1985). "Photonuclear reaction cross sections for 12C, 14N and 16O", Physics Reports, 127: 185 - 231.

[110] Sagawa, H. and Suzuki, T., (1999). "Pigmy and giant dipole states in oxygen isotopes", Phys. Rev. C, 59: 3116–3119.

[111] Woodworth, J. G., McNeill, K. G., Jury, J. W., Alvarez, R. A., Berman, B. L., Faul, D. D. and Meyer, P., (1979). "Photonuclear cross sections for ^{18}O", Phys. Rev. C, 19: 1667–1683.

[112] Hartmann, T., Enders, J., Mohr, P., Vogt, K., Volz, S. and Zilges, A., (2000). “Measurement of the Dipole and Electric Quadrupole Strength Distributions up to 10 MeV in the Doubly Magic Nuclei ^{40}Ca and ^{48}Ca”, Phys. Rev. Lett., 85: 274–277.

[113] Co’, G., Donno, V. D., Maieron, C., Anguiano, M. and Lallena, A. M., (2009). “Evolution of the pygmy dipole resonance in nuclei with neutron excess”, Phys. Rev. C, 80: 014308.

[114] Carbone, A., Colò, G., Bracco, A., Cao, L.-G., Bortignon, P. F., Camera, F. and Wieland, O., (2010). “Constraints on the symmetry energy and neutron skins from pygmy resonances in ^{68}Ni and ^{132}Sn”, Phys. Rev. C, 81: 041301.

[115] Litvinova, E., Ring, P., Tselyaev, V. and Langanke, K., (2009). “Relativistic quasiparticle time blocking approximation. II. Pygmy dipole resonance in neutron-rich nuclei”, Phys. Rev. C, 79: 054312.

[116] Terasaki, J. and Engel, J., (2006). “Self-consistent description of multipole strength: Systematic calculations”, Phys. Rev. C, 74: 044301.

[117] Pèru, S., Berger, J. and Bortignon, P., (2005). “Giant resonances in exotic spherical nuclei within the RPA approach with the Gogny force”, The European Physical Journal A - Hadrons and Nuclei, 26: 25-32.

[118] Vitturi, A., Lanza, E. G., Andrés, M. V., Catara, F. and Gambacurta, D., (2011). “Giant and Pygmy Dipole Resonances in neutron-rich nuclei: their excitation via Coulomb and nuclear fields”, Journal of Physics: Conference Series, 267: 012006.

[119] Arteaga, D. P., Khan, E. and Ring, P., (2009). “Isovector dipole strength in nuclei with extreme neutron excess”, Phys. Rev. C, 79: 034311.

[120] Tsoneva, N. and Lenske, H., (2008). “Pygmy dipole resonances in the tin region”, Phys. Rev. C, 77: 024321.

[121] Ritman J., et. al., (1993). “First observation of the Coulomb-excited double giant dipole resonance in ^{208}Pb via double-γ decay”, Phys. Rev. Lett., 70: 533–536.

[122] Ryezayeva N., et. al., (2002). “Nature of Low-Energy Dipole Strength in Nuclei: The Case of a Resonance at Particle Threshold in ^{208}Pb”, Phys. Rev. Lett., 89: 272502.

[123] Yüksel, E., Khan, E. and Bozkurt, K., (2013). “The soft Giant Monopole Resonance as a probe of the spin-orbit splitting”, The European Physical Journal A, 49: 124.

[124] Dickey, S., Kraushaar, J., Ristinen, R. and Rumore, M., (1982). “The 120Sn(p, d)119Sn reaction at 26.3 MeV”, Nuclear Physics A, 377: 137 - 147.

[125] Oros, A.-M., (1996). Study of the coupling between single-particle and collective degrees of freedom in medium-mass spherical nuclei, PhD Thesis, University of Köln, .

[126] Negele, J. and Vautherin, D., (1973). “Neutron star matter at sub-nuclear densities”, Nuclear Physics A, 207: 298 - 320.

[127] Chamel, N., Naimi, S., Khan, E. and Margueron, J., (2007). “Validity of the Wigner-Seitz approximation in neutron star crust”, Phys. Rev. C, 75: 055806.

[128] N. Schwierz, A. V., “Parameterization of the Woods-Saxon Potential for Shell-Model Calculations”, arXiv:0709.3525, .

[129] Mahaux C., et. al., (1985). “Dynamics of the shell model”, Physics Reports, 120: 1 - 274.

[130] Kamerdzhiev, S., Speth, J. and Tertychny, G., (2004). “Extended theory of finite Fermi systems: collective vibrations in closed shell nuclei”, Physics Reports, 393: 1 - 86.

[131] Agrawal, B. K. and Shlomo, S., (2004). “Consequences of self-consistency violations in Hartree-Fock random-phase approximation calculations of the nuclear breathing mode energy”, Phys. Rev. C, 70: 014308.

[132] Monrozeau C., et. al., (2008). “First Measurement of the Giant Monopole and Quadrupole Resonances in a Short-Lived Nucleus: ^{56}Ni”, Phys. Rev. Lett., 100: 042501.

[133] Avdeenkov, A., Goriely, S., Kamerdzhiev, S. and Krewald, S., (2011). “Self-consistent calculations of the strength function and radiative neutron capture cross section for stable and unstable tin isotopes”, Phys. Rev. C, 83: 064316.

[134] Haxel, O., Jensen, J. H. D. and Suess, H. E., (1949). “On the "Magic Numbers" in Nuclear Structure”, Phys. Rev., 75: 1766–1766.

[135] Hagen, G., Hjorth-Jensen, M., Jansen, G. R., Machleidt, R. and Papenbrock, T., (2012). “Evolution of Shell Structure in Neutron-Rich Calcium Isotopes”, Phys. Rev. Lett., 109: 032502.

[136] Rejmund M., et. al., (2007). “Shell evolution and the $N = 34$ “magic number””, Phys. Rev. C, 76: 021304.

[137] Coraggio, L., Covello, A., Gargano, A. and Itaco, N., (2009). “Spectroscopic study of neutron-rich calcium isotopes with a realistic shell-model interaction”, Phys. Rev. C, 80: 044311.

[138] Holt, J. D., Menèndez, J. and Schwenk, A., (2013). “The role of three-nucleon forces and many-body processes in nuclear pairing”, Journal of Physics G: Nuclear and Particle Physics, 40: 075105.

[139] Holt, J. D., Otsuka, T., Schwenk, A. and Suzuki, T., (2012). “Three-body forces and shell structure in calcium isotopes”, Journal of Physics G: Nuclear and Particle Physics, 39: 085111.

[140] Grasso, M., (2014). “Magicity of the ^{52}Ca and ^{54}Ca isotopes and tensor contribution within a mean-field approach”, Phys. Rev. C, 89: 034316.

[141] Yüksel, E., Van Giai, N., Khan, E. and Bozkurt, K., (2014). “Effects of the tensor force on the ground state and first 2^+ states of the magic ^{54}Ca nucleus”, Phys. Rev. C, 89: 064322.

[142] Audi, G., Wapstra, A. and Thibault, C., (2003). “The Ame2003 atomic mass evaluation: (II). Tables, graphs and references”, Nuclear Physics A, 729: 337 - 676.

[143] Bennaceur, K. and Dobaczewski, J., (2005). “Coordinate-space solution of the Skyrme Hartree Fock Bogolyubov equations within spherical symmetry. The program HFBRAD (v1.00)”, Computer Physics Communications, 168: 96 - 122.

[144] Cao, L.-G., Colò, G., Sagawa, H., Bortignon, P. F. and Sciacchitano, L., (2009). “Effects of the tensor force on the multipole response in finite nuclei”, Phys. Rev. C, 80: 064304.

[145] Cao, L.-G., Sagawa, H. and Colò, G., (2011). “Effects of tensor correlations on low-lying collective states in finite nuclei”, Phys. Rev. C, 83: 034324.

[146] Raman, S., Nestor, J. R. C. and Tikkanen, P., (2001). “Transition Probability from the ground to the first-excited 2+ state of even-even nuclides”, Atomic Data and Nuclear Data Tables, 78: 1 - 128.

[147] Sagawa, H. and Giai, N. V., (1983). “Transition charge and current densities of collective isoscalar quadrupole states in 208Pb”, Physics Letters B, 127: 393 - 398.

[148] Khan, E., Giai, N. V. and Sandulescu, M., (2007). “Pairing interactions and vanishing pairing correlations in hot nuclei”, Nuclear Physics A, 789: 94-102.

[149] Niu, Y. F., Niu, Z. M., Paar, N., Vretenar, D., Wang, G. H., Bai, J. S. and Meng, J., (2013). “Pairing transitions in finite-temperature relativistic Hartree-Bogoliubov theory”, Phys. Rev. C, 88: 034308.

[150] Schiller A., et. al., (2001). “Critical temperature for quenching of pair correlations”, Phys. Rev. C, 63: 021306.

[151] Melby, E., Guttormsen, M., Rekstad, J., Schiller, A., Siem, S. and Voinov, A., (2001). “Thermal and electromagnetic properties of ^{166}Er and ^{167}Er”, Phys. Rev. C, 63: 044309.

[152] Sandulescu, N., (2004). “Nuclear superfluidity and specific heat in the inner crust of neutron stars”, Phys. Rev. C, 70: 025801.

[153] Monrozeau, C., Margueron, J. and Sandulescu, N., (2007). “Nuclear superfluidity and cooling time of neutron star crusts”, Phys. Rev. C, 75: 065807.

[154] Donati, P., Pizzochero, P. M., Bortignon, P. F. and Broglia, R. A., (1994). “Temperature dependence of the nucleon effective mass and the physics of stellar collapse”, Phys. Rev. Lett., 72: 2835–2838.

[155] Fantina, A. F., (2010). Supernovae Theory: Study of Electro-weak processes during gravitational collapse of massive stars, PhD Thesis, Universitè Paris Sud XI and Universitè degli Studi di Milano, Paris.

[156] Fantina, A., Donati, P. and Pizzochero, P., (2009). "Systematic thermal reduction of neutronization in core-collapse supernovae", Physics Letters B, 676: 140 - 145.

[157] Dean, D. J., Langanke, K. and Sampaio, J. M., (2002). "Temperature dependence of the symmetry energy", Phys. Rev. C, 66: 045802.

[158] Yüksel, E., Khan, E., Bozkurt, K. and Colò, G., (2014). "Effect of temperature on the effective mass and the neutron skin of nuclei", The European Physical Journal A, 50: 160.

[159] Matsuo, M., (2001). "Continuum linear response in coordinate space Hartree Fock Bogoliubov formalism for collective excitations in drip line nuclei", Nuclear Physics A, 696: 371 - 395.

[160] Paul Bonche, S. L. and Vautherin, D., (1984). "Mean-field description of nuclei at high temperature", Nuclear Physics A, 428: 95 - 99.

[161] Egido, J. L., Robledo, L. M. and Martin, V., (2000). "Behavior of Shell Effects with the Excitation Energy in Atomic Nuclei", Phys. Rev. Lett., 85: 26–29.

[162] Giai, N. V. and Sagawa, H., (1981). "Spin-isospin and pairing properties of modified Skyrme interactions", Physics Letters B, 106: 379 - 382.

[163] Beiner M., G. N. and Quentin, P., (1975). "Nuclear ground-state properties and self-consistent calculations with the skyrme interaction: (I). Spherical description", Nuclear Physics A, 238: 29 - 69.

[164] Bartel, J., Quentin, P., Brack, M., Guet, C. and Håkansson, H. B., (1982). "Towards a better parametrisation of Skyrme-like effective forces: A critical study of the SkM force", Nuclear Physics A, 386: 79 - 100.

[165] Dobaczewski, J., Nazarewicz, W., Werner, T. R., Berger, J. F., Chinn, C. R. and Dechargé, J., (1996). "Mean-field description of ground-state properties of drip-line nuclei: Pairing and continuum effects", Phys. Rev. C, 53: 2809–2840.

[166] Hasse, R. W. and Schuck, P., (1986). "Correlation effects on the level density of a hot nucleus", Physics Letters B, 179: 313 - 316.

[167] Bortignon, P. and Dasso, C., (1987). "Effective mass and level-density parameter in nuclei at finite temperature", Physics Letters B, 189: 381 - 383.

[168] Heckman, P., Back, B., Baumann, T., Carpenter, M., Diószegi, I., Hofman, D., Khoo, T., Mitsuoka, S., Nanal, V., Pennington, T., Seitz, J., Thoennessen, M., Tryggestad, E. and Varner, R., (2005). "Temperature and spin dependence of the giant dipole resonance width", Nuclear Physics A, 750: 175 - 184.

[169] Santonocito, D., and Blumenfeld, Y., , (2006). "Evolution of the giant dipole resonance properties with excitation energy", Eur. Phys. J. A, 30: 183-202.

[170] Krumbholz A.M., et. al., (2015). "Low-energy electric dipole response in 120Sn", Physics Letters B, 744: 7 - 12.

CURRICULUM VITAE

PERSONAL INFORMATION

Name Surname : Esra Yüksel

Date of birth and place : August 09, 1987 – İstanbul

Foreign Languages : English

E-mail : eyuksel@yildiz.edu.tr

EDUCATION

Degree	Department	University	Date of Graduation
Masters	Physics	Yıldız Technical University	2011
Undergraduate	Physics	Abant İzzet Baysal University	2009
High School	Science–Mathematics	Süleyman Nazif High School	2004

WORK EXPERIENCE

Year	Corporation/Institution	Job Description
2010–20..	Yıldız Technical University	Research and Teaching Assistant

PUBLICATIONS

1. Yüksel. E., Khan. E. Bozkurt. K., (2012). “Analysis of the neutron and proton contributions to the pygmy dipole mode in doubly magic nuclei”, Nuclear Physics A (NPA) 877, 35–50 (2012).

2. Yüksel. E., Khan. E. Bozkurt. K., (2013). “The soft Giant Monopole Resonance as a probe of the spin-orbit splitting”, The European Physical Journal A (EPJA), 49(10).

3. Yüksel. E., Khan. E. Bozkurt. K., Colò G., (2014).“ Effect of temperature on the effective mass and the neutron skin of nuclei”, The European Physical Journal A (EPJA), 50(10), 160.

4. Yüksel. E., Giai N. V., Khan. E. Bozkurt. K., (2014). " Effects of the tensor force on the ground state and first 2^{+} states of the magic ^{54}Ca nucleus", Physical Review C (PRC), 89(6).

5. Yüksel. E., Khan. E. Bozkurt. K., (2014). " Pairing properties of hot nuclei within the finite temperature Hartree Fock+BCS approximation", Journal of Physics: Conference Series, 533(012019).

6. Yüksel. E., Bozkurt. K., (2011)." Tensor Effects in Pygmy Dipole Excitation", International Journal of Modern Physics E (IJMPE), 20(10), 2143-2151.

7. Yüksel. E., Bozkurt. K., (2013). " Tensor Effects in Dipole Excitations at Finite Temperature", Acta Physica Polonica A, 123(2), 320-322.

8. Yüksel. E., Gök. Ç. Bozkurt. K., (2013)." Detailed investigation of the tensor force on the evaluation of the single particle levels of Z=28 and Z=82 nuclei", Modern Physics Letters A (MPLA), 28(38).

Posters and Presentations in Conferences

1. Yüksel. E., Khan. E., Colò G., Bozkurt. K.,(2015, September). Evolution of multipole response in nuclei at finite temperature. Collective Motion in Nuclei under Extreme Conditions. Collective Motion in Nuclei under Extreme Conditions (COMEX5). Krakow, Poland.

2. Bozkurt. K., Yüksel. E., (2014, April). Investigation of the neutron skin thickness via low-energy modes of nuclei. APMAS-Antalya. International Advances in Applied Physics and Materials Science Congress.

3. Yüksel. E., Khan. E. Bozkurt. K., (2014, October). Low energy modes in Atomic nuclei. VII. International Workshop on Nuclear Structure Properties. Sinop-Turkey.

4. Yüksel. E., Khan. E. Bozkurt. K., Giai N. V., Colò G.,(2014, September). Tensor and Temperature effects on the nuclear properties. NUBA Conference Series-1 Nuclear Physics and Astrophysics. Antalya/Turkey.

5. Yüksel. E., Khan. E. Bozkurt. K., (2013, September). Pairing properties of hot nuclei within the finite temperature Hartree Fock+BCS approximation. XX International School on Nuclear Physics, Neutron Physics and Applications. Varna-Bulgaristan.

6. Yüksel. E., Bozkurt. K., (2013, April). Investigation of tensor correlations on the single particle properties of heavy nuclei. APMAS (International Advances in Applied Physics and Materials Science Congress). Antalya.

7. Yüksel. E., Bozkurt. K., (2013, April). Investigation of Bubble nuclei. APMAS (International Advances in Applied Physics and Materials Science Congress). Antalya.

8. Gök. Ç., Yüksel. E., Bozkurt. K., (2013, September). Effect of tensor interaction on the ground state properties of light, medium and heavy nuclei. XX International School on Nuclear Physics, Neutron Physics and Applications. Varna-Bulgaristan.

9. Bozkurt. K., Yüksel. E., Khan. E. (2012, October). Low-energy strength in Calcium isotopes. Collective Motion in Nuclei under Extreme Conditions (COMEX4), Kanagawa, JAPONYA.

10. Yüksel. E., Bozkurt. K., (2011, September). Investigation of tensor effects on the pygmy dipole resonance of neutron-rich nuclei. Turkish Physical Society 28^{th} International Physics Congress.

11. Bozkurt. K., Yüksel. E., (2011, September). Isovector Pygmy dipole strength in ^{68}Ni. Turkish Physical Society 28^{th} International Physics Congress.

12. Yüksel. E., Bozkurt. K.,(2010, September). Pygmy Dipole Resonance in neutron rich nuclei with Skyrme and Gogny interactions. Turkish Physical Society 27^{th} International Physics Congress-İstanbul.